The Dissertation Committee for Kenneth Mark Pesyna, Jr.
certifies that this is the approved version of the following dissertation:

Advanced Techniques for Centimeter-Accurate GNSS Positioning on Low-Cost Mobile Platforms

Committee:

Todd E. Humphreys, Supervisor

Robert W. Heath, Jr., Co-Supervisor

Sujay Sanghavi

Haris Vikalo

Johnathan York

Advanced Techniques for Centimeter-Accurate GNSS Positioning on Low-Cost Mobile Platforms

by

Kenneth Mark Pesyna, Jr., B.S.E.E.; M.S.E.

DISSERTATION

Presented to the Faculty of the Graduate School of

The University of Texas at Austin

in Partial Fulfillment

of the Requirements

for the Degree of

DOCTOR OF PHILOSOPHY

THE UNIVERSITY OF TEXAS AT AUSTIN

December 2015

Dedicated to my beautiful wife, Kathryn.

Acknowledgments

I would like to thank the multitude of people who helped me both directly and behind the scenes to support me and encourage me in completing my Ph.D.

I thank Dr. Todd Humphreys for his inspiring ideas and passion that made every discussion feel exciting and meaningful. I thank him also for his devotion to first principles and his innate capability to break our ideas down to these first principles on the spot. Our white board discussions and detailed follow-up emails were my best learning moments.

I thank Dr. Robert Heath for his clear and structured writing style which helped me to always remember the confused and busy readers. He taught me to craft my writing to teach with the fewest amount of words. I thank him also for his persistence in always celebrating accomplishments, even the little ones, through emails and group outings.

I thank my committee members, Dr. Sujay Sanghavi, Dr. Haris Vikalo, and Dr. Johnathan York, for reviewing my research and serving on my committee.

I thank the members of the Radionavigation Laboratory, the Wireless Systems Innovation Laboratory, and the Wireless Networking and Communications Group for their inspiration, friendship, and discussions that made each day in the office fun.

I would like to acknowledge the various funding sources that generously supported me throughout my graduate program. These sources include The University of Texas, The United States Department of Transportation, the National Defense

Science and Engineering Graduate Fellowship, the National Science Foundation, and Samsung Research America.

I wish to thank my many friends, who inspired me along the way and with whom I've had many great moments: My Purdue friends for our long webchats and their desire to stay in touch; Andrew for his selfless attitude and clearheaded discussions my final year; Jahshan for talking things out and helping me to get unstuck so many times; Zak for always being upbeat; Daniel for his attention to detail; Marlon for our life discussions and early morning bible studies; Tory for his sacrificial discipleship; John for encouraging me to pursue my faith; and Kyle for inspiring me throughout and showing me how it's done.

I thank my brothers and sisters for their many summer visits and desire to spend time together at every break.

I thank my mother and father for making me who I am today. I will forever be shaped by their unconditional love, teaching, and sacrifice.

Most importantly, I wish to thank my wife, Kathryn. I thank her for her sacrifice to support our family and encourage me while I pursued my degree. She has been, and will always be, my biggest cheerleader.

Advanced Techniques for Centimeter-Accurate GNSS Positioning on Low-Cost Mobile Platforms

Publication No. ______________

Kenneth Mark Pesyna, Jr., Ph.D.
The University of Texas at Austin, 2015

Supervisor: Todd E. Humphreys

Co-Supervisor: Robert W. Heath, Jr.

Over the past decade, GPS and other Global Navigation Satellite System (GNSS) chipsets have become smaller, cheaper, and more energy efficient, so much so that they now come standard in most smartphones and tablets. Under good multipath conditions, one can expect 2-to-3-meter-accurate positioning with these chipsets, under adverse multipath, accuracy degrades to 10 meters or worse. Outside the mainstream of consumer GNSS receivers, however, centimeter—even millimeter—accurate GNSS receivers are used routinely in geodesy, agriculture, and surveying. The key to their accuracy is a radically different approach to positioning in which the standard code-phase (or pseudorange) positioning technique is replaced by differential carrier-phase positioning. Adopting this high-precision carrier-phase-based technique for consumer-grade mobile devices is possible, but comes with significant challenges.

This dissertation identifies and addresses the challenges to performing centimeter accurate carrier-phase differential GNSS (CDGNSS) positioning on low-cost mobile devices. To this end, this dissertation makes three primary contributions.

First, this dissertation develops a carrier phase reconstruction technique to address the high power consumption of current CDGNSS algorithms. The reconstruction technique enables a continuous and unambiguous phase time history to be reconstructed from intermittent phase measurements, permitting aggressive duty cycling of the mobile device's internal GNSS chip, decreasing energy consumption.

Second, this dissertation demonstrates that a centimeter-accurate positioning solution is possible based on GNSS data collected using a smartphone, a first in the open literature. It is identified that the primary impediment to performing CDGNSS on smartphones lies not in the commodity GNSS chipset within the phone, but instead in the antenna, whose chief failing is its poor multipath suppression, resulting in long initialization times. It is demonstrated that wavelength-scale random antenna motion can be used to decorrelate multipath errors and reduce the initialization period—the so-called time-to-ambiguity-resolution (TAR)—of smartphones employing CDGNSS to obtain centimeter-level positioning fix.

Finally, this dissertation develops a framework that tightly fuses smartphone camera image measurements with GNSS carrier phase measurements to reduce CDGNSS initialization times beyond what is achievable using antenna motion alone. The framework augments the traditional bundle-adjustment- (BA-)-based structure from motion (SFM) algorithm with the carrier phase differential GNSS (CDGNSS) algorithm in a way that preserves the key features of both algorithms, namely the sparseness of the matrices in BA and the integer structure of the ambiguities in CDGNSS. The framework is shown to produce a faster, more robust, and more accurate positioning solution than achievable with existing techniques.

Table of Contents

List of Figures

Chapter 1

Introduction

On May 2, 2000, the intentional degradation of the Global Positioning System (GPS) signals known as selective availability was turned off and the position accuracy obtainable by civilian GPS receivers went from errors of 50 meters or more to errors on the order of a few meters. Such a large and sudden increase in accuracy opened up the floodgates for the consumer use of GPS. Since the turn of the century, the use of GNSS by the civilian sector has risen at an exponential rate [5], leading to an infiltration of GNSS receivers into the industrial and consumer markets. Recently, GNSS receivers have made their way into smartphones and tablets and now come standard in these devices [6, 7]. These embedded GNSS chipset receivers have been used to provide mobile devices with on-demand position information, enabling a host of applications such as turn-by-turn directions, location-focused web searches, fitness tracking, and more.

Despite significant improvements to consumer-grade GNSS receivers, enabling them to meet size, energy, and cost constraints of the mobile devices into which they have been embedded [8], their underlying position accuracy has stagnated at about 2-3 meters. Figure 1.1 shows the GPS user range error (URE) over a 12 year time span [9]. The URE represents the errors in a receiver's code-phase-based range calculation due to imperfect satellite clock and orbit models broadcast to receivers in the GPS navigation message stream [10]. Despite a trend of improvements

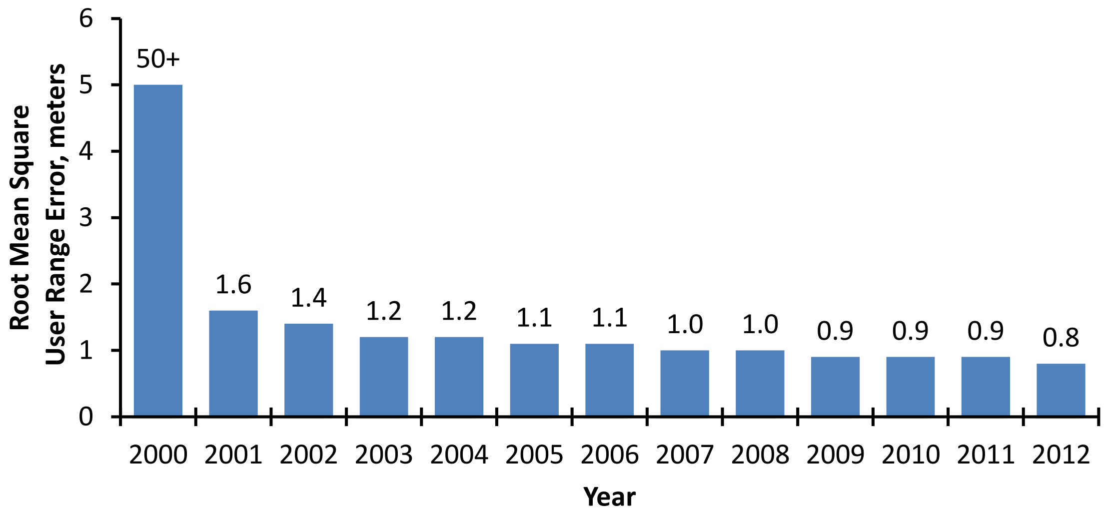

Figure 1.1: Trends indicate that user range error has been declining, but at a slowing rate, over the last 12 years. [1]

by the GPS space-segment [1], URE seems to have stagnated at around 0.8 meters. Furthermore, URE is not the only source of positioning error in consumer-grade GNSS receivers. Receiver-side errors, e.g. errors due to receiver clock-variations, front-end noise, and multipath also contribute to the ultimate positioning precision and are on the same order of magnitude as URE. Table 1.1 lists common receiver-dependent error sources and their typical values for a typical consumer-grade receiver. These receiver-side errors lead to a total positioning error about 2 meters. While such accuracy is impressive as compared to just 10 years ago, receiver accuracy using so-called "code-phase" positioning are reaching fundamental limitations. Improvements beyond meter-level accuracy is difficult to achieve, except under ideal circumstances.

Table 1.1: Receiver-Side Range Errors

Error Source	Standard Deviation (meters)
Ionospheric Modeling Errors [11]	0.5
Multipath Errors [12]	1
Front-end Noise (50 dB-Hz signal) [13]	0.5
Cumulative	$(0.5^2 + 1^2 + 0.5^2)^{\frac{1}{2}} = 1.2$

1.1 Carrier-Phase-Based Positioning

Fortunately, there exist advanced positioning techniques, which promise accuracy better than the meter-level of standard code-phase techniques. Such techniques take advantage of the GNSS signal's underlying carrier-phase to provide GNSS receivers with centimeter-level, and, in some cases, millimeter-level accuracy. These techniques, while virtually absent in consumer devices, have for the past decade been implemented in non-consumer industrial-grade receivers and used extensively in the fields of surveying and farming [14, 15]. A natural question is, "So why not adopt these high-precision carrier-phase-based techniques for consumer-grade mobile devices?". This dissertation identifies the primary challenges currently preventing such adoption and presents solutions to address these challenges.

1.1.1 Comparison to Traditional Code-Phase Positioning

GNSS signals consist of a carrier wave modulated by a pseudorandom code sequence. As illustrated in Fig. 1.2, traditional positioning techniques work by tracking each satellite signal's code sequence and use it to estimate a range to each satellite. These ranges are commonly called "pseudoranges" because they have

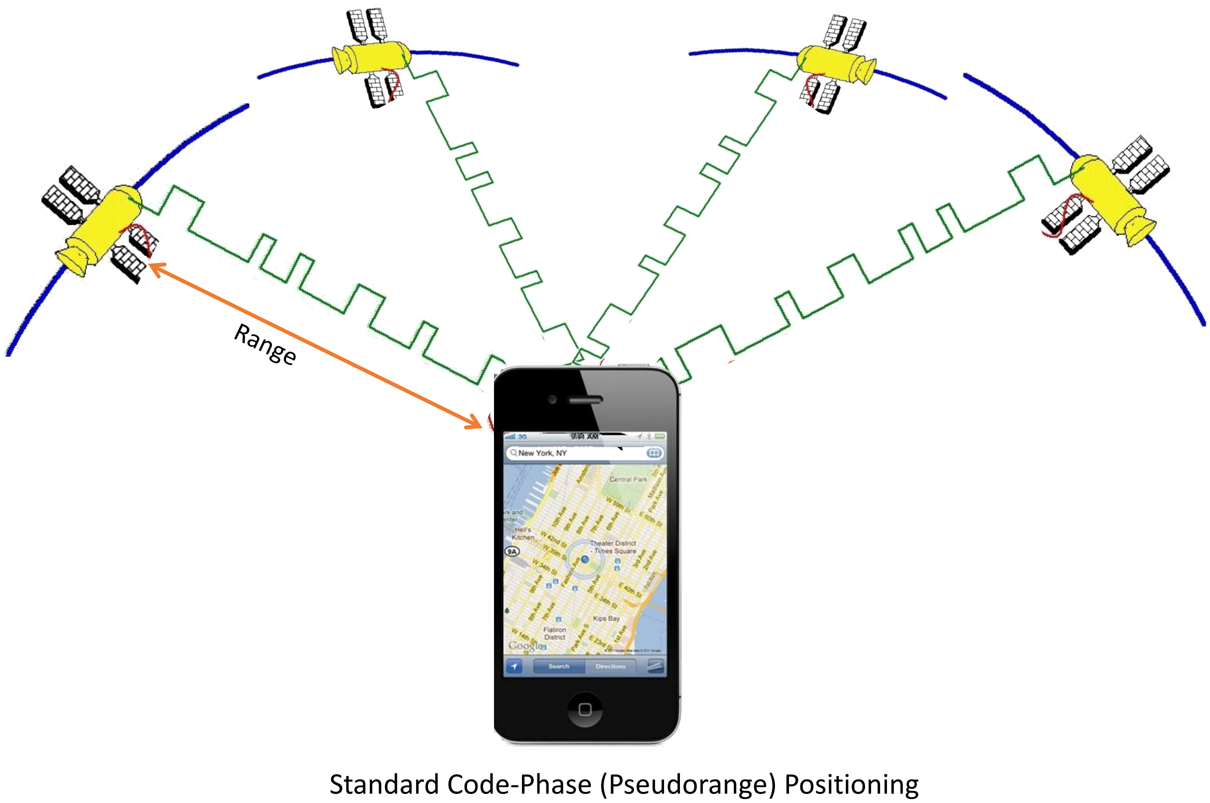

Figure 1.2: Code-phase-based positioning relies on a receiver tracking the code sequence (square-wave) of each GNSS satellite's transmitted signal and uses corresponding code-phase measurements to compute a meter-level-accurate range to each satellite.

errors, e.g., clock-, atmosphere-, and multipath-induced errors, and are thus not error-free "true" ranges. Pseudoranges computed to four or more satellites are subsequently combined into a least-squares cost function, the minimum of which determines the three dimensional receiver position and clock offset of the receiver. This pseudorange-based technique—because it uses a signal's code sequence to compute a position—is known as "code-phase"-based positioning.

In contrast to code-phase positioning, carrier-phase positioning, as illustrated in Fig. 1.3, computes much more precise satellite-receiver ranges by tracking a signal's underlying carrier phase [16, 17]. Because carrier wavelengths are much smaller than the length of each chip in the code sequence (19 centimeters vs 300 meters), or, equivalently because the frequency of the GNSS carrier phase is much higher than the chipping rate of the chipping sequence modulated on top if it, the phase tracking loops that produce carrier-phase measurements can much more easily mitigate the effects receiver noise and multipath. As such, while a GPS code sequence can be tracked with meter-level accuracy (under typical 50 dB-Hz carrier-to-noise ratios), GPS carrier signals can be tracked 100 to 1000 times more accurately, at the centimeter- and millimeter-levels [18].

1.1.2 Challenges

Despite its accuracy advantages, carrier-phase positioning comes with two primary challenges relative to code-phase positioning: initialization time and energy consumption. These challenges are especially apparent on mobile devices, where impatient users and limited battery life strongly influence of this more-accurate positioning technique.

The first challenge, the longer initialization time of carrier phase positioning as compared to code phase positioning, is the result of the need to resolve of so-

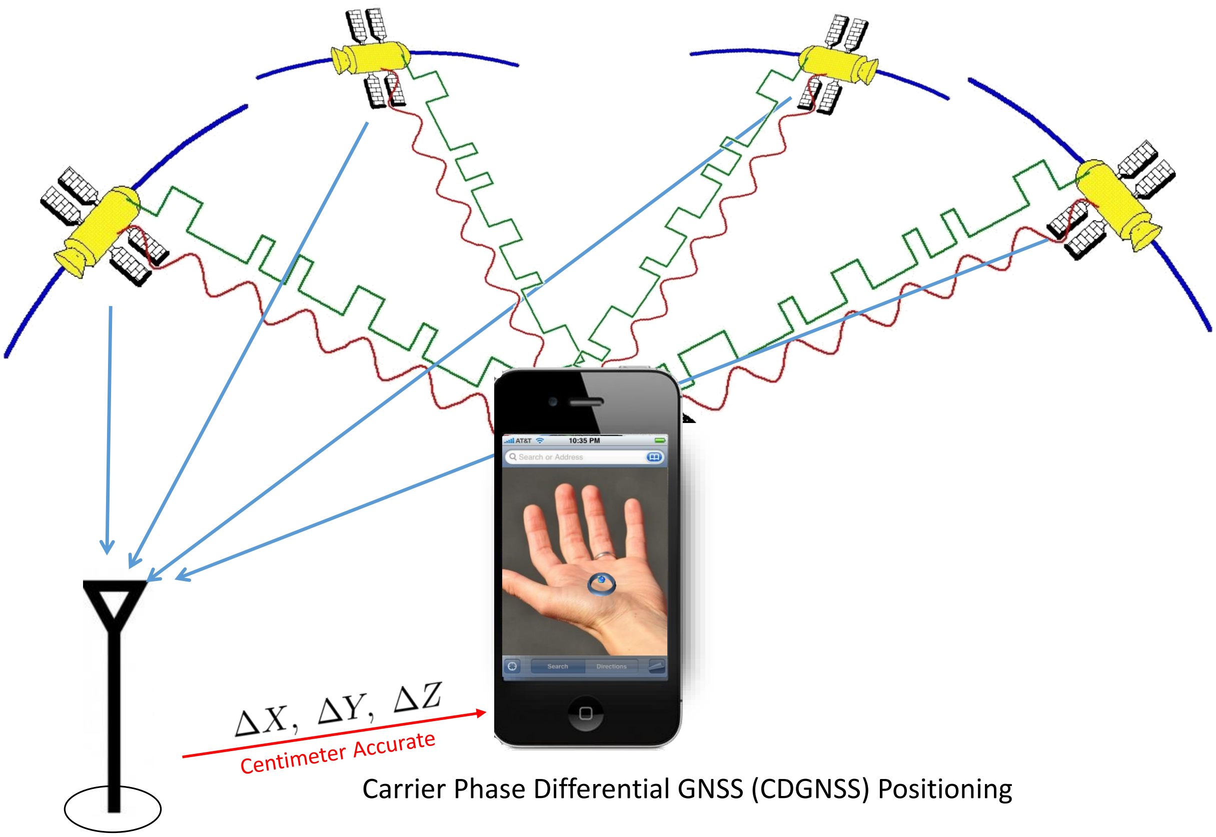

Figure 1.3: Carrier-phase-based positioning relies on a receiver tracking the underlying carrier (sine-wave) of each GNSS satellite's transmitted signal, differencing its carrier phase measurements with those taken from a second receiver tracking the same set of signals, resolving a set of integer ambiguities, and then using these now-unambiguous differenced measurements to compute a centimeter-level-accurate range to each satellite.

called carrier phase ambiguities. Unlike the with measurements of the code-phase of a GNSS signal, measurements of the carrier-phase of a signal cannot be immediately traced back to a known satellite transmission time, thereby preventing an immediate satellite range calculation. The carrier phase ambiguities must first be resolved before a position can be computed. Fortunately, each signal's phase ambiguity can be assumed constant under continuous carrier phase tracking, and even still, can be constrained as integer-valued when measurements are appropriately differenced between two receivers tracking the same set of satellites (see Fig. 1.3). Such differencing is key to a specific carrier-phase positioning technique known as carrier phase differential GNSS (CDGNSS). (See Ch. 3 for further details on CDGNSS). Reliable carrier ambiguity estimation has been the topic of much previous research [16, 19–22]. While good progress has been made in developing optimal techniques to find the true set of integers and also reducing the ambiguity resolution time, the time to ambiguity resolution (TAR) is often dictated by the underlying measurements quality and number of available signals. As such, the need for ambiguity resolution is an added burden of carrier-phase-based positioning as compared to traditional code-phase-based positioning, as it results in a longer time-to-first-fix (TTFF).

A second challenge of carrier-phase-based positioning over code-phase-based positioning is its relatively high power consumption. This stems from its supposed continuous tracking requirement. So long as a receiver is continuously tracking a signal's carrier phase, its carrier phase ambiguity can be assumed constant. The constant nature of ambiguities is important because (1) it becomes easier to estimate them over time as more measurements are captured, and (2) once they are estimated, they can be locked in place and not need be re-estimated. The need for continuous carrier phase tracking, however, prevents measurement duty-cycling, a common energy-saving technique in many code-phase-based GNSS chipsets, especially those embedded in smartphones and tablets. This power-saving duty cycling technique is often aggressive, receivers waking up once a second for only a few milliseconds per second [23, 24]. Such a requirement makes it difficult to maintain lock and the carrier phase of the GNSS signal, preventing CDGNSS.

The ambiguity resolution and energy consumption challenges associated with carrier-phase positioning have so far been a major impediment to the mainstreaming of carrier-phase-based positioning techniques in smartphones and tablets. Nearly all current uses of carrier-phase positioning techniques are by industrial-grade GNSS receivers where these costs are far outweighed by the benefit that their increase in accuracy brings to industrial users. This benefit is further supported by users' willingness to purchase them, despite the high multi-thousand-dollar cost of industrial carrier-phase receivers [25].

1.1.3 Steady Improvements

Fortunately, the challenges to carrier-phase positioning are naturally becoming less severe over time. Every year marks the launch of more GNSS satellites and with these satellites come more signals [5]. As the number of signals in the sky grows, consumer GNSS receivers are quickly augmented to track them. Modern smartphone receivers currently track both American GPS and Russian GLONASS signals [26]. Both carrier-phase- and code-phase-based positioning stand to benefit from such advancements, as more signals create more geometrical constraints and, consequently lead to a more-accurate positioning solution. However, one of the largest benefits of these added signals is unique to carrier-phase positioning. Additional signals significantly improve the probability of successful CDGNSS integer ambiguity resolution, despite there being a larger number of ambiguities to estimate [27]. The improvement comes in the added redundancy brought by extra signals, which significantly reduces the average precision of the pre-fixed float ambiguity estimates [28, 29]. Overall, more signals enable receivers to resolve ambiguities faster in time.

Furthermore, the increasing availability and technological advancement of non-GNSS sensors in smartphones are also soothing the challenges of carrier-phase positioning. The camera and inertial sensors can be used to approximate the smartphone motion profile during ambiguity resolution [30–32], which can be used as a constraint to speed successful ambiguity resolution.

1.1.4 Motivation

The uses of centimeter-accurate positioning in the mass market are becoming increasingly numerous. It is anticipated that a device with low-cost centimeter-accurate positioning and sub-degree accurate orientation capabilities will usher in a host of new and useful applications to the commercial and consumer industries. In the wireless communication industry, the ability to use GNSS measurements to obtain precise antenna position and orientation information could benefit V2V and millimeter wave communication where centimeter-accurate position information can facilitate high gain, narrow beamwidth communication links that require minimal feedback overhead. In another wireless application, two rigidly attached GNSS antennas could be used to provide sub-degree heading determination of cellular basestation antennas to perform precise antenna alignment and maximize coverage efficiency. Furthermore, a mobile device with robust centimeter positioning capability could be used in the entertainment industry for geo-referenced augmented and virtual reality, in the construction industry for low-cost surveying and 3-D map making, and in the automotive industry to provide guidance, navigation, and collision avoidance of autonomous and semi-autonomous vehicles.

1.2 Thesis Statement and Expected Contributions

This dissertation defends the following thesis statement:

Centimeter-accurate GNSS positioning on low-cost mobile platforms is achievable, but hard. These platforms, however, have certain intrinsic features that can be exploited to make the process easier.

The following is a summary of the contributions of this dissertation:

1. **A Carrier Phase Reconstruction Technique:** A carrier phase reconstruction technique to enable low-power centimeter-accurate positioning on mobile devices is developed and analyzed. Carrier-phase positioning solutions currently require continuous, non-duty-cycled signal phase measurements. Accurate carrier phase reconstruction permits the aggressive duty cycling of phase measurements, significantly decreasing the overall energy consumption of existing solutions. This work has been published in [33, 34].

2. **Carrier-Phase Differential GNSS Positioning using Low-Cost Antennas:** It is demonstrated for the first time that a centimeter-accurate positioning solution is possible based on data collected from the internal antenna of a smartphone. It is shown that the primary impediment to performing CDGNSS positioning on low-cost mobile platforms lies not in the commodity GNSS chipset within the phone, but instead in the antenna, whose chief failing is its poor multipath suppression [2]. An empirical analysis of the average gain and carrier phase multipath error susceptibility of smartphone-grade GNSS antennas is offered and it is shown that these properties are significantly worse than what is seen when using even a low-quality external patch antenna.

   It is demonstrated that wavelength-scale random antenna motion can be used to substantially improve the CDGNSS initialization time as compared to keeping the antenna stationary. This work has been published in [2, 35, 36].

3. **A Joint Structure-From-Motion and Carrier Phase Differential GNSS Framework:** A joint Vision and GNSS measurement estimation framework that fuses smartphone camera measurements with differential GNSS carrier phase measurements to reduce CDGNSS initialization times when using low-cost antennas beyond what is achievable using antenna motion alone is developed and analyzed. In addition, it is demonstrated that such fusion facilitates not only centimeter-accurate device position determination—as this is possible on the basis of carrier phase measurements alone—but also sub-degree-accurate device orientation determination and centimeter-accurate, globally-referenced, collaborative, three-dimensional mapping. This work has been published in [31, 37].

1.3 Published Works

The publications to which the author contributed during the course of carrying out the contributions described in this dissertation are as follows.

Journal Publications

1. K. M. Pesyna, Jr., Z. M. Kassas, R. W. Heath, Jr., and T. E. Humphreys, "A phase-reconstruction technique for low-power centimeter-accurate mobile positioning," *IEEE Transactions on Signal Processing*, vol. 62, pp. 2595–2610, May 2014

2. K. M. Pesyna, Jr., T. Novlan, C. Zhang, R. W. Heath, Jr., and T. E. Humphreys, "Exploiting antenna motion for faster initialization of centimeter-accurate

GNSS positioning with low-cost antennas," *IEEE Transactions on Aerospace and Electronic Systems*, 2015. (Submitted for review.)

3. K. M. Pesyna, Jr., D. P. Shepard, R. W. Heath, Jr., and T. E. Humphreys, "VISRTK: Fusion of camera and GNSS carrier phase measurements for fast, robust, precise, and globally-referenced mobile device pose determination," *IEEE Transactions on Signal Processing*, 2015. (In preparation.)

Conference Publications

1. K. M. Pesyna, Jr., R. W. Heath, Jr., and T. E. Humphreys, "Centimeter positioning with a smartphone-quality GNSS antenna," in *Proceedings of the ION GNSS+ Meeting*, 2014

2. K. M. Pesyna, Jr., R. W. Heath, Jr., and T. E. Humphreys, "Precision limits of low-energy GNSS receivers," in *Proceedings of the ION GNSS+ Meeting*, (Nashville, Tennessee), Institute of Navigation, 2013

3. K. M. Pesyna, Jr., Z. M. Kassas, and T. E. Humphreys, "Constructing a continuous phase time history from TDMA signals for opportunistic navigation," in *Proceedings of the IEEE/ION PLANS Meeting*, pp. 1209–1220, April 2012

4. D. P. Shepard, K. M. Pesyna, Jr., and T. E. Humphreys, "Precise augmented reality enabled by carrier-phase differential GPS," in *Proceedings of the ION GNSS Meeting*, (Nashville, Tennessee), Institute of Navigation, 2012

5. K. M. Pesyna, Jr., K. D. Wesson, R. W. Heath, Jr., and T. E. Humphreys, "Extending the reach of GPS-assisted femtocell synchronization and localization through tightly-coupled opportunistic navigation," in *IEEE GLOBECOM Workshop*, 2011

6. K. M. Pesyna Jr., Z. M. Kassas, J. A. Bhatti, and T. E. Humphreys, "Tightly-coupled opportunistic navigation for deep urban and indoor positioning," in *Proceedings of the ION GNSS Meeting*, (Portland, Oregon), Institute of Navigation, 2011

7. K. D. Wesson, K. M. Pesyna, Jr., J. A. Bhatti, and T. E. Humphreys, "Opportunistic frequency stability transfer for extending the coherence time of GNSS receiver clocks," in *Proceedings of the ION GNSS Meeting*, (Portland, Oregon), Institute of Navigation, 2010

Magazine Articles

1. K. M. Pesyna, Jr, R. W. Heath, Jr., and T. E. Humphreys, "Accuracy in the palm of your hand: Centimeter positioning with a smartphone-quality GNSS antenna," *GPS World*, vol. 26, pp. 16–31, Feb. 2015

Patents

1. D. P. Shepard, T. E. Humphreys, K. M. Pesyna, Jr., and J. A. Bhatti, "A system and method for using global navigation satellite system (GNSS) navigation and visual navigation to recover absolute position and attitude without any prior association of visual features with known coordinates," Feb. 2014. US Patent filed on Feb., 3, 2014

1.3.1 Dissertation Organization

Chapter 2 introduces the first challenge to CDGNSS on low power devices, its high power consumption, resulting from a supposed continuous signal tracking requirement. It is shown that continuous tracking can be forgone in favor of more-power-efficient measurement duty-cycling so long as a continuous carrier phase time history can be accurately reconstructed from the intermittent measurements. Accurate reconstruction means that the ambiguity introduced into the initial phase of each measurement burst as a result of the duty-cycling must be correctly resolved. This is shown to be possible through the formulation of a reconstruction technique which, at its core, solves a mixed real and integer estimation problem. The sensitivity of the technique to a set of system parameters which are set to model a typical low-power mobile receiver setup is investigated.

Chapter 3 presents an empirical analysis of data collected from the GNSS antenna of a smartphones. The chapter shows the antenna's poor multipath rejection to be the primary hindrance to fast CDGNSS positioning fixes. A centimeter-accurate positioning fix is shown to be possible, nonetheless, albeit with a significant, e.g., hundreds of seconds, initialization time. Strategies to reduce this initialization time, which involve both constrained and unconstrained antenna motion, are developed and then analyzed both in simulation and in practice.

Chapter 4 develops a joint estimation framework that combines monocular camera images with GNSS carrier phase measurements for fast, robust, precise, and globally-referenced mobile device position and orientation (pose) determination. The proposed framework augments the traditional bundle-adjustment- (BA-)-based structure from motion (SFM) algorithm with the carrier phase differential GNSS (CDGNSS) algorithm. Comparisons to existing approaches reveal that these do not combine measurements as tightly nor optimally as the proposed approach, resulting in the proposed approach having a faster, more robust, and more accurate solution. Empirical simulation results and results using real images and GNSS carrier phase measurements captured from a low-cost GNSS receiver and smartphone platform show that the proposed estimation framework (1) achieves centimeter- and sub-degree-accurate pose estimates, (2) leads to faster resolution of the CDGNSS integer ambiguities as compared to standalone CDGNSS, and (3) is able to use prior information from previously-localized point features, if available, for even faster (and oftentimes instantaneous) CDGNSS integer-ambiguity resolution.

Chapter 5 concludes this dissertation with a summary of contributions and suggestions for future research.

1.4 Nomenclature

ADOP	Ambiguity Dilution of Precision
ASR	Ambiguity Success Rate
BA	Bundle Adjustment
CAA	Correlation and Accumulation
CDGNSS	Carrier-Phase Differential GNSS
CELD	Coherent Early-Late Discriminator
CMVS	Clustering Views for Multi-View Stereo
CRLB	Cramer-Rao Lower Bound
ECEF	Earth-Centered, Earth-Fixed
ENU	East-North-Up
DD	Double Differenced
DLL	Delay-Locked Loop
GDOP	Geometric Dilution of Precision
GNSS	Global Navigation Satellite System
GPS	Global Positioning System
GRID	Generalized Radionavigation Interfusion Device
ILS	Integer Least Squares

IMU	Inertial Measurement Unit
INS	Inertial Navigation System
LAMBDA	Least-squares Ambiguity Decorrelation Adjustment
LLL	Lenstra-Lenstra-Lovász
LMA	Levenberg-Marquardt Algorithm
LOS	Line of Sight
MEMS	Microelectromechanical Systems
MVS	Multi-View Stereo
NL	Non-Linear
OU	Ornstein Uhlenbeck
PLL	Phase-Locked Loop
PPP	Precise Point Positioning
PSD	Power Spectral Density
REE	Receiver Equipment Errors
RHCP	Right-hand Circularly Polarized
RMS	Root Mean Square
RTK	Real Time Kinematic
RX	Receiver
SAP	Synthetic Aperture Processing
SIS	Signal in Space
SFM	Structure From Motion
SLAM	Simultaneous Localization and Mapping
SPS	Standard Positioning Service
SRIM	Square-root Information Matrix
SV	Satellite Vehicle

TDMA	Time Division Multiple Access
TOF	Time Of Flight
TAR	Time to Ambiguity Resolution
TTFF	Time to First Fix
TX	Transmitter
URE	User Range Error
VISRTK	Visual Real Time Kinematic
WAAS	Wide Area Augmentation System

Chapter 2

A Phase Reconstruction Technique For Low-Power Centimeter Accurate Carrier-Phase GNSS Positioning

2.1 Introduction

GNSS code-phase positioning accuracy is, under most practical conditions, limited to meter-level positioning accuracy. The multipath-free GPS signal code-phase ranging accuracy, for example, under a typical carrier-to-noise ratio of 50 dB-Hz and a typical signal integration time of 20 milliseconds is limited, as per the Cramer Rao lower bound, to 1.1 meters [12]. With multipath included, this accuracy degrades even further. To advance beyond this accuracy level, a receiver can alternatively exploit a signal's carrier-phase to compute a navigation solution. One common technique, known as carrier-phase differential GNSS (CDGNSS), developed by the surveying and precision GNSS communities differences carrier-phase measurements made between two receivers tracking the same set of satellites to achieve exquisite (centimeter-level) positioning accuracy [16, 19, 20].

Unfortunately, carrier-phase positioning solutions have challenges that are not experienced by their code-phase counterparts. For one, CDGNSS and other carrier phase positioning techniques have inherent integer ambiguities that must be resolved before a precise navigation solution can be computed. Fortunately, these

CDGNSS ambiguities are constant and estimable so-long as a receiver maintains lock on each signal's carrier phase. However, any interruption in signal data collection will introduce another set of integer ambiguities which do not remain static and are much more difficult to estimate. To avoid these new ambiguities, manufacturers have designed receivers that continuously track signals and consume power in excess of 100 mW [43]. These power consumption levels are in stark contrast to many code-phase positioning receivers which aggressively duty-cycle their code-phase measurements, such that they consume power at levels around 10 mW [23].

This chapter proposes a technique that relaxes the continuous tracking requirement of carrier-phase positioning by reconstructing a continuous phase time history from duty-cycled carrier-phase measurements. The technique estimates and removes the second set of phase ambiguities which appear as a result of the duty-cycled measurement structure. These phase ambiguities (different from the aforementioned CDGNSS ambiguities) are unknown integer-cycle offsets from the true phase that arise at the beginning of each duty-cycled measurement interval because the receiver's phase discriminator is not capable of measuring unmodeled full-cycle changes in phase that may occur when the receiver is in between measurement intervals.

There are two parts to the current chapter's contribution. First, a technique is proposed for continuous carrier phase reconstruction from duty-cycled phase measurements. The technique builds on the Kalman-filter-and-smoother-based solution to the mixed real and integer estimation problem introduced in [44], but modifies this to incorporate measurement models characterizing carrier phase errors such as the receiver front-end noise, propagation-induced phase errors, and line-of-sight range-errors. The modified solution also incorporates carrier phase structure parameters such as the measurement burst length, the measurement burst period, and the unknown whole- or fractional-cycle phase ambiguities.

Second, a rigorous evaluation of the proposed reconstruction technique is performed. This evaluation includes a Monte-Carlo-type simulation and test environment for computing the probability of successful integer ambiguity resolution as a function of common signal error and structure components. Additionally the evaluation compares the integer ambiguity resolution simulation results to previously-derived analytical upper and lower bounds.

2.2 A Brief CDGNSS Background

CDGNSS positioning is one method of exploiting the carrier phase of a GNSS signal to accurately determine a receiver's position. The technique accurately computes a three dimensional relative position between two GNSS receivers, one whose position is typically stationary and known (the reference receiver) and one whose position is to be determined (the mobile receiver) [45–47]. Fig. 2.1 shows a diagram of the CDGNSS technique. CDGNSS requires that carrier phase measurements from two receivers are collected, aligned, and twice differenced between and two receivers and pairs of satellites [48] to form so-called double-differenced measurements. From these measurements, the CDGNSS algorithm can compute a centimeter-accurate three-dimensional relative position vector between the two receivers. If one of the receivers is static and its position is precisely known, the second receiver's position can be accurately determined as well.

Double-differencing removes many of the common phase variations that would otherwise be difficult to model, e.g., receiver and satellite clock errors, a majority of the atmosphere-induced errors. As a result, the phase reconstruction technique proposed here will be performed on the double-differenced measurements, rather than

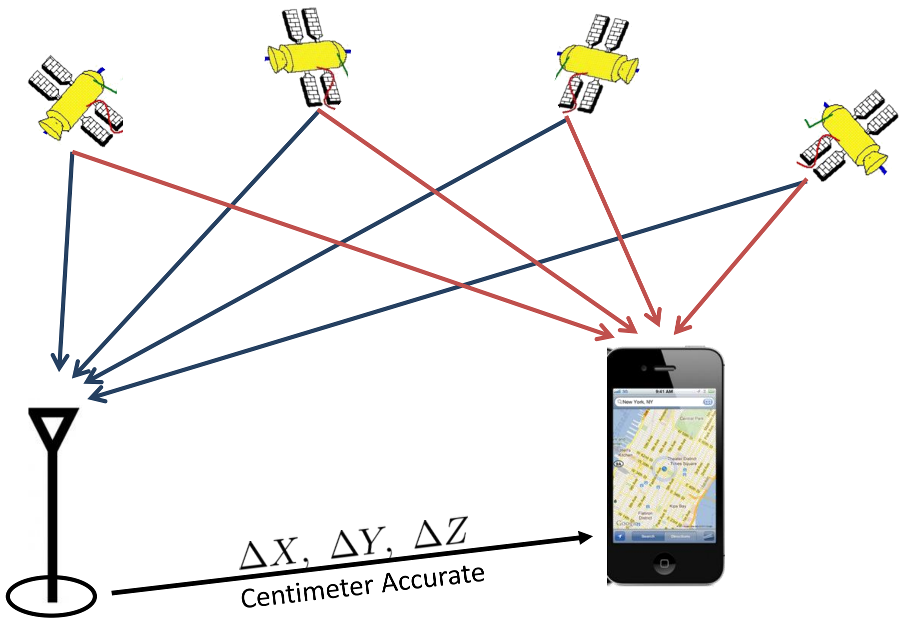

Figure 2.1: CDGNSS Framework

the undifferenced measurements. While reconstruction on double-differenced measurements is not strictly required, it does make the problem easier. Furthermore, the post-reconstructed phase time histories will be in the correct double-differenced form to perform the subsequent CDGNSS positioning solution.

2.3 Prior Work

The problem of reconstructing a continuous phase time history from intermittent, ambiguous phase measurements can be posed as a mixed real and integer estimation problem where the real parameter is the time-varying continuous phase and the integer parameters are the phase ambiguities. Prior work in mixed real and integer estimation has led to the development of a general Kalman-filter- [49] and smoother-based [44] framework which has been implemented, not for carrier-phase reconstruction, but for CDGNSS ambiguity resolution [50]. In prior work by this dissertation's author, this framework was modified to construct a continuous carrier phase from time division multiple access (TDMA) Iridium satellite communication signals, enabling their use in navigation [34]. Other authors have constructed a similar framework for fixed-baseline CDGNSS attitude determination [51]. The integer ambiguities in these problems and in the current work bear a strong resemblance to similar integer ambiguities in CDGNSS positioning and in sphere decoding, the resolution of which has been the subject of much research in the GNSS community [20, 52, 53] and in the communications community [54–56], respectively.

2.4 Carrier Phase Models

Three GNSS carrier phase models are introduced in this section; one applies before, one during, and one after carrier phase reconstruction.

2.4.1 Before Reconstruction: Undifferenced Residual Carrier Phase Model

Let the undifferenced residual carrier phase $\phi_{\mathrm{r}}(t)$ be defined as the measured phase after duty-cycled downmixing and correlation with the local signal replica. The term "residual" refers to this phase being the difference between the received carrier phase and the receiver's best prediction of the received carrier phase. The undifferenced residual carrier phase for a GNSS signal can be modeled by the following adaptation of the GPS carrier phase measurement model given in [57]:

$$
\begin{aligned}
\phi_{\mathrm{r}}(t) &\triangleq \text{received carrier phase - predicted carrier phase} \\
&= \begin{cases} \tilde{\phi}_{\mathrm{r}}(t) + \frac{1}{M}\eta(t) & \text{for } \; t_{\mathrm{b}i} \leq t < t_{\mathrm{b}i} + T_{\mathrm{b}}, \\ & \qquad\qquad i = 0, 1, ..., N_{\mathrm{b}} - 1 \\ \text{undefined} & \qquad \text{otherwise} \end{cases} \\
\tilde{\phi}_{\mathrm{r}}(t) &= \frac{1}{\lambda} r_{\mathrm{e}}(t) + \frac{c}{\lambda}[\delta t_{\mathrm{RX}}(t) - \delta t_{\mathrm{TX}}(t)] + \gamma_0 - \psi_0 \\
&\quad + \epsilon_{\mathrm{p}}(t) + v_{\phi}(t)
\end{aligned}
\tag{2.1}
$$

with the following definitions:

$\tilde{\phi}_{\mathrm{r}}(t)$ the continuous, ambiguity-free residual carrier phase, in cycles.

$t_{\mathrm{b}i}$ the start time of the i^{th} discrete phase measurement interval, or burst, in seconds.

T_{b} the burst duration, in seconds.

N_{b} the number of bursts.

M the ambiguity factor used to depict whole-cycle phase ambiguities (M=1) or fractional-cycle phase ambiguities (M >1), whichever is appropriate for the receiver setup. If the broadcast binary phase-shift keying (BPSK) GNSS navigation data symbols are provided to the receiver and the receiver knows its position and time to a fraction of a data symbol interval such that it can align the data symbols to the incoming signal to perform data symbol wipeoff, or if the receiver is tracking a data-symbol-free pilot signal, then $M = 1$; otherwise $M = 2$ due to the necessary usage of a squaring-type phase detector [58], that is, a detector which is insensitive to half-cycle phase changes induced by the data symbols.

$\eta(t)$ an integer that remains constant during each discrete phase measurement interval; i.e., $\eta(t) = n_i$ for $t_{\mathrm{b}i} \leq t < t_{\mathrm{b}i} + T_{\mathrm{b}}$. When scaled by $\frac{1}{M}$ this represents the offset of the signal's measured phase from that of the unambiguous phase at the beginning of each burst. In this chapter, n_i will be referred to as the integer ambiguity over the i^{th} burst.

λ the carrier wavelength, in meters.

$r_{\mathrm{e}}(t)$ the error in the predicted range between the receiver and transmitter, in meters. This term includes errors due to the receiver's inertial measurement unit noise, as discussed briefly in the next paragraph and in detail in section 2.7.2.1.

c the speed of light, in meters per second.

$\delta t_{\mathrm{RX}}(t)$ the difference between the predicted and actual receiver clock offset from true time, in seconds.

$\delta t_{\mathrm{TX}}(t)$ the difference between the predicted and actual transmitter clock offset from true time, in seconds.

γ_0 the initial replica carrier phase at receiver clock time 0, in cycles.

ψ_0 the initial transmitted carrier phase at satellite clock time 0.

$\epsilon_{\mathrm{p}}(t)$ the carrier phase deviation due to unmodeled propagation and multipath effects, in cycles.

$v_{\phi}(t)$ the measurement noise introduced by the receiver front-end, in cycles.

This model captures all the significant effects that cause the received carrier phase to be different from what the receiver would predict on the basis of its own clock, its assumed position, and its internal models for propagation and multipath effects, satellite motion, and satellite clock offset.

It is important to point out that to facilitate reliable reconstruction, a dynamic receiver needs to have a rough estimate of its motion. Unmodeled or poorly modeled receiver motion may result in large variations in the receiver-satellite range error $r_{\mathrm{e}}(t)$, which, as will be seen later, decreases the probability of successful reconstruction. Fortunately, a simple 3-axis inertial measurement unit (IMU) can be used to measure the receiver's 3-dimensional acceleration and angular velocity. These measurements, in conjunction with an initial position and orientation, can be integrated to predict the receiver's position changes and substantially eliminate variations in $r_{\mathrm{e}}(t)$. Of course, inertially-aided motion prediction is imperfect: noise in the IMU measurements will still produce residual variations in $r_{\mathrm{e}}(t)$, which must be accurately characterized to enable optimal phase reconstruction. Further details on IMU-aided phase reconstruction will be presented in Sections 2.7.2 and 2.9.

2.4.2 During Reconstruction: Double-Differenced Residual Carrier Phase Model

It is possible to reconstruct a continuous time phase history from measurements of the undifferenced residual carrier phase, as done in [34]. But some error sources modeled in (2.1), such as errors in the predicted transmitter and receiver clock offsets $\delta t_{\mathrm{TX}}(t)$ and $\delta t_{\mathrm{RX}}(t)$ and the propagation errors $\epsilon_{\mathrm{p}}(t)$ can often be too unstable to support reliable reconstruction. By implementing a technique known as double-differencing, where measurements between two GNSS satellites and two GNSS receivers (a rover and a reference) are differenced, many of these error sources can be entirely or substantially canceled, increasing the probability of successful reconstruction. To enable this, carrier phase measurements made by the rover and reference receivers can be passed off to a cloud server using a cellular or other wireless connection, where double-differencing (and subsequent reconstruction) can be performed. A secondary benefit of double-differencing is that the resulting reconstructed carrier phase will be in the proper form for CDGNSS, which, as mentioned earlier, is a commonly-used technique that achieves cm-accurate relative positioning by taking advantage of double differencing, not for phase reconstruction, as suggested here, but for precise positioning [16, 19, 20]. The CDGNSS positioning solution can similarly be performed in the cloud subsequent to reconstruction.

Let the double-differenced residual carrier phase $\nabla\Delta\phi^{\mathrm{ij}}_{\mathrm{rAB}}(t)$ be defined as the difference of the undifferenced residual carrier phases made between satellites i and j and receivers A and B:

$$\nabla\Delta\phi^{\mathrm{ij}}_{\mathrm{rAB}}(t) \triangleq \left[\phi^{i}_{r_A}(t) - \phi^{j}_{r_A}(t)\right] - \left[\phi^{i}_{r_B}(t) - \phi^{j}_{r_B}(t)\right]. \tag{2.2}$$

In this model, receiver B differences its undifferenced residual carrier phase measurements made by tracking satellites i and j. This difference is then subtracted from the difference made at receiver A between the same two satellites. Performing the subtractions in (4.17) and dropping the sub- and superscripts for clarity yields

$$\nabla\Delta\phi_{\mathrm{r}}(t) = \begin{cases} \nabla\Delta\tilde{\phi}_{\mathrm{r}}(t) + \frac{1}{M}\nabla\Delta\eta(t) & \text{for } \; t_{\mathrm{b}i} \leq t < t_{\mathrm{b}i} + T_{\mathrm{b}}, \\ & i = 0, 1, ..., N_{\mathrm{b}} - 1 \\ \text{undefined} & \text{otherwise} \end{cases} \tag{2.3}$$

$$\nabla\Delta\tilde{\phi}_{\mathrm{r}}(t) = \frac{1}{\lambda}\nabla\Delta r_{\mathrm{e}}(t) + \nabla\Delta\epsilon_{\mathrm{p}}(t) + \nabla\Delta v_{\phi}(t)$$

with the following new definitions:

$\nabla\Delta\tilde{\phi}_{\mathrm{r}}(t)$ the continuous, ambiguity-free double-differenced residual carrier phase, in cycles.

$\nabla\Delta\eta(t)$ an integer, constant over each measurement burst and measured in cycles, that represents the double difference of the integer $\eta(t)$ term from (2.1). In addition, $\nabla\Delta\eta(t)$ incorporates the double-difference of the initial transmitter and receiver replica carrier phases ψ_0 and γ_0 between the two satellites and two receivers. For properly designed GNSS receivers this latter double difference is an integer and remains constant during the entire dataset [57].

$\nabla\Delta r_{\mathrm{e}}(t)$ the error in the double-differenced predicted range between the two receivers and two satellites, in meters. This term includes errors due to the receiver's inertial measurement unit noise, as discussed later on in Sec. 2.7.2.1.

$\nabla\Delta\epsilon_{\mathrm{p}}(t)$ the double-differenced carrier phase deviation due to unmodeled propagation and multipath effects, in cycles.

$\nabla\Delta v_{\phi}(t)$ the double-differenced measurement noise induced by the receivers' front-ends, in cycles.

Note that the double-differencing operation has canceled the error terms $\delta t_{\mathrm{TX}}(t)$ and $\delta t_{\mathrm{RX}}(t)$ introduced in (2.1). Because of these cancellations and substantial reductions in the variations of other terms, it is more effective to apply phase reconstruction to the double-differenced residual carrier phase rather than to the undifferenced residual carrier phase. Accordingly, (2.3) will be taken to model the received carrier phase *during* reconstruction.

Fig. 2.2 illustrates the formation of the phase ambiguities $\frac{1}{M}\nabla\Delta\eta(t)$ modeled in (2.3). The upper gray trace represents the continuous and ambiguity-free double-differenced residual carrier phase $\nabla\Delta\tilde{\phi}_{\mathrm{r}}(t)$, which could be measured if both the reference and rover receivers were continually tracking GNSS signals. Instead, due to the measurement duty-cycling by one or both receivers, the measurable phase

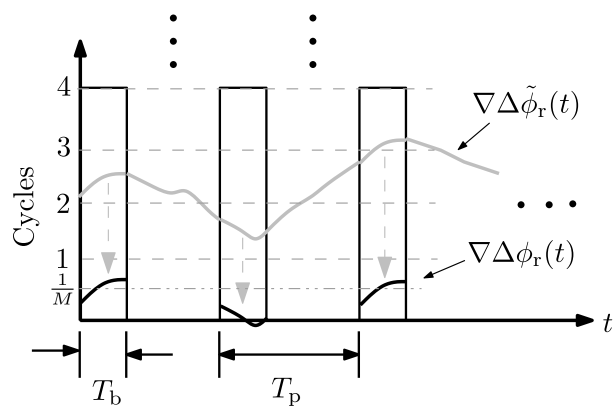

Figure 2.2: Illustration of the double differenced residual carrier phase measurements formed during each burst. The solid gray trace represents $\nabla\Delta\tilde{\phi}_{\mathrm{r}}(t)$, the continuous but unmeasurable ambiguity-free phase. To represent the measurable phase $\nabla\Delta\phi_{\mathrm{r}}(t)$, $\nabla\Delta\tilde{\phi}_{\mathrm{r}}(t)$ is structured into periodic bursts and aliased between 0 and $\frac{1}{M}$ cycles, forming the intermittent dark traces. The aliasing leads to a phase ambiguity for each burst and occurs due to the insensitivity of the receiver's phase detector to $\frac{1}{M}$-cycle phase offsets. T_{p} represents the burst period and T_{b} represents the burst duration.

becomes periodic and phase-aliased as illustrated by the lower black trace. Aliasing is caused by the insensitivity of the receiver's phase discriminator to whole- or fractional-cycle phase drifts between bursts and leads to the formation of the phase ambiguities.

2.4.3 After Reconstruction: Reconstructed Double-Differenced Carrier Phase Model

One final model is presented here to characterize the double-differenced carrier phase after reconstruction. Although this model is not used during reconstruction, it nicely illustrates the effects of reconstruction errors and relates them to the so-called "ideal" or error-free reconstructed carrier phase. In this model, the reconstructed double-differenced carrier phase $\nabla\Delta\phi_{\mathrm{R}}(t)$ is given by

$$\nabla\Delta\phi_{\mathrm{R}}(t) =\nabla\Delta\phi_{\mathrm{ideal}}(t) + \beta(t) + \frac{1}{M}\left[\nabla\Delta\eta(t) - \nabla\Delta\hat{\eta}(t)\right]. \tag{2.4}$$

Here, the following new definitions apply:

$\nabla\Delta\phi_{\mathrm{ideal}}(t)$ the ideal double-differenced residual carrier phase. This term represents the double-differenced carrier phase as it would appear if it were perfectly reconstructed, i.e., if the receivers involved in the double-differencing were continuously tracking the GNSS signals and there was no measurement noise.

$\beta(t)$ the non-ambiguity related reconstruction errors, measured in cycles. This term encompasses all non-ambiguity-related deviations of $\nabla\Delta\phi_{\mathrm{R}}(t)$ from $\nabla\Delta\phi_{\mathrm{ideal}}(t)$.

$\nabla\Delta\hat{\eta}(t)$ the reconstruction technique's best estimate of the time-varying double-differenced integer ambiguity term $\nabla\Delta\eta(t)$, measured in cycles. The difference

$\frac{1}{M}[\nabla\Delta\eta(t) - \nabla\Delta\hat{\eta}(t)]$ is the time-varying reconstruction error that arises during ambiguity resolution.

$\nabla\Delta\phi_{\mathrm{R}}(t)$ is the reconstruction technique's best estimate of $\nabla\Delta\phi_{\mathrm{ideal}}(t)$, the continuous, noise-free, and ambiguity-free double-differenced residual carrier phase. Errors in phase reconstruction cause $\nabla\Delta\phi_{\mathrm{R}}(t)$ to deviate, sometimes significantly, from $\nabla\Delta\phi_{\mathrm{ideal}}(t)$. This deviation is modeled by $\beta(t)$ and $\frac{1}{M}[\nabla\Delta\eta(t) - \nabla\Delta\hat{\eta}(t)]$, the non-ambiguity and ambiguity-related reconstructed errors, respectively. Typically, the second term dominates, as errors in ambiguity resolution tend to be much larger than non-ambiguity errors.

Because the receiver only has access to the intermittent ambiguous phase $\nabla\Delta\phi_{\mathrm{r}}(t)$, as represented by the lower dark trace in Fig. 2.2, the reconstruction algorithm must determine in which whole-cycle vertical partition (or fractional-cycle partition if $M > 1$) each solid black curve would reside if $\nabla\Delta\phi_{\mathrm{r}}(t)$ were instead unambiguous. That is, it must determine the time-varying integer-valued phase-ambiguity term $\nabla\Delta\eta(t)$. Fig. 2.3 helps to illustrate this challenge. The horizontal dashed lines illustrate vertical partitions in which the reconstructed phase $\nabla\Delta\phi_{\mathrm{R}}(t)$ could lie. Here $M = 1$, so each partition is 1 cycle in height. These partitions repeat infinitely in each direction along the vertical axis. This leads to an infinite number of possible phase time histories, or trajectories, 16 of which are depicted in the figure. However, just one of these trajectories accurately depicts the continuous, ambiguity-free phase time history $\nabla\Delta\tilde{\phi}_r(t)$. It becomes the task of the reconstruction algorithm to use past, present, and future measurements of $\nabla\Delta\phi_{\mathrm{r}}(t)$ to resolve the phase ambiguities and attempt to reconstruct $\nabla\Delta\tilde{\phi}_r(t)$. If one or more ambiguities are resolved incorrectly, an incorrect reconstructed phase trajectory would be chosen, leading $\nabla\Delta\phi_{\mathrm{R}}(t)$ to deviate significantly ($\geq \frac{1}{M}$ cycles) from $\nabla\Delta\tilde{\phi}_r(t)$. Such errors will degrade the utility of the reconstructed phase time

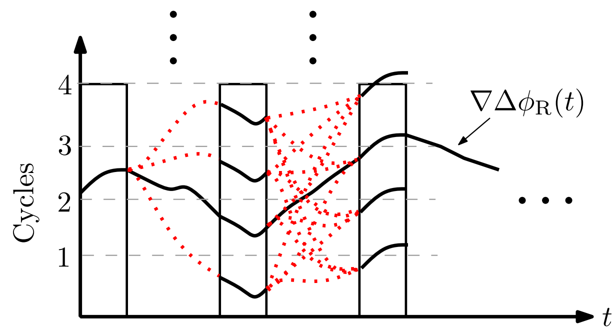

Figure 2.3: Illustration of possible reconstructed phase trajectories, only 1 of which corresponds to the true trajectory. It is the job of the reconstruction algorithm to reconstruct the true trajectory using measurements of the periodic and aliased double-differenced residual carrier phase $\nabla\Delta\phi_{\rm r}(t)$, which, in this particular illustration, has 1 cycle phase ambiguities, i.e., $M = 1$.

history in the context of a CDGNSS solution, as they will lead to a positioning solution that is no longer cm-accurate (see Sec. 2.9). Accordingly, it becomes useful to examine the probability of correctly resolving the phase ambiguities; this will be done both theoretically and empirically in subsequent sections.

2.5 Reconstruction Technique

This section describes the proposed technique for reconstructing a continuous carrier phase time history from intermittent phase measurements made by the receiver. The technique takes the intermittent double-differenced residual carrier phase measurements $\nabla\Delta\phi_{\rm r}(t)$ and forms a reconstructed double-differenced carrier phase time history $\nabla\Delta\phi_{\rm R}(t)$. It resolves phase ambiguities with an integer least-squares solver and optimally "stitches" discrete phase measurements together with a Kalman filter and smoother. Square-root information implementations of the filter and smoother ensure that phase reconstruction is performed in an accurate and computationally-efficient manner [44, 59]. For a tutorial on square-root information filtering and its relationship to traditional Kalman filtering, see [60].

2.5.1 Estimation State and Dynamics and Measurement Model

This section describes the reconstruction filter and smoother's state as well as its dynamics and measurement models.

2.5.1.1 State

The state has a real-valued component that models the noise- and ambiguity-free double-differenced residual carrier phase, and an integer-valued component that models the phase ambiguities. The real-valued state component at time t_k is denoted $\mathbf{x}_k$, where $t_k = kT$ and $T \leq T_\mathrm{b}$ is the time between consecutive filter and smoother updates. This component can be expressed as

$$\mathbf{x}_k = [\nabla\Delta\phi_{\mathrm{ideal},k}, \omega_k]^\mathsf{T} \tag{2.5}$$

with the following definitions:

$\nabla\Delta\phi_{\mathrm{ideal},k}$ the discrete-time noise- and ambiguity-free ideal double-differenced residual carrier phase at time t_k, in cycles, i.e., $\nabla\Delta\phi_{\mathrm{ideal},k} = \nabla\Delta\phi_{\mathrm{ideal}}(t_k)$, where $\nabla\Delta\phi_{\mathrm{ideal}}(t)$ was defined in (2.4).

ω_k the rate of change of $\nabla\Delta\phi_{\mathrm{ideal}}(t)$ at time t_k, in Hz.

The integer-valued state component $\mathbf{n}_k$ at time t_k can be expressed as

$$\mathbf{n}_k = [n_1, n_2, \ldots, n_{i_k}]^\mathsf{T} \tag{2.6}$$

with the following definitions:

$\mathbf{n}_k$ an $i_k \times 1$ vector of integers, one for each measurement burst that began between time 0 and t_k.

n_{i_k} the integer corresponding to the i_k^{th} measurement burst.

i_k a counter representing the number of measurement bursts that begin at or before time t_k.

2.5.1.2 Dynamics Model

The real and integer components of the state evolve separately; thus their dynamics will be modeled separately. The real-valued state component $\mathbf{x}_k$ is assumed to evolve as a first-order Gauss-Markov process with process noise representing the variations due to $\nabla\Delta r_{\mathrm{e}}(t)$ and $\nabla\Delta\epsilon_{\mathrm{p}}(t)$ from (2.3). The integer-valued state component $\mathbf{n}_k$ evolves under the assumption that a new ambiguity is introduced with each measurement burst.

The following models describe the time evolution of the real- and integer-valued state components:

$$\mathbf{x}_{k+1} = \mathbf{\Phi}\mathbf{x}_k + \mathbf{\Gamma}\mathbf{w}_k \tag{2.7}$$

$$\mathbf{n}_{k+1} = \begin{cases} \begin{bmatrix} \mathbf{n}_k \\ n_{i_{k+1}} \end{bmatrix} & \text{if a new burst began within the interval } (t_k, t_{k+1}] \\ \begin{bmatrix} \mathbf{n}_k \end{bmatrix} & \text{otherwise} \end{cases} \tag{2.8}$$

with the following definitions:

$\mathbf{\Phi}$ the state transition matrix.

$\mathbf{\Gamma}$ the process noise influence matrix.

$\mathbf{w}_k$ the process noise at time t_k, modeled as a discrete-time zero-mean $\mathbf{Q}$ covariance Gaussian random vector, i.e., $\mathbf{w}_k \sim \mathcal{N}(\mathbf{0}, \mathbf{Q})$.

$\mathbf{Q}$ the process noise covariance matrix.

The state transition matrix for the real-valued state models standard Euler integration from t_k to t_{k+1}:

$$\mathbf{\Phi} = \begin{bmatrix} 1 & T \\ 0 & 1 \end{bmatrix}. \tag{2.9}$$

The process noise influence is defined as

$$\mathbf{\Gamma} = \begin{bmatrix} 1 & 0 & 0 \\ 0 & 1 & 0 \end{bmatrix} \tag{2.10}$$

and the process noise covariance matrix is defined as

$$\mathbf{Q} = S_g f_0^2 \begin{bmatrix} \frac{T^3}{3} & \frac{T^2}{2} & \frac{T^3}{8} \\ \frac{T^2}{2} & T & \frac{T^2}{6} \\ \frac{T^3}{8} & \frac{T^2}{6} & \frac{T^3}{20} \end{bmatrix} + S_f f_0^2 \begin{bmatrix} T & 0 & \frac{T}{2} \\ 0 & 0 & 0 \\ \frac{T}{2} & 0 & \frac{T}{3} \end{bmatrix}, \tag{2.11}$$

where f_0 is the GNSS signal's nominal carrier frequency, in Hz. The quantities S_g and S_f parameterize the combined phase instability caused by the process noise error components in (2.3), namely $\nabla\Delta r_{\mathrm{e}}(t)$ and $\nabla\Delta\epsilon_{\mathrm{p}}(t)$. The model for the evolution of the real-valued state elements in (2.7) with the process-noise covariance defined by (3.17) follows a two-state Gauss-Markov model commonly used to describe clock-error-induced phase variations (see [61], Ch. 11). This model will be discussed further in Sec. 2.7.1. Note that $\mathbf{w}_k$ is of dimension 3-by-1 while $\mathbf{x}_k$ is of dimension 2-by-1. The third element in $\mathbf{w}_k$ and, correspondingly, the third row and column in $\mathbf{Q}$ is a standard way to model the average of the phase process noise over the interval $t_{k-1} < t \leq t_k$ [62] and will be needed in the measurement model discussed next.

2.5.1.3 Measurement Model

The filter ingests measurements y_k of the double-differenced residual carrier phase and relates these measurements to its state. Each measurement y_k represents the average of $\nabla\Delta\phi_{\mathrm{r}}(t)$ over the interval $t_{k-1} < t \leq t_k$, i.e., $y_k = \frac{1}{T}\int_{t_{k-1}}^{t_k} \nabla\Delta\phi_{\mathrm{r}}(t)$. It should be noted that filter measurement updates occur only within measurement bursts when measurements are available. The filter's measurement model relates y_k to the real- and integer-valued state components $\mathbf{x}_k$ and $\mathbf{n}_k$ and to the process-noise $\mathbf{w}_{k-1}$:

$$y_k = \begin{cases} \tilde{\mathbf{H}}_{\mathrm{x}}\mathbf{x}_k + \tilde{\mathbf{H}}_{\mathrm{n}k}\mathbf{n}_k + \tilde{\mathbf{H}}_{\mathrm{w}}\mathbf{w}_{k-1} + v_k & \text{for } t_{\mathrm{b}i} \leq t_k < t_{\mathrm{b}i} + T_{\mathrm{b}}, \\ & i = 0, 1, ..., N_{\mathrm{b}} - 1 \\ \text{undefined} & \text{otherwise} \end{cases} \tag{2.12}$$

with the following new definitions:

$\tilde{\mathbf{H}}_{\mathrm{x}}$ the measurement sensitivity matrix for the real-valued state components.

$\tilde{\mathbf{H}}_{\mathrm{n}k}$ the measurement sensitivity matrix for the integer-valued state components at time t_k.

$\tilde{\mathbf{H}}_{\mathrm{w}}$ the measurement sensitivity matrix for the process noise.

v_k the average of the continuous-time double-differenced measurement noise over the interval $t_{k-1} < t \leq t_k$, i.e., $v_k = \frac{1}{T}\int_{t_{k-1}}^{t_k} \nabla\Delta v_\phi(t)$. v_k is modeled as a zero-mean discrete-time Gaussian white noise process, $v_k \sim \mathcal{N}(0, \sigma_{\phi k}^2)$, where $\sigma_{\phi k}^2$ has a nonlinear relationship with the mean carrier-to-noise ratio over the interval $(C/N_0)_k$, but for high $(C/N_0)_k$ converges to $\sigma_{\phi k}^2 = \frac{1}{2T(C/N_0)_k}$ [63].

The measurement sensitivity matrices can be expanded as

$$\tilde{\mathbf{H}}_{\mathrm{x}} = \begin{bmatrix} 1 & -\dfrac{T}{2} \end{bmatrix} \tag{2.13}$$

$$\tilde{\mathbf{H}}_{\mathrm{n}k} = \begin{bmatrix} 0 & 0 & \dots & 0 & \dfrac{1}{M} \end{bmatrix} \tag{2.14}$$

$$\tilde{\mathbf{H}}_{\mathrm{w}} = \begin{bmatrix} -1 & \dfrac{T}{2} & 1 \end{bmatrix} \tag{2.15}$$

where T is the time between consecutive filter updates, as defined previously, and M is the ambiguity factor defined in (2.1). Two features of the $1 \times i_k$ matrix $\tilde{\mathbf{H}}_{\mathrm{n}k}$ are noteworthy. First, the $\frac{1}{M}$ factor in its last element allows the integer-valued state $\mathbf{n}_k$ to relate to a whole-cycle ($M = 1$) or a fractional-cycle ($M > 1$) phase ambiguity. Second, $\tilde{\mathbf{H}}_{\mathrm{n}k}$ has 0s in all but its last element to ensure that the measurements made during burst i_k are only affected by the most recent integer ambiguity n_{i_k} of $\mathbf{n}_k$. Because y_k is an average, $\tilde{\mathbf{H}}_{\mathrm{w}}$ is needed to model the accumulation of process noise into the measurement [62].

2.5.2 Cost Function

Optimal channel-by-channel estimates of the state components $\mathbf{x}_k$ and $\mathbf{n}_k$ for $1 \leq k \leq K$ can be obtained according to the maximum *a posteriori* criterion based on all measurements y_k from $k = 1$ to K by determining the state and process noise time histories that minimize a certain cost function subject to the dynamics models in (2.7) and (2.8). For numerical robustness, a square-root-information approach is adopted [44, 59]. Let the square-root information equation for the *a priori* estimate of the real-valued state component $\mathbf{x}_0$ at $k = 0$ be given by

$$\mathbf{z}_{\mathrm{x}0} = \mathbf{R}_{\mathrm{xx}0}\mathbf{x}_0 + \mathbf{v}_{\mathrm{x}0} \tag{2.16}$$

with the following definitions:

$\mathbf{z}_{\mathrm{x}0}$ the *a priori* nonhomogeneous term that stores information about $\mathbf{x}_0$.

$\mathbf{R}_{\mathrm{x}0k}$ the *a priori* square-root information matrix for $\mathbf{x}_0$.

$\mathbf{v}_{\mathrm{x}0}$ the error corresponding to $\mathbf{x}_0$, a sample from a discrete-time zero-mean, unity covariance Gaussian white noise process, i.e., $\quad \mathbf{v}_{\mathrm{x}0} \sim \mathcal{N}(\mathbf{0}, \mathbf{I})$.

No *a priori* information is assumed to be available for the integer-valued state component $\mathbf{n}$. Let the square-root information equation for the *a priori* estimate of the process noise $\mathbf{w}_k$ at each time index k be given by

$$\mathbf{z}_{\mathrm{w}k} = 0 = \mathbf{R}_{\mathrm{ww}}\mathbf{w}_k + \mathbf{v}_{\mathrm{w}k} \tag{2.17}$$

with the following definitions:

$\mathbf{z}_{\mathrm{w}k}$ the *a priori* nonhomogeneous term that stores information about $\mathbf{w}_k$.

$\mathbf{R}_{\mathrm{ww}}$ the *a priori* square-root information matrix for $\mathbf{w}_k$, defined as $\mathbf{R}_{\mathrm{ww}} = \mathbf{Q}^{-\frac{1}{2}}$, where $\mathbf{Q}$ is defined in (3.17).

$\mathbf{v}_{\mathrm{w}k}$ the error corresponding to $\mathbf{w}_k$, a sample from a discrete-time zero-mean, unity covariance Gaussian white noise process, i.e., $\quad \mathbf{v}_{\mathrm{w}k} \sim \mathcal{N}(\mathbf{0}, \mathbf{I})$.

The equation in (2.17) is set equal to zero because the process noise is assumed to be zero-mean and thus solving (2.17) for the *a priori* process noise estimate $\hat{\mathbf{w}}_k$ should yield $\hat{\mathbf{w}}_k = 0$. Now, let the measurement model in (3.12) be normalized by multiplying both sides by $\sigma_{\phi k}^{-1}$. This normalized measurement model, now in standard square-root equation form, is written

$$z_k = \mathbf{H}_{\mathrm{x}k}\mathbf{x}_k + \mathbf{H}_{\mathrm{n}k}\mathbf{n}_k + \mathbf{H}_{\mathrm{w}k}\mathbf{w}_{k-1} + v_{zk} \tag{2.18}$$

with the following definitions:

z_k the normalized nonhomogeneous term defined as $z_k = \sigma_{\phi k}^{-1} y_k$.

$\mathbf{H}_{\mathrm{x}k}$ the normalized measurement sensitivity matrix for the real-valued state components at time t_k, defined as $\mathbf{H}_{\mathrm{x}k} = \sigma_{\phi k}^{-1} \tilde{\mathbf{H}}_{\mathrm{x}}$

$\mathbf{H}_{\mathrm{n}k}$ the normalized measurement sensitivity matrix for the integer-valued state components at time t_k, defined as $\mathbf{H}_{\mathrm{n}k} = \sigma_{\phi k}^{-1} \tilde{\mathbf{H}}_{\mathrm{n}k}$.

$\mathbf{H}_{\mathrm{w}k}$ the normalized measurement sensitivity matrix for the process-noise at time t_k, defined as $\mathbf{H}_{\mathrm{w}k} = \sigma_{\phi k}^{-1} \tilde{\mathbf{H}}_{\mathrm{w}}$.

v_{zk} the normalized measurement noise at time t_k, modeled as a zero-mean, unit variance, discrete-time, Gaussian white noise process, $v_{zk} \sim \mathcal{N}(0, 1)$.

Like y_k in (3.12), z_k is undefined between bursts.

Given (2.16), (2.17), and (2.18), the phase reconstruction problem can be posed as follows:

$$\begin{aligned} \underset{\substack{\mathbf{x}_i, \mathbf{n}_i \ \{i:\ 0<i\leq K\} \\ \mathbf{w}_i \ \{i:\ 0\leq i<K\}}}{\text{minimize}} \quad J = \quad & \underbrace{||\mathbf{R}_{\mathrm{xx}0}\mathbf{x}_0 - \mathbf{z}_{\mathrm{x}0}||^2}_{\textit{A priori} \text{ information}} + \underbrace{\sum_{k=0}^{K-1} ||\mathbf{R}_{\mathrm{ww}}\mathbf{w}_k||^2}_{\text{Process noise}} \\ & + \underbrace{\sum_{k=1}^{K} ||\mathbf{H}_{\mathrm{x}k}\mathbf{x}_k + \mathbf{H}_{\mathrm{n}k}\mathbf{n}_k + \mathbf{H}_{\mathrm{w}k}\mathbf{w}_{k-1} - z_k||^2}_{\text{Measurements}} \end{aligned} \tag{2.19}$$

subject to the state dynamics models in (2.7) and (2.8).

A solution to (2.19) can be found by breaking the reconstruction process into three stages: filtering, ambiguity resolution, and smoothing.

2.5.3 Filtering

Filtering is the first stage in the reconstruction process. Filter estimates of the state at each time index k will be produced by making optimal use of the measurement at time t_k (if within a measurement burst) and all measurements prior to t_k. It can be shown through a series of orthogonal transformations on (2.19) that at each time index k, the filter's best estimate of the real- and integer-valued state elements can be found by choosing $\mathbf{x}_k$ and $\mathbf{n}_k$ to minimize the partial cost functional [64]

$$\begin{aligned} J_k\left(\mathbf{x}_k, \mathbf{n}_k\right) = & \underbrace{\left\|\mathbf{R}_{\mathrm{xx}k}\mathbf{x}_k + \mathbf{R}_{\mathrm{xn}k}\mathbf{n}_k - \mathbf{z}_{\mathrm{x}k}\right\|^2}_{\text{Term involving the integer- and real-valued states}} \\ & + \underbrace{\left\|\mathbf{R}_{\mathrm{nn}k}\mathbf{n}_k - \mathbf{z}_{\mathrm{n}k}\right\|^2}_{\text{Term involving only the integer-valued state}} + \underbrace{\sum_{i=1}^{k}\left\|z_{\mathrm{r}i}\right\|^2}_{\text{Residual term}} \end{aligned} \tag{2.20}$$

with the following definitions:

$\mathbf{z}_{\mathrm{x}k}$ the nonhomogeneous term corresponding to the real-valued state component at time t_k.

$\mathbf{z}_{\mathrm{n}k}$ the nonhomogeneous term corresponding to the integer-valued state component at time t_k.

$z_{\mathrm{r}i}$ the residual nonhomogeneous term at time $t_{\mathrm{b}i}$, $1 \leq i \leq k$.

$\mathbf{R}_{\mathrm{xx}k}$ the square-root information matrix corresponding to $\mathbf{x}_k$ and $\mathbf{z}_{\mathrm{x}k}$ at time t_k.

$\mathbf{R}_{\mathrm{xn}k}$ the square-root information matrix corresponding to $\mathbf{n}_k$ and $\mathbf{z}_{\mathrm{x}k}$ at time t_k.

$\mathbf{R}_{\mathrm{nn}k}$ the square-root information matrix corresponding to $\mathbf{n}_k$ and $\mathbf{z}_{\mathrm{n}k}$ at time t_k.

$J_k\left(\mathbf{x}_k, \mathbf{n}_k\right)$ is the contribution to the overall cost that is obtained after filtering measurements z_1 to z_k. Each term on the right-hand side of (3.26) is produced during the filter's measurement updates during which *a priori* state estimates are combined with measurements. Minimization of (3.26) proceeds as follows: First, one determines the integer-valued vector state estimate $\hat{\mathbf{n}}_k$ that minimizes the second term of (3.26), the term involving only the integer-valued state. This estimate can be determined efficiently using the integer least-squares techniques discussed in the next section. Once determined, $\hat{\mathbf{n}}_k$ is inserted into the first term, the term involving both the integer- and real-valued states. At this point, it is possible to determine the real-valued state estimate $\hat{\mathbf{x}}_k$ that reduces the first term to zero, minimizing (3.26).

2.5.4 Integer Ambiguity Resolution

Integer ambiguity resolution is the second stage in the reconstruction process and must be performed before the real-valued state component can be determined. At any time index k during filtering, the cost functional of the form in (3.26) can be minimized to provide real-time (causal) estimates of the real- and integer-valued state components. This entails first minimizing the following cost function involving the integer-valued state

$$J_{\mathrm{n}}\left(\mathbf{n}_k\right) = \left\|\mathbf{R}_{\mathrm{nn}k}\mathbf{n}_k - \mathbf{z}_{\mathrm{n}k}\right\|^2 . \tag{2.21}$$

This minimization can be posed as an integer least-squares (ILS) problem whose solution has been shown to be NP-hard and has been studied extensively [20, 53, 54, 65]. ILS solution algorithms are optimal in the sense that out of the set of all admissible estimators, they have the largest possible probability of successful integer ambiguity resolution [66]. For the definition of an admissible estimator, see [66]. Solution algorithms accept the matrix $\mathbf{R}_{\mathrm{nn}k}$ and the vector $\mathbf{z}_{\mathrm{n}k}$ from the filter and solve for the vector $\mathbf{n}_k$ that minimizes (2.21); calling this minimizing vector $\hat{\mathbf{n}}_k$.

If desired, to save computational resources, the minimizing procedure to estimate $\mathbf{n}_k$ only need be performed once, at the end of the dataset at time index K. This is because $\hat{\mathbf{n}}_k$ is a vector that contains integer estimates for all ambiguities up to through time k. Real-time requirements, however, may require $\hat{\mathbf{n}}_k$ to be determined more often, e.g., after each filter update, as the real-valued state components $\mathbf{x}_k$ may be needed in real-time and these cannot be determined without first determining $\hat{\mathbf{n}}_k$.

The ILS solution algorithm can be interpreted geometrically as a closest point lattice search [53], where the lattice is defined by the $n \times n$ dimensional square-root information matrix $\mathbf{R}_{\mathrm{nn}k}$ and the n-dimensional vector of integers $\mathbf{n}_k$. The product $\mathbf{R}_{\mathrm{nn}k}\mathbf{n}_k$ forms an n-dimensional vector which spans the lattice. Given $\mathbf{R}_{\mathrm{nn}k}$ and $\mathbf{z}_{\mathrm{n}k}$, the ILS solution amounts to finding the closest lattice point $\mathbf{R}_{\mathrm{nn}k}\mathbf{n}_k$ to $\mathbf{z}_{\mathrm{n}k}$ [54]:

$$\hat{\mathbf{n}}_k = \underset{\mathbf{n}_k \in \mathbb{Z}^{i_k}}{\operatorname{argmin}} \left\| \mathbf{R}_{\mathrm{nn}k}\mathbf{n}_k - \mathbf{z}_{\mathrm{n}k} \right\|^2 . \tag{2.22}$$

The solution procedure can be broken into a reduction step and a search step. The reduction step attempts to reduce the search space; the search step searches for the lowest-cost solution. For the reduction step, the least-squares ambiguity decorrelation adjustment method (LAMBDA) [20] and the Lenstra-Lenstra-Lovász (LLL) reduction [67] are widely used in practice [52, 53]. Implementations of both the LAMBDA method [68] and the LLL method [69] were compared by this dissertation's author. They were found to offer comparable computational performance. For the search step, the solution algorithm introduced in [68] has been used for the results presented in this chapter.

2.5.5 Smoothing

Smoothing is the third stage in the phase reconstruction process. Although a reconstructed carrier phase time history can be determined by solving for the time-varying real-valued state component $\mathbf{x}_k$ after only the first two stages, smoothing is acausal and thus enables past, present, and future phase measurements to be incorporated into the estimates of $\mathbf{x}_k$ at each time instant. To initialize the smoother, the integer ambiguity vector estimate $\hat{\mathbf{n}}_K$ after the final measurement update is determined as described previously and then incorporated, together with $\mathbf{R}_{\mathrm{xn}K}$, to form the smoother's initial nonhomogeneous term $\mathbf{z}^{\star}_{\mathrm{x}K}$ and initial square-root information matrix $\mathbf{R}^{\star}_{\mathrm{xn}K}$ as follows:

$$\mathbf{z}^{\star}_{\mathrm{x}K} = \mathbf{z}_{\mathrm{x}K} - \mathbf{R}_{\mathrm{xn}K}\hat{\mathbf{n}}_K \tag{2.23}$$

$$\mathbf{R}^{\star}_{\mathrm{xx}K} = \mathbf{R}_{\mathrm{xx}K}. \tag{2.24}$$

It should be noted that because the smoother is initialized with the already-resolved integer ambiguity vector $\hat{\mathbf{n}}_K$, a quantity determined solely from filter outputs as described in Sec. 2.5.4, smoothing has no effect on integer ambiguity resolution. Consequently, the smoother's contribution to phase reconstruction is a minor one; smoothing acts only to remove abrupt innovation-induced dynamics from $\mathbf{x}_k$ that do not conform to the filter's state dynamics model (see [34], Fig. 5). Furthermore, because smoothing is performed over a batch of measurements, a natural lag is introduced between when the measurements are taken and when the smoothed reconstructed double-differenced carrier phase estimates are formed. As a result, for real-time systems, smoothing may be forgone in favor of removing this lag. Computational lag due to filtering, ambiguity resolution, and subsequent CDGNSS processing, however, will still persist.

After this initialization, the smoother begins its processing. At each time index k, $0 \leq k \leq K$, the smoother ingests $\mathbf{z}^{\star}_{\mathrm{x}k}$ and $\mathbf{R}^{\star}_{\mathrm{xx}k}$ from the previous smoother update as well the process noise terms $\mathbf{z}_{\mathrm{w},k-1}$, $\mathbf{R}_{\mathrm{ww}}$, $\mathbf{R}_{\mathrm{wx},k-1}$, and $\mathbf{R}_{\mathrm{wn},k-1}$ from the filtering stage and outputs $\mathbf{R}^{\star}_{\mathrm{xx},k-1}$ and $z^{\star}_{\mathrm{x},k-1}$. It then decrements k by 1 and repeats, working backward from index K until it reaches $k = 0$. Smoothed state estimates $\mathbf{x}^{\star}_k$ for $k = 0, 1, \ldots, K$ can then be computed from the smoother output terms as follows:

$$\mathbf{x}_k^\star = (\mathbf{R}_{\mathrm{xx}k}^\star)^{-1}\mathbf{z}_{\mathrm{x}k}^\star. \tag{2.25}$$

The minimum cost after smoothing can be shown to be [64]

$$\begin{aligned} J\left(\{\mathbf{x}_i^\star\}_{i=1}^K, \hat{\mathbf{n}}_K, \{\mathbf{w}_i^\star\}_{i=0}^{K-1}\right) = &\underbrace{\|\mathbf{R}_{\mathrm{nn}K}\hat{\mathbf{n}}_K - \mathbf{z}_{\mathrm{n}K}\|^2}_{\text{Integer-fit error}} \\ &+ \underbrace{\sum_{i=1}^K \|z_{\mathrm{r}i}\|^2}_{\text{Residual error}}. \end{aligned} \tag{2.26}$$

2.6 Bounds on the Probability of Successful Ambiguity Resolution

In Section 2.5.4, it was shown that the reconstruction algorithm uses an integer least-squares solver to determine the vector of integer ambiguities $\mathbf{n}_k$ which minimizes (2.21). However, because of noise, there is no guarantee that the minimizing $\mathbf{n}_k$, denoted $\hat{\mathbf{n}}_k$, equals the true integer phase ambiguities of the double-differenced residual carrier phase trajectory. This section discusses the probability of successful ambiguity resolution P_c, or the probability that $\hat{\mathbf{n}}_k$ equals $\mathbf{n}_k$. Only bounds on P_c are presented, as determination of the exact probability is NP-hard.

As discussed previously, minimizing (2.21) is equivalent to finding the closest lattice point $\mathbf{R}_{\mathrm{nn}k}\mathbf{n}_k$ to $\mathbf{z}_{\mathrm{n}k}$, which, in turn, is equivalent to minimizing the ambiguity measurement noise vector $\mathbf{v}_{\mathrm{n}k}$ in the following ambiguity square-root information equation:

$$\mathbf{z}_{\mathrm{n}k} = \mathbf{R}_{\mathrm{nn}k}\mathbf{n}_k + \mathbf{v}_{\mathrm{n}k}, \quad \mathbf{v}_{\mathrm{n}k} \sim \mathcal{N}(\mathbf{0}, \mathrm{I}). \tag{2.27}$$

The vector of integers $\hat{\mathbf{n}}_k$ that corresponds to the closest lattice point will be equal to the true vector of integer ambiguities $\mathbf{n}_k$ if and only if the ambiguity measurement noise $\mathbf{v}_{\mathrm{n}k}$ is such that $\mathbf{z}_{\mathrm{n}k}$ remains closer to the lattice point $\mathbf{R}_{\mathrm{nn}k}\mathbf{n}_k$ than any other point in the lattice. This is equivalent to $\mathbf{R}_{\mathrm{nn}k}\mathbf{n}_k + \mathbf{v}_{\mathrm{n}k}$ falling within the *Voronoi cell* $\mathcal{V}_{\mathrm{Rnn}k}$ of $\mathbf{R}_{\mathrm{nn}k}\mathbf{n}_k$. $\mathcal{V}_{\mathrm{Rnn}k}$ is formally defined as the collection of real-valued ℓ-dimensional points (where $\ell = i_k$) closer to $\mathbf{R}_{\mathrm{nn}k}\mathbf{n}_k$ than any other lattice point. Under this framework, the probability of correct integer ambiguity resolution P_{c} can be defined as [53]:

$$P_{\mathrm{c}} = \Pr\left\{\mathbf{R}_{\mathrm{nn}k}\mathbf{n}_k + \mathbf{v}_{\mathrm{n}k} \in \mathcal{V}_{\mathrm{Rnn}k}\right\} \quad \mathbf{v}_{\mathrm{n}k} \sim \mathcal{N}(\mathbf{0}, \mathrm{I}). \tag{2.28}$$

Because the lattice has a periodic structure, $\mathcal{V}_{\mathrm{Rnn}k}$ is merely a translation of the origin's *Voronoi cell* $\mathcal{V}_{0k}$ by $\mathbf{R}_{\mathrm{nn}k}\mathbf{n}_k$. Thus P_{c} can be written equivalently as

$$P_{\mathrm{c}} = \Pr\left\{\mathbf{v}_{\mathrm{n}k} \in \mathcal{V}_{0k}\right\} \quad \mathbf{v}_{\mathrm{n}k} \sim \mathcal{N}(\mathbf{0}, \mathrm{I}). \tag{2.29}$$

P_{c} is now a function of solely the Gaussian random ambiguity noise vector $\mathbf{v}_{\mathrm{n}k}$ and can be precisely determined by integrating the probability distribution function of $\mathbf{v}_{\mathrm{n}k}$ over $\mathcal{V}_{0k}$ [70]:

$$\begin{aligned} P_{\mathrm{c}} &= \int_{\mathcal{V}_{0k}} \mathcal{N}(\mathbf{v}_{\mathrm{n}k}; \mathbf{0}, \mathrm{I}) \mathrm{d}\mathbf{v}_{\mathrm{n}k} \\ &= \int_{\mathcal{V}_{0k}} \frac{1}{(2\pi)^{\frac{n}{2}}} \exp\left(-\frac{1}{2}\left\|\mathbf{v}_{\mathrm{n}k}\right\|^2\right) \mathrm{d}\mathbf{v}_{\mathrm{n}k}. \end{aligned} \tag{2.30}$$

In (2.30), $\mathcal{N}(\mathbf{v}_{\mathrm{n}k}; \mathbf{0}, \mathrm{I})$ is the multivariate normal distribution and $\|\cdot\|$ is the $L2$-norm. Unfortunately, determining $\mathcal{V}_{0k}$ and integrating over it is a computationally intensive problem [53]. Nonetheless, it is possible to relax the structure of $\mathcal{V}_{0k}$ and solve instead for bounds on P_{c} [53, 70, 71].

2.6.1 Upper Bound on P_{c}

The volume of a Voronoi cell is equal to the absolute value of the determinant of its lattice generating matrix [53]. Thus, the volume of $\mathcal{V}_{0k}$ is $|\det \mathbf{R}_{\mathrm{nn}k}|$. By making a simplifying assumption that $\mathcal{V}_{0k}$ is an ℓ-dimensional hypersphere with the same volume, an upper bound on the probability of successful integer ambiguity resolution can be written as [53]

$$P_{\mathrm{c,ub}} = \Pr\left\{\|\mathbf{v}_{\mathrm{n}k}\| < \rho\right\} \tag{2.31}$$

where ρ is the radius of the hypersphere defined as

$$\rho = \sqrt[\ell]{|\det\, \mathbf{R}_{\mathrm{nn}k}|/\alpha_\ell} \tag{2.32}$$

where ℓ is the dimension of vector $\mathbf{v}_{\mathrm{n}k}$ and

$$\alpha_\ell = \pi^{\frac{\ell}{2}}/\Gamma(\ell/2+1) \qquad\qquad \text{and}$$
$$\Gamma(\ell) = (\ell-1)!.$$

Since $\mathbf{v}_{\mathrm{n}k}$ is an ℓ-dimensional normal random vector, $\|\mathbf{v}_{\mathrm{n}k}\|^2$ is equal to the sum of squares of ℓ independent normally distributed random variables [53], which has a chi-squared distribution with ℓ-degrees of freedom. As a result,

$$P_{\mathrm{c,ub}} = F_{\chi^2}(\rho^2;\ell). \tag{2.33}$$

where $F_{\chi^2}(\cdot;n)$ is the cumulative distribution function of a n-degree chi-squared random variable.

2.6.2 Lower Bound on P_c

The probability of correctly resolving integer ambiguities using so-called integer bootstrapping [72] offers the sharpest known lower bound on P_c [73]. Unlike the case with ILS solvers, it is possible to compute this bootstrapping probability exactly. The bootstrapping estimator takes an approach where it rounds the float least-squares solution while taking advantage of correlation between the ambiguities into account. The bootstrapping estimator's probability of successful ambiguity resolution, which offers a lower bound on P_c, can be written as [72]

$$P_{\mathrm{c,lb}} = \prod_{i=1}^{n} \left(2\Psi\left(\frac{1}{2\sigma_{\hat{n}|I}} \right) - 1 \right) \tag{2.34}$$

where $\sigma_{\hat{n}|I}$ are conditional variances derived from $\mathbf{R}_{\mathrm{nn}k}$ [72], and

$$\Psi(x) = \int_{-\infty}^{x} \frac{1}{2\pi} \exp\left(-\frac{1}{2} y^2 \right) \mathrm{d}y. \tag{2.35}$$

For the sensitivity results presented later in Sec. 2.8, the code provided by the Ps-LAMBDA software package [74] was used to compute this lower bound.

2.7 Simulation and Test Environment

To evaluate the performance of the reconstruction technique outlined in Sec. 2.5, a Monte-Carlo-type simulation and test environment has been designed in MATLAB. The environment performs three tasks.

First, it simulates double-differenced GNSS residual carrier phase time histories $\nabla\Delta\phi_{\mathrm{r}}(t)$. Noise parameters modeling the double-differenced range error $\nabla\Delta r_{\mathrm{e}}(t)$, the double-differenced propagation- and multipath-induced effects $\nabla\Delta\epsilon_{\mathrm{p}}(t)$, and the double-differenced measurement noise $\nabla\Delta v_{\phi}(t)$ are inputs to the simulator. Structural parameters such as the measurement burst duration T_{b}, the time between consecutive bursts T_{p}, and the ambiguity factor M are also inputs. Note that although the reconstruction technique can handle variations in T_{b} and T_{p}, i.e., a non-fixed burst duration and aperiodic bursts, for the analysis performed in this section, these quantities will be assumed fixed. From these parameters, independent time histories of $\nabla\Delta\phi_{\mathrm{r}}(t)$ are generated. Note that phase-locked loop (PLL) pull-in transients need not be simulated in $\nabla\Delta\phi_{\mathrm{r}}(t)$ so long as a batch estimation technique is assumed to be used by the receiver as opposed to a PLL as will be discussed in Sec. 2.10.4.

Second, the reconstruction technique is applied to each generated $\nabla\Delta\phi_{\mathrm{r}}(t)$ to produce smoothed reconstructed double-differenced carrier phase time histories $\nabla\Delta\phi_{\mathrm{R}}(t)$.

Third, the environment evaluates the performance of the reconstruction technique by computing the empirical probability of correct integer ambiguity resolution $P_{\mathrm{c,emp}}$ as well as the analytical upper and lower bounds $P_{\mathrm{c,lb}}$ and $P_{\mathrm{c,ub}}$ discussed in Sec. 2.6. $P_{\mathrm{c,emp}}$ is computed as the ratio of the number of successful reconstruction attempts to the total number of attempts. A successful attempt occurs when all ambiguities are resolved successfully. In the limit, as the number of attempts approaches infinity, $P_{\mathrm{c,emp}} \to P_{\mathrm{c}}$.

2.7.1 Error Component Modeling

To create a high-fidelity simulator and to ensure near-optimal reconstruction of the simulated phase time histories, it is important to provide both the simulator and the reconstruction algorithm with accurate models for the phase variations caused by each error component of $\nabla\Delta\phi_{\mathrm{r}}(t)$ detailed in (2.3). Some of the error components can be realistically modeled by the following flexible model:

Let $S_\phi(f)$ be the single-sided power spectral density (PSD) of some stationary phase error process $\phi(t)$. $S_\phi(f)$ can be expressed as

$$\mathcal{S}_\phi(f) = 4\int_0^\infty \mathcal{R}_\phi(\tau)\cos(2\pi f\tau)\mathrm{d}\tau \tag{2.36}$$

where $\mathcal{R}_\phi(\tau) = \mathbb{E}[\phi(t)\phi(t+\tau)]$ is the autocorrelation function of $\phi(t)$. Let $S_\phi(f)$ be approximated by a frequency-weighted summation of five power-law parameters h_α, called h-parameters [75]:

$$\mathcal{S}_\phi(f) = \frac{\nu_0^2}{f^2} \sum_{\alpha=-2}^{2} h_\alpha f^\alpha \qquad 0 < f < f_h \tag{2.37}$$

where ν_0 is the nominal center frequency of the phase data (e.g., the GPS L1 center frequency), in Hz, and f_h is the maximum frequency at which $\mathcal{S}_\phi(f)$ is evaluated, typically corresponding to the Nyquist frequency of the sampled phase error process $\phi(t)$. Often only the h_{-2} component (corresponding to frequency random walk) and the h_0 component (corresponding to phase random walk) of the model are assumed to be nonzero. In this case, the five-parameter model in (2.37) reduces to the two-parameter (second-order Gauss-Markov) clock error model commonly invoked in Kalman filtering [61].

Two out of the four error components of $\nabla\Delta\phi_\mathrm{r}(t)$ can be accurately characterized by a PSD model of the form in (2.37): (1) double-differenced range error term $\nabla\Delta r_\mathrm{e}(t)$ whose variations are largely induced by IMU errors, and (2) the double-differenced propagation- and multipath-induced error term $\nabla\Delta\epsilon_\mathrm{p}(t)$. As discussed in Sec. 2.5.1.2, both of these error components are process noise and are characterized by the S_f and S_g parameters in the process noise covariance matrix $\mathbf{Q}$ defined in (3.17). The relationship between S_f and S_g and the two-parameter h_{-2} and h_0 model is as follows [61]:

$$S_g = 2\pi^2 h_{-2} \tag{2.38}$$

$$S_f = \frac{h_0}{2}. \tag{2.39}$$

A third error component, the double-differenced measurement noise $\nabla\Delta v_\phi(t)$, could also be characterized by a PSD model, in particular by the h_2 parameter corresponding to white phase noise, but $\nabla\Delta v_\phi(t)$ will instead be characterized by the more-familiar carrier-to-noise ratio C/N_0. Under this characterization, the measurement noise variance $\sigma^2_{\phi k}$ (defined after (3.12)) is computed from its full nonlinear relationship to $(C/N_0)_k$, assuming a standard arctangent-type phase detector, and used to simulate the discrete-time measurement noise v_k of (3.12). The final term, the phase ambiguity term $\nabla\Delta\eta(t)$, need not be modeled, as ambiguities are introduced deterministically via an "ambiguity-free" simulation of $\nabla\Delta\phi_{\mathrm{r}}(t)$ which is then aliased to between 0 and $\frac{1}{M}$ cycles.

2.7.2 Inertial Aiding

As discussed in Sec. 2.4, an inertial measurement unit (IMU) can model the rover receiver's changing position, enabling it to more-accurately predict its line-of-sight range to each satellite. This modeling substantially eliminates receiver-motion-induced variations from $r_{\mathrm{e}}(t)$, and, consequently, from $\nabla\Delta\phi_{\mathrm{r}}(t)$. It is for this reason that while the reconstruction technique can work without inertial aiding, it works much better when inertial measurements are available.

2.7.2.1 Characterization of Inertial Errors

Despite its advantages, inertially-aided motion prediction is imperfect. Noise in the IMU measurements will leave residual variations in $r_{\mathrm{e}}(t)$ which enter into $\nabla\Delta\phi_{\mathrm{r}}(t)$. These variations must be accurately characterized to enable optimal reconstruction. The two-parameter PSD model, discussed previously, can be used to characterize these variations. Table 2.1 lists h-parameter values that characterize the undifferenced range-error variations resulting from use of three different-quality IMUs to predict the receiver's motion: (1) a low-end "consumer-grade" IMU found in consumer-electronic devices, (2) a high-end "consumer-grade" IMU found in commercial equipment, and (3) a "tactical-grade" IMU found in military equipment.

Table 2.1: h-parameter values characterizing the noise statistics of three inertial measurement units

Device	h_{-2} (cycles^2-Hz)	h_0 (cycles^2/Hz)	Grade
Analog Dev. ADIS16360	5×10^{-24}	3×10^{-27}	Consumer
XSENS MTi	5×10^{-25}	3×10^{-28}	Consumer
Honeywell HG1900	5×10^{-26}	3×10^{-29}	Tactical

These h-parameter values were determined as follows: First, white noise and bias instability values commonly used to characterize acceleration and angular velocity measurement noise were taken from the datasheet of each IMU. Second, these values were used to simulate IMU measurement errors and, from these, IMU-specific 3-dimensional position error trajectories were generated [76]. Third, the PSD of the variations along a randomly chosen dimension was computed and a weighted least-squares solution was used to determine h-parameter-values best characterizing each PSD, as per (2.37). The final values listed in Table 2.1 represent average values from 20 Monte-Carlo-type simulations. While it is possible to compute the h-parameter equivalents of the white noise and bias instability parameters in isolation, it becomes much more difficult to accurately compute these parameters when the noise sources are coupled together, such as is the case in an inertial navigation system as described here.

2.7.2.2 Estimation of Inertial Biases

The foregoing two-parameter model for errors in $\nabla\Delta\phi_{\mathrm{r}}(t)$ due to imperfect inertial aiding does not account for biases in the IMU's accelerometer and rate sensor measurements. Such biases could be accommodated by augmenting the real-valued state with a phase-acceleration component and, consequently, the two-parameter error model with an h_{-4} parameter. However, this turns out to be unnecessary so long as these inertial biases and the receiver orientation are periodically estimated and compensated for. Assuming that a receiver starts with a pseudorange-based initial position and an accelerometer-and-magnetometer-provided orientation, then acceleration, angular velocity, and magnetometer measurements can be integrated in an inertial navigation system (INS) [76] that approximates the receiver's change in position and orientation over an extended period of many bursts. After each extended period, e.g., roughly 20 seconds for a consumer-grade IMU, the INS-derived position must be augmented with GNSS code-phase and recently-reconstructed ambiguity-free GNSS carrier-phase measurements in a tightly-coupled INS/GNSS filter that estimates the inertial biases and receiver orientation as part of its state [32, 77]. These recent bias and orientation estimates will enable the INS to more-accurately approximate the receiver's change in position and orientation over the next extended period, allowing the reconstruction technique to accurately predict the receiver-motion-induced phase variations. This technique works so long as the inertial biases remain approximately constant over the duration of each extended period. Section 2.9 provides a demonstration of the reconstruction technique on real data where inertial biases and receiver orientation were periodically estimated in this way.

2.8 Sensitivity Analysis

This section discusses the sensitivity of the reconstruction technique to signal structure parameters such as the burst period T_{p} and the $\frac{1}{M}$ ambiguity factor and to signal error parameters such as the carrier-to-noise ratio and the underlying IMU quality. Sensitivity is measured by computing empirical estimates and analytical bounds on the probability of correct integer ambiguity resolution P_{c} as a function of these parameters. The purpose of the sensitivity analysis is to discover parameter bounds beyond which the reconstruction technique will perform poorly. As it is unwieldy to test all possible combinations of parameters, testing is performed around a set of nominal parameters that model a typical low-power mobile receiver setup. In particular, during each test, sensitivity is analyzed as a function of the burst period T_{p} and one other parameter, namely IMU quality, the ambiguity factor $\frac{1}{M}$, or the carrier-to-noise ratio C/N_0. During each test, the strategy will be to:

1. Fix the burst duration T_{b} to 0.05 seconds and the time duration over which reconstruction will be performed to 250 seconds.

2. Vary the time between bursts T_{p} for each test, along with one of either IMU quality, M, and C/N_0.

3. Fix $M = 1$, $C/N_0 = 50$ dB-Hz, and the IMU quality to that of a low-quality consumer-grade IMU when not being varied.

This will result in three sensitivity scenarios, each of which is explored in the next three subsections.

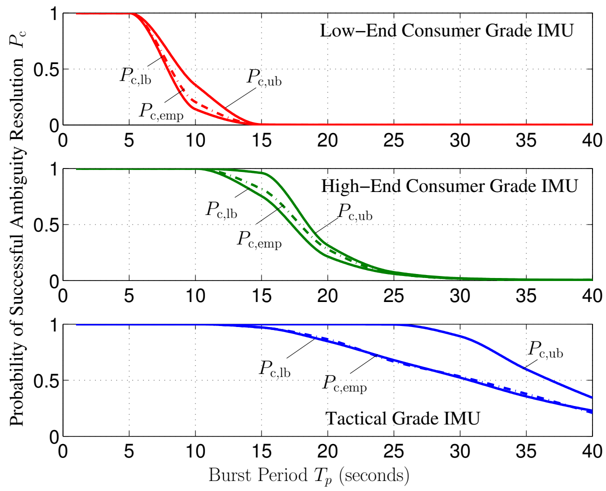

Figure 2.4: Probability of successful ambiguity resolution P_{c} as a function of the burst period T_{p} and of IMU quality. The dashed traces denote the empirical estimate of P_{c}, $P_{\mathrm{c,emp}}$, obtained via Monte-Carlo simulation. The solid traces denote the analytically computed upper and lower bounds $P_{\mathrm{c,lb}}$ and $P_{\mathrm{c,ub}}$.

2.8.1 Sensitivity to IMU Quality

This section illustrates the sensitivity of the reconstruction technique to the underlying IMU quality, modeled by the h_0 and h_{-2} power-law parameter values listed in Table 2.1, and to the burst period T_{p}. During sensitivity testing, the IMU quality and the burst period were varied while the other important parameters were held constant at the values discussed earlier.

Fig. 2.4 illustrates the sensitivity results. The empirical probability of successful ambiguity resolution $P_{\mathrm{c,emp}}$ was computed via Monte-Carlo simulation and is represented by the dashed trace. The lower and upper bounds $P_{\mathrm{c,lb}}$ and $P_{\mathrm{c,ub}}$ were computed analytically (see section 2.6) and are represented by the solid traces. The waterfall structure of each trace indicates a breakdown point in successful ambiguity resolution. Each subplot represents a different underlying IMU quality. It is evident that the higher the IMU quality, the larger the burst period T_{p} that the

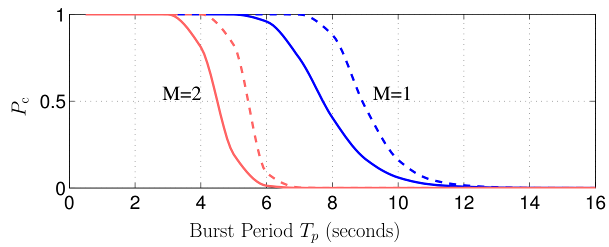

Figure 2.5: Probability of successful ambiguity resolution P_{c} as a function of the burst period T_{p} and the ambiguity factor M. The dashed traces denote an upper bound on P_{c}, $P_{\mathrm{c,ub}}$, while the solid traces denote a lower bound, $P_{\mathrm{c,lb}}$.

reconstruction technique can sustain before a breakdown occurs. A higher quality IMU allows the reconstruction technique to more accurately predict the underlying phase trajectory between bursts, making it easier to resolve the phase ambiguity at the beginning of each burst.

2.8.2 Sensitivity to the Ambiguity Factor

Fig. 2.5 plots $P_{\mathrm{c,lb}}$ and $P_{\mathrm{c,ub}}$ as a function of T_{p} for two different values of the ambiguity factor M. (For visual clarity, empirical results, which always lie close to $P_{\mathrm{c,ub}}$, were not plotted.) As shown, a lower M value allows for a larger burst period T_{p} before a breakdown in P_{c} occurs. This is as might be expected: all else equal, integer-cycle ambiguities are easier to resolve than fractional-cycle ambiguities. This implies that a GNSS receiver with *a priori* knowledge of the binary navigation data symbols and an approximation of its position and time (to within a fraction of a data symbol interval) (in which case $M = 1$) has the ability to be more power efficient than a receiver with no such knowledge ($M = 2$) by extending its burst period while maintaining the same probability of successful ambiguity resolution.

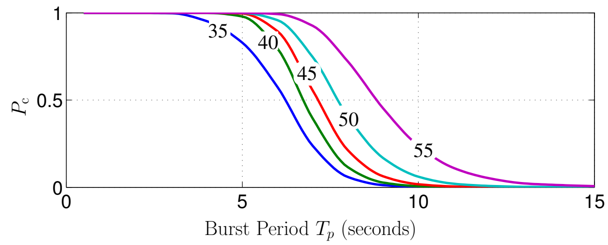

Figure 2.6: Lower bounds on the probability of successful channel reconstruction as a function of the burst period T_p and the carrier-to-noise ratio C/N_0 (in dB-Hz).

2.8.3 Sensitivity to the Carrier-to-noise Ratio

Fig. 2.6 plots lower bounds on P_c as a function of the burst period for five different carrier-to-noise ratios. Note that for visual clarity only the lower bounds were plotted. As illustrated, a higher C/N_0 tolerates a longer burst period before a breakdown in P_c occurs. This is because for lower C/N_0 values the measurement noise variations v_k imparted by the receiver's front end become a larger share of the overall variations within y_k [see (3.12)]. This makes it difficult for the reconstruction technique to separate these variations from the variations due to the real- and integer-valued state components $\mathbf{x}_k$ and $\mathbf{n}_k$, leading to a decrease in the probability of correct ambiguity resolution.

2.9 Demonstration of a CDGNSS Solution on Reconstructed Data

This section provides a demonstration of the reconstruction technique applied to real data collected by a reference and rover GNSS receiver. Each receiver was running a version of the GRID software [78–80] and is capable of capturing GNSS signal code- and carrier-phase data. Additionally, the rover contained an Xsens MTi IMU capable of providing linear acceleration measurements and attitude estimates derived from an internal filter.

2.9.1 Data Collection, Modification, and Processing

The demonstration was carried out as follows. First, GNSS signal code- and carrier-phase data were collected simultaneously and continuously by both receivers while IMU-provided acceleration measurements and attitude estimates were additionally collected by the rover. Two minutes of data were collected. During this time the rover receiver was moved about while the reference receiver remained stationary. The rover's trajectory was that of a pedestrian moving at a walking-pace holding the receiver at an approximately fixed pitch and roll angle, but allowing changes in yaw. Second, the data collected by the rover receiver were digitally modified in two ways to simulate collection by a power-constrained receiver: (1) discrete measurement intervals were selected from the continuously-recorded GNSS code- and carrier-phase data and (2) the carrier-phase data were aliased to between 0 and 1 cycle. Third, the intermittent carrier-phase time histories from the two receivers were differenced to form 7 double-differenced carrier-phase time histories from 8 GNSS satellite signals present in the recorded data. Fourth, biases in the IMU acceleration measurements were estimated once every 60 seconds via an INS/GNSS filtering technique similar to that described in Sec. 2.7.2.2. Fifth, the bias estimates, acceleration measurements, and IMU-derived attitude estimates were incorporated into an INS to approximate the receiver trajectory and remove the motion-induced variations from each double-differenced carrier-phase time history, forming double-differenced residual carrier-phase time histories. Sixth, the reconstruction technique was applied to each double-differenced residual carrier-phase time history. Finally, the reconstructed time histories (along with the intermittent code-phase measurements) were passed off to a standard CDGNSS positioning al-

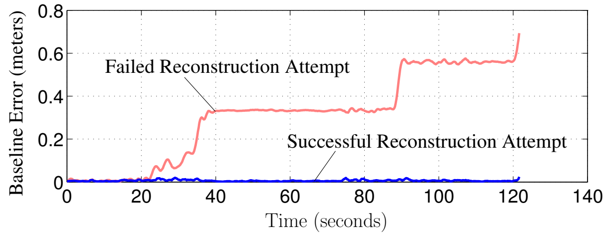

Figure 2.7: Error in the positioning solution provided by the CDGNSS algorithm whose inputs are phase trajectories from two different reconstruction outcomes: (1) a successful attempt (lower blue trace) defined when all phase ambiguities were resolved correctly for all 7 of the reconstructed phase time histories involved in the positioning solution and (2) a failed attempt (upper red trace) defined when one or more phase ambiguities were resolved incorrectly for one or more of the reconstructed phase time histories.

gorithm which computed a centimeter-accurate positioning solution for the rover receiver.

2.9.2 Results

Fig. 2.7 illustrates the accuracy of the CDGNSS-based positioning solution under two circumstances: (1) a scenario in which all phase ambiguities from the 7 reconstructed time histories were resolved correctly, and (2) a scenario in which one or more phase ambiguities were resolved incorrectly. In the first scenario, carrier-phase measurements were provided to the reconstruction algorithm with a burst length of $T_{\mathrm{b}} = 0.05$ seconds and a burst period of $T_{\mathrm{p}} = 1$ seconds, which corresponds to a 5% duty cycle. For the second scenario, $T_{\mathrm{b}} = 0.05$ seconds and $T_{\mathrm{p}} = 2$ seconds, corresponding to a 2.5% duty cycle. The time duration of the dataset for each scenario was approximately 120 seconds. In both scenarios, the error, in meters, from the true position is computed and plotted as a function of time. The ground truth trajectory is obtained by separately computing a CDGNSS solution using the unmodified, ambiguity-free, continuous phase time histories originally captured by the receivers. As the lower trace illustrates, when the reconstruction algorithm resolves the phase ambiguities correctly, the positioning error is very small (less than 1.5 cm). The small error is primarily due to the inability of the reconstruction algorithm to perfectly reconstruct the variations in the residual carrier phase between measurement bursts. In contrast, as the upper trace illustrates, incorrectly resolved ambiguities lead to significant positioning errors well in excess of the accuracy potential of the CDGNSS algorithm. Large jumps in the positioning error denote an incorrectly resolved phase ambiguity at that time index.

In this demonstration, the availability of the ground truth trajectory enables the generation of a simple metric, i.e., baseline error, to indicate when reconstruction has failed. However, a system in the field will not have a ground truth trajectory with which the baseline error can be generated. In these cases, the system can compute the upper and lower bounds on the probability of successful reconstruction, as introduced in Sec. 2.6, and use one or both of these as an indicator as to when reconstruction may have failed, e.g., when $P_{\mathrm{c,lb}}$ is not above a predetermined threshold for each double-differenced reconstructed phase time history, the resulting CDGNSS solution can be presumed inaccurate.

It should be noted that while the results shown here are promising, these results reveal the performance of the reconstruction technique on only one set of collected data. For a more in-depth and direct analysis of the technique's performance, see Sec. 2.8, where reconstruction was performed on hundreds of sets of simulated data and compared against analytical performance bounds.

Table 2.2: GNSS Chip Power Consumption

Mfr.	Chip	Measurements Provided	Power (mW)
Broadcom	BCM4751	duty-cycled code phase	13
u-blox	NEO-6P	cont. code & carrier phase	117

2.10 Power Consumption Analysis

This section provides an analysis of the power consumption of the duty-cycled measurement framework enabled by the carrier-phase reconstruction technique as compared to a framework requiring the continuous tracking of GNSS signal carrier phase.

2.10.1 Low-Power GNSS Chips

Table 2.2 lists two GNSS chips and their average power consumption. The Broadcom chip, used in many mobile devices, computes a receiver's position using only the tracked code-phase of each GNSS signal. It achieves an impressively low power draw of 13 mW by aggressively duty cycling its code-phase measurements [23]. Unlike carrier-phase measurements, code-phase measurements do not suffer from ambiguity problems when duty-cycled. Code-phase measurements, however, can only be used to compute a pseudorange-based position solution, which is much less accurate than a carrier-phase-based CDGNSS solution. The other two chips provide both code- and carrier-phase measurement outputs. To provide ambiguity-free carrier-phase measurements, these chips continuously track each GNSS signal, drastically increasing their power consumption compared to the duty-cycling Broadcom chip. The NEO-7M, a variant of the NEO-6P, has a low-power duty-cycled mode with a power draw of 14 mW [43], similar to that of the Broadcom chip. The

NEO-7M, however, does not provide access its carrier-phase measurements. This dissertation's author conjectures that both u-blox and Broadcom believe it is fruitless to provide carrier-phase data fraught with ambiguities and so do not provide access to these measurements in chips with duty-cycled tracking modes.

It is important to note that unlike code and carrier phase, whose measurements are duty-cycled in this low-power framework, acceleration and angular velocity must be continuously measured by an IMU such that they can be used in predicting receiver motion between phase measurement bursts (see Sec. 2.7.2). Fortunately, there exist low-power chip-scale IMUs which consume power on the order of 10-20 mW [81], much less than the state-of-the-art u-blox chips that output continuous code and carrier phase measurements.

2.10.2 Power Consumption of the Reconstruction Algorithm

The reconstruction technique outlined in this chapter relaxes the continuous tracking requirement for GNSS chips that provide carrier-phase measurements. Although duty-cycled measurements will contain phase ambiguities, the reconstruction technique can be applied to these measurements, enabling, under favorable circumstances, an ambiguity-free continuous time phase history to be accurately reconstructed.

The minimum power consumed by a receiver duty cycling its carrier-phase measurements can be described as a percentage of the power consumed by a receiver continuously tracking the carrier phase:

$$\text{Power Consumption } (\%) = \frac{T_{\mathrm{b}}}{T_{\mathrm{p}}} \times 100. \tag{2.40}$$

This power consumption metric is a minimum as it considers only the power that will be saved by measurement duty-cycling. It ignores the overhead imposed by

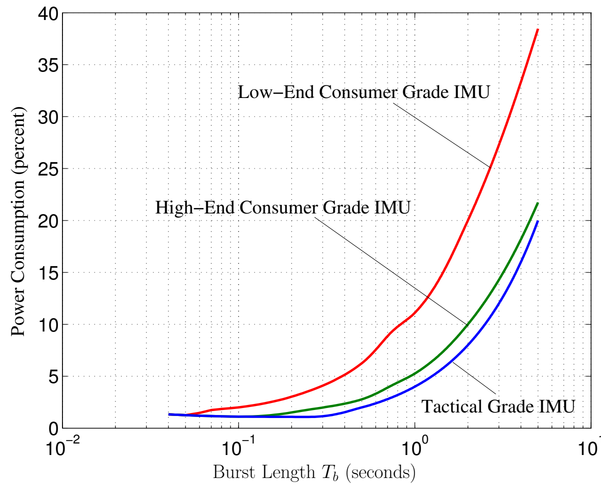

Figure 2.8: Minimum achievable relative power consumption of a duty-cycled measurement and phase reconstruction framework as compared to a continuous measurement framework as function of the burst length T_b.

the reconstruction algorithm and the overhead involved in turning on and off the receiver components associated with sampling and digitizing the signal. This will be discussed later.

When evaluating the power consumption using (2.40), it is logical to check that the chosen combination of T_b and T_p will result in a successful reconstruction. One way to do this is to look at the lower bound of the probability of successful ambiguity resolution $P_\mathrm{c,lb}$ and determine if it is above a certain threshold, e.g., 99.99%. Obviously, as $\frac{T_\mathrm{b}}{T_\mathrm{p}} \to 1$, $P_\mathrm{c,lb} \to 1$, but the power consumption as denoted by (2.40) will also approach 100%, saving little power. Accordingly, there exists a tradeoff between keeping $P_\mathrm{c,lb}$ close to 1 and minimizing the power consumption.

Fig. 2.8 provides an empirical analysis of the minimum achievable power consumption as a function of the burst length T_b for performing reconstruction on a simulated double-differenced residual GNSS signal. The signal was simulated with a single-sided PSD defined by (2.37) with the h_{-2} and h_0 power-law parameters varied according to the values in Table 2.1, representing the usage of a low-end consumer-, high-end consumer-, and tactical-grade IMU. Additionally white phase noise was added to the signal to simulate front-end noise representative of a receiver $C/N_0 = 50$ dB-Hz. The simulated dataset duration was 250 seconds. For simplicity, it was assumed that the contribution to $\nabla\Delta\phi_{\mathrm{r}}(t)$ by unmodeled propagation and multipath effects was small in comparison to the other noise sources, and as such, the h-parameters characterizing the PSD of this noise source were set to 0.

In computing the power consumption values in Fig. 2.8, for each T_{b} the largest value of T_{p} was chosen such that $P_{\mathrm{c,lb}}$ remained above .9999. The power consumption was then computed using (2.40) and plotted. From the figure, one can make two interesting observations. First, the minimal power consumption is attained when the burst length is very small. This implies that, to save power, it is beneficial for a GNSS receiver making duty-cycled phase measurements to use relatively short burst lengths and short burst periods rather than long burst lengths and long burst periods. Second, at shorter burst lengths (and burst periods), the quality of the underlying IMU has a smaller impact on reducing power consumption. This implies that a high-quality IMU can be forgone in favor of a lower-quality IMU as long as the burst length and burst period are reduced enough to achieve the desired power consumption. This is an important result as many mobile handheld devices come with consumer-grade IMUs (or separate consumer-grade accelerometers and rate sensors).

2.10.3 Power Consumption Overhead

Although measurement duty-cycling enables a large reduction in power consumption at the rover receiver, it would be negligent to assume that the added computational complexity required by the reconstruction algorithm to reconstruct a continuous phase-time history from the duty-cycled measurements does not consume any power. Much computational complexity is added by the integer least-squares ambiguity resolution algorithm, and this complexity increases exponentially with the number of integer ambiguities to resolve [54]. Fortunately, unlike carrier-phase measurement, carrier-phase reconstruction need not be executed at the rover receiver – the discrete phase measurements can be relayed to the cloud for reconstruction. Furthermore, because the CDGNSS algorithm requires a double-differencing of carrier-phase measurements from the rover and a reference station, the rover would in any case be required to offload its measurements to the network, since receiving reference station measurements from the network and computing the CDGNSS solution locally would likely consume more power than relaying local phase measurements to the network.

The additional power required to transmit data in an LTE network versus receiving it is about 400 mW per 1 Mbps [82]. The average rate at which the rover must send duty-cycled phase measurements to the cloud is $f_\mathrm{s} \cdot \frac{T_\mathrm{b}}{T_\mathrm{p}}$ measurements per second, which, for aggressive duty cycling (e.g., $\frac{T_\mathrm{b}}{T_\mathrm{p}} = \frac{1}{10}$) and a modest sampling rate (e.g., $f_\mathrm{s} = 50$ Hz), would result in an average code- and carrier-phase measurement rate of 5 samples per second per signal tracked. Given 10 signals tracked and 32 bits allocated per sample, the average transmission data rate is about 1.6 kbps, or approximately 0.6 mW of added power to transmit the carrier phase data rather than receive it. Although this number does not account for the cost of transmitting the code-phase and IMU measurements, the total rover power consumption for a cloud-based CDGNSS solution will likely be far below the power consumption needed to perform a local CDGNSS solution. Thus, under the current framework, the rover will relay a batch of code- and carrier-phase measurements along with IMU measurements to the network for processing. The network will perform phase differencing, IMU bias correction, reconstruction, and CDGNSS processing and then relay back to the rover the latter's precise position time history over the batch interval.

In addition to the overhead involved in transmitting data over the network, the power consumption model in (2.40) also ignores the power overhead associated with switching on and off the receiver components involved in sampling and digitizing the GNSS signals. Such overhead is inversely proportional to T_p; as T_p is decreased, there will come a point when the increase in power consumption due to this overhead will outweigh the additional reduction in power consumption from measurement duty-cycling. This "break-even" point places a lower bound on T_p (and its associated T_b), below which the power consumption will no longer decrease. For the power consumption analysis described in Sec. 2.10.2 whose results are displayed in Fig. 2.8, T_p is always larger than 1 second. Such values of T_p are assumed to be well above this break-even point. As such, the power overhead due to switching is assumed to be negligible and is not modeled by (2.40).

2.10.4 Avoiding Phase-Locked Loop Transients using Batch Estimation

If the rover receiver's phase-locked loop (PLL) re-synchronizes its local carrier replica with the incoming carrier phase at the beginning of each measurement burst, then this will result in short phase transients during re-synchronization [83]. These transients are manageable so long as they settle prior to the end of the measurement burst, i.e., the convergence time is less than T_b. However, only the phase measurements taken after this settling period can be used during reconstruction. Rather than forgo the information contained in these transients, which could benefit reconstruction, a different methodology avoids them altogether. Instead of attempting to track the incoming carrier-phase using a traditional PLL, the rover receiver can generate a model line of sight trajectory to each GNSS satellite tracked and employ batch estimation on raw correlation outputs to measure carrier phase, code phase, and Doppler with no phase pull-in transient. This model-trajectory methodology is standard in so-called vector tracking, where traditional tracking loops are replaced by a navigation filter that provides prior knowledge of receiver position and velocity to the local replica generators [62, 84]. The only requirement is that the model-trajectory be accurate enough that the difference between the received carrier phase and the carrier-phase predicted by the model-trajectory does not drift by more than $\frac{1}{2}$ cycle during the sampling interval $\frac{1}{f_s}$.

2.11 Conclusions

A technique for reconstructing a continuous carrier-phase time history from intermittent GNSS carrier-phase measurements has been developed. The technique combines an integer least-squares method for estimating the phase ambiguity that arises at the beginning of each measurement burst with a Kalman filter and smoother that correct for these ambiguities and "stitch" the bursts together.

A Monte-Carlo-type simulation and test environment has been built in MATLAB to simulate the intermittent GNSS phase measurements, implement the phase reconstruction technique, and analyze the sensitivity of the technique to determine the parameter space within which successful reconstruction is possible. Theoretical bounds predicting the probability of successful reconstruction were compared to empirical results from the Monte-Carlo simulations.

Simulation results indicate that successful carrier-phase reconstruction is strongly dependent on the burst period, the carrier-to-noise ratio, the ambiguity factor, and the quality of the underlying inertial measurement unit employed by the receiver. A demonstration on real data shows that the reconstruction technique can successfully reconstruct carrier phase measurements made at a 5% duty cycle by a GNSS receiver containing a consumer-grade IMU and receiving GNSS signals with a carrier-to-noise ratio of 50 dB-Hz. The reconstruction technique assumes the use of special batch tracking techniques to avoid PLL transients at the start of each burst. Furthermore, an analytical power analysis indicates that the reconstruction technique can permit potential power savings in excess of 95% for a receiver duty-cycling its carrier phase measurements when compared against a receiver continuously tracking the incoming carrier phase. These results suggest that the reconstruction technique could act as an enabler for high-precision positioning in energy-limited mobile devices.

Chapter 3

Proof of Concept and Techniques to Address the Challenges of Carrier-Phase Positioning on Low-Cost Mobile Platforms

This chapter demonstrates for the first time that centimeter-accurate positioning is possible based on data sampled from a smartphone-quality Global Navigation Satellite System (GNSS) antenna. An empirical analysis of data collected from a smartphone-grade GNSS antenna reveals the antenna to be the primary impediment to fast and reliable resolution of the integer ambiguities which arise when solving for a centimeter-accurate carrier-phase differential GNSS (CDGNSS) position. The antenna's poor multipath suppression and irregular gain pattern result in large time-correlated phase errors which significantly increase the time to integer ambiguity resolution (TAR) as compared to even a low-quality stand-alone patch antenna.

To address this problem, this chapter investigates the presents and analyzes the effectiveness of multipath-decorrelating antenna motion for reducing TAR in receivers employing low-cost single-frequency antennas to obtain a CDGNSS position. This chapter demonstrates that the time to ambiguity resolution—and to a centimeter-accurate fix—can be significantly reduced through gentle wavelength-scale random antenna motion. Such motion acts to decrease the correlation time of the multipath-induced phase errors. *A priori* knowledge of the motion profile is shown to further reduce TAR, with the reduction more pronounced as the initialization scenario is more challenging.

3.1 Introduction

GNSS technology is now ubiquitous in smartphones and tablets, yet the underlying positioning accuracy of consumer-grade GNSS receivers has stagnated over the past decade. The latest clock, orbit, and atmospheric models have improved receiver ranging accuracy to a meter or so [9], leaving receiver-dependent multipath- and front-end-noise-induced variations as the dominant error sources in current consumer devices [85]. Under good multipath conditions, 2-to-3-meter-accurate positioning is typical; under adverse multipath, accuracy degrades to 10 meters or worse.

Yet outside the mainstream of consumer GNSS receivers, centimeter-accurate GNSS positioning is routine. This exquisite accuracy, common in geodesy, agriculture, and surveying, results from replacing standard code-phase positioning techniques with carrier-phase differential GNSS (CDGNSS) techniques [17, 45]. Carrier phase techniques offer far more accurate positioning due to the much smaller wavelength of the GNSS signal's carrier, approximately 20 centimeters, as compared its spreading code, whose chip interval spans approximately 300 meters.

Currently, the primary impediment to performing centimeter-accurate CDGNSS positioning on smartphones and other consumer handheld devices lies not in the commodity GNSS chips, which actually outperform survey-grade chips in some respects [86], but in the low-cost (e.g., a few cents to a few dollars), low-quality GNSS antennas, whose chief failing is poor multipath suppression. Multipath, caused by direct signals reflecting off the ground and nearby objects, induces centimeter-level phase measurement errors, which, for static receivers, have correlation times in the hundreds of seconds [87]. The time correlation of these errors, coupled with their relatively large magnitude, significantly increases the initialization period of GNSS receivers using these antennas to achieve a centimeter-accurate CDGNSS positioning solution [2, 88, 89]. This is because, given a fixed measurement duration, a longer measurement error correlation time results in less information being provided to the CDGNSS estimator as it attempts to resolve the integer ambiguities inherent in CDGNSS processing, making their successful estimation less likely. Consequently, any strategy that reduces the measurement error correlation time—all else equal—leads to an increased ambiguity resolution (AR) success rate and thus a decreased initialization time, otherwise known as time to ambiguity resolution (TAR).

Prior work on mitigating the effect of time-correlated phase measurement errors in CDGNSS processing has focused not on decreasing the correlation time of the measurement errors but on appropriately modeling such correlation within the CDGNSS estimator, which leads to more accurate validation of integer ambiguity estimates but does not significantly reduce—and in some cases increases—TAR [90–93].

This chapter proposes gentle wavelength-scale random antenna motion as an effective strategy to reduce the correlation time of multipath-induced carrier phase errors, thus reducing TAR. Insofar as this dissertation's author is aware, no prior work has advocated random antenna motion as a means to expedite CDGNSS ambiguity resolution, likely because, as this chapter will show, antenna motion is beneficial—and practical—primarily for CDGNSS with small low-cost single-frequency antennas, which has been the subject of only recent study [2]. Single-frequency antennas are of primary focus because multi-frequency antennas—while offering increased AR performance that comes with more signals—will for many years remain too expensive (e.g, hundreds of dollars too expensive) for mass market products.

Although it may seem counterintuitive that random antenna motion would lead to reduced TAR, this chapter will show both in simulation and empirically that for low-quality antennas, which experience relatively large phase measurement errors, the reduction in measurement error correlation time due to motion more than compensates for the increased dynamics uncertainty within a CDGNSS estimator. Conversely, it will be shown that this is not the case for high-quality antennas. Moreover, it will be shown that TAR is further reduced with improved *a priori* knowledge of the antenna motion profile. In the limit of perfect motion profile knowledge, this chapter's technique becomes similar to the synthetic aperture technique of [94], the difference being that [94] uses the perfect motion profile to coherently process the low-level complex GNSS correlation products, whereas this chapter takes the slightly less optimal but simpler approach of operating on the usual carrier phase observables typically ingested by CDGNSS estimators.

3.2 Test Architecture

This section describes the test architecture used to (1) collect data from a smartphone-grade antenna and higher-quality antennas, (2) process these data through a software-defined GNSS receiver, and (3) compute a CDGNSS solution on the basis of the carrier phase measurements output by the GNSS receiver.

Fig. 3.1 illustrates the test architecture as configured for an in situ study of a smartphone-grade GNSS antenna. The architecture has been designed such that the antenna is left undisturbed within the phone; data are collected by tapping off

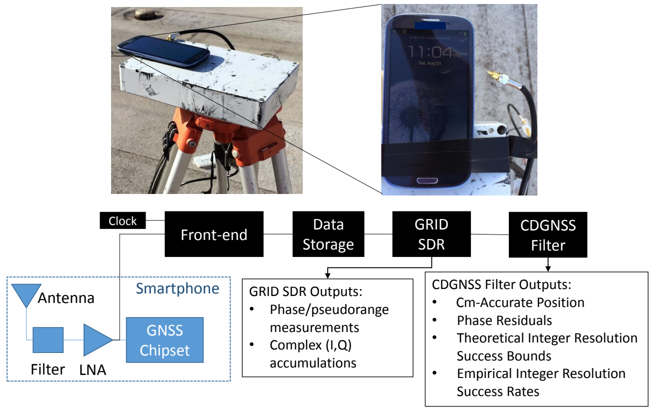

Figure 3.1: Test architecture designed for an in situ study of a smartphone-grade GNSS antenna. The analog GNSS signal is tapped off after the phone's internal bandpass filter and low-noise amplifier and is directed to a dedicated RF front-end for downconversion and digitization. Data are stored to file for subsequent post-processing by a software GNSS receiver and CDGNSS filter.

the analog signal immediately after the phone's internal bandpass filter and low-noise amplifier. This analog signal is directed to an external radio frequency (RF) front-end and GNSS receiver. Use of an external receiver permits well-defined GNSS signal processing unencumbered by the limitations of the phone's internal chipset and clock.

The clock attached to the external front-end was an oven-controlled crystal oscillator (OCXO), which has much greater stability than the low-cost oscillators used to drive GNSS signal sampling within smartphones. However, it was found that reliable cycle-slip-free GNSS carrier tracking only required a 40-ms coherent integration (pre-detection) interval, which is within the coherence time of a low-cost temperature-compensated crystal oscillator (TCXO) at the GPS L1 frequency [41].

Although only a single model of smartphone was tested using this architecture—a popular mass-market phone—the results are assumed representative of all smartphones from the same manufacturer.

Using this architecture, many hours of raw high-rate (∼6 MHz) digitized intermediate frequency samples were collected and stored to disk for post processing. Also stored to disk were high-rate data from a survey-grade antenna, which served as the reference antenna for CDGNSS processing. An in-house software-defined GNSS receiver, known as GRID [78–80], was used to generate, from these samples, high-quality carrier phase measurements. GRID is a flexible receiver that can be easily adapted to maintain carrier lock despite severe fading. Complex baseband accumulations output from GRID allowed detailed analysis of the signal and tracking loop behavior to ensure that no cycle slips occurred. The generated carrier phase measurements were subsequently passed to a CDGNSS filter, a model for which is described in the next section.

3.3 Antenna Performance Analysis

This section describes four antennas from which data were captured and processed using the test architecture and CDGNSS filter described previously. It also quantifies the characteristics that make low-quality smartphone-grade antennas poorly suited to CDGNSS.

Table 3.1 describes a range of antenna grades of decreasing quality, noting properties relevant to CDGNSS. The loss numbers in the rightmost column represent the average loss in gain relative to a survey-grade antenna, where the average is

Table 3.1: Antenna Properties

Antenna Class	**Axial Ratio**	**Polarization**	**Relative Loss**
Survey-Grade [95]	1 dB	Circular	0 dB
High-quality Patch [96]	2 dB	Circular	0 - 0.5 dB
Low-quality Patch [97]	3 dB	Circular	0.6 dB
Smartphone-Grade	10+ dB	Linear	11 dB

Table 3.2: Antennas Under Test

Survey-Grade	**High-Quality Patch**	**Low-Quality Patch**	**Smartphone-Grade**
		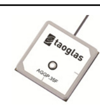	

taken over elevation angles above 15 degrees. Table 3.2 shows four antennas, one of each grade, from which many hours of data have been collected using the test architecture. Survey-grade antennas, whose properties are described in the first row of Table 3.1, have a uniform quasi-hemispherical gain pattern, right-hand circular polarization, a stable phase center, and a low axial ratio. These are all desirable properties for CDGNSS. Unfortunately, these properties inhere in the antennas' large size; the laws of physics dictate that smaller antennas will typically be worse in each property. Also listed in Table 3.1 are properties for three other antenna grades. The second and third rows list properties for high- and low-quality patch antennas. These antennas have similar properties to a survey-grade antenna and lose, on average, less than 0.5 dB and 1 dB respectively in sensitivity as compared to the survey-grade antenna [96, 97].

The last row of Table 3.1 lists the properties for a smartphone-grade antenna. As

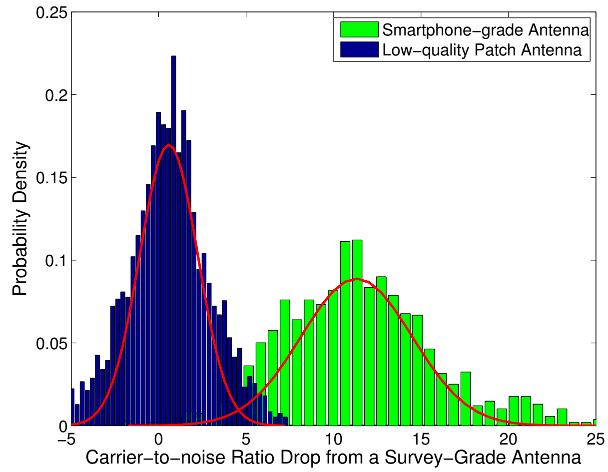

Figure 3.2: Normalized histograms displaying the drop in carrier-to-noise ratio between a survey-grade antenna and a smartphone-grade (right) and low-quality patch (left) antenna. Each histogram was generated from 2 hours of data and 9 tracked satellites ranging in elevation from 15 to 90 degrees. The antennas remained stationary. The red traces represent Gaussian distribution models fit to each histogram.

shown subsequently, this antenna loses between 5 and 15 dB in sensitivity as compared to the survey-grade antenna. Such a loss makes it difficult to retain lock on GNSS signals. In addition, this antenna's linear polarization leads to extremely poor multipath suppression.

3.3.1 Antenna Gain Analysis

Fig. 3.2 quantifies one of the obvious drawbacks of a smartphone-grade antenna, namely, its low gain. The rightmost histogram, in green, shows that the decrease in carrier to noise ratio as compared to a survey-grade antenna is on average 11 dB, such that the smartphone-grade antenna only captures approximately 8% of the signal power as compared its survey-grade counterpart. For comparison, shown on the left, in blue, is a histogram of the decrease in carrier-to-noise ratio for the

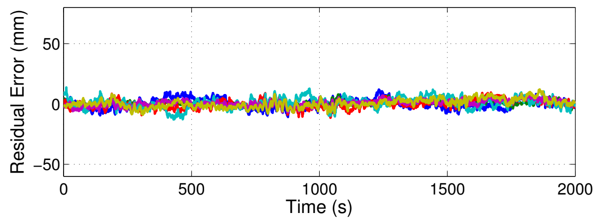

Figure 3.3: Time histories of double-differenced phase residuals for a 2000-second batch of data captured from a survey-grade antenna. Each trace represents a residual for a different satellite pair. The ensemble average standard deviation of the residuals is 3.4 millimeters.

low-quality patch antenna. This antenna only suffers about a 0.6 dB drop in power on average relative to the survey-grade antenna. Each histogram was generated from 2 hours of data with 9 tracked satellites ranging in elevation from 15 to 90 degrees. The antennas remained stationary. The variation in signal power around the means is due to the multipath-induced power variations in the signal as well as to the different gain patterns between each antenna and the survey-grade antenna.

3.3.2 Phase Residual Analysis

Shown in Figs. 3.3, 3.4, and 3.5 are 2000-second segments of double-differenced phase residual time histories for data collected from a survey-grade, a low-quality patch, and a smartphone-grade antenna, respectively. To produce these residuals, the antenna position was locked to its estimated value within the CDGNSS filter. The residuals represent departures of the carrier phase measurements from perfect alignment at the average phase center of the antenna. Each different colored trace corresponds to a different satellite pair. While the data segments were not captured at the same time of day, they were captured at the same location, and thus the

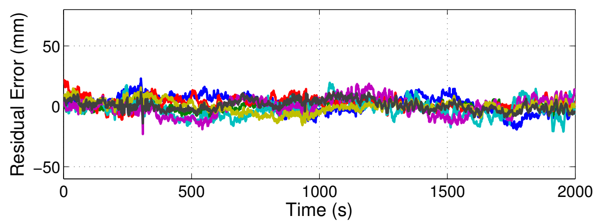

Figure 3.4: Time histories of double-differenced phase residuals for a 2000-second batch of data captured from a low-quality patch antenna. Each trace represents a residual for a different satellite pair. The ensemble average standard deviation of the residuals is 5.5 mill-meters.

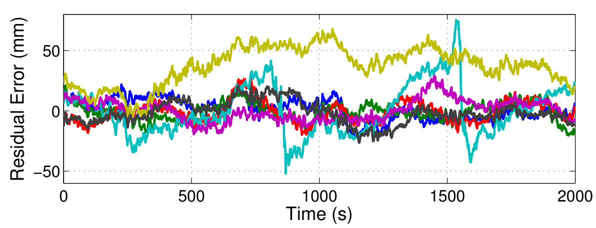

Figure 3.5: Time histories of double-differenced phase residuals for a 2000-second batch of data captured from a smartphone-grade antenna. Each trace represents a residual for a different satellite pair. The ensemble average standard deviation of the residuals is 11.4 millimeters.

multipath environment was similar.

The ensemble average residual standard deviations increase with decreasing antenna quality. The residuals for the survey-grade, low-quality patch, and smartphone-grade antennas have ensemble average standard deviations of 3.4, 5.5, and 11.4 millimeters, respectively. This increase is due to the lower gain and less effective multipath suppression of the lower-quality antennas.

Fig. 3.5 shows the presence of outlier residuals in the data collected from the smartphone-grade antenna. These outliers, one of which persists for over 1000 seconds, are likely caused by either large and irregular azimuth- and elevation-dependent antenna phase center variations or a combination of poor antenna gain in the direction of the non-reference satellite coupled with ample gain in the direction of a multipath signal such that the multipath signal is received with more power than the direct-path signal. Obvious outliers such as these can be automatically excluded by the CDGNSS filter via an innovations test. However, the standard deviation of the remaining residuals still remains large compared to that of the other antennas; the ensemble average standard deviation decreases from 11.4 to 8.6 millimeters upon exclusion of the two large outliers.

For antennas with a large ensemble average standard deviation in their double-differenced phase errors, the time correlation in the phase errors becomes more important. This time correlation, which persists for 100-200 seconds, is a well-studied phenomenon caused by slowly-varying carrier phase multipath [87, 88]. While correlation is present in the residuals of all antenna types, and manifests approximately the same decorrelation time, its effect is more of a problem for low-quality antennas because the phase errors are larger. Such correlation, coupled with a large deviation, ultimately leads to a longer time to ambiguity resolution, as will be shown subsequently.

Given a smartphone antenna's extremely poor gain and multipath suppression as compared to even a low-quality stand-alone patch antenna, one might question the wisdom of attempting a CDGNSS solution using such an antenna. However, the next section reveals that it is indeed possible to achieve a centimeter-accurate positioning solution using a smartphone GNSS antenna despite its poor properties.

3.4 CDGNSS Performance using a Smartphone Antenna

This section discusses the results of performing a CDGNSS solution using data collected from a smartphone-grade antenna and presents two strategies for improving the performance of CDGNSS on smartphones.

Fig. 3.6 shows the result of an attempt to compute a CDGNSS solution using data collected from the GNSS antenna of a smartphone. The cluster of red near the top of the phone represents 400 CDGNSS position estimates over a 5-minute interval, superimposed on the photo and properly scaled. This cluster is referenced to a marker immediately under the phone whose position was surveyed to approximately 1-centimeter accuracy using a high- quality patch antenna. The mean of the clusters horizontal coordinates is approximately 2 centimeters from the phones internal GNSS antenna. As such, Figure 3.6 shows the absolute horizontal accuracy of a CDGNSS solution through the smartphones antenna to be approximately 2 centimeters.

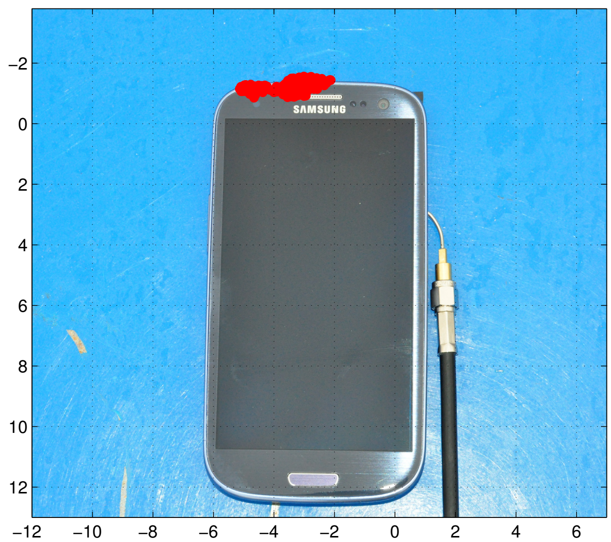

Figure 3.6: A successful CDGNSS solution using data collected from the antenna of a smartphone. The cluster of red near the lower left-hand corner of the phone represents 400 CDGNSS solutions over a 5-minute interval, superimposed on the photo and properly scaled.

Figure 3.7: A successful CDGNSS solution using data collected from the antenna of a smartphone while held approximately steady in the hand of the author. The cluster of red near represents the computed 3-dimensional position of the phone over a 300-second interval, superimposed on the photo and properly scaled.

The data in Figure 3.6 were collected with a large conductive backplane below the smartphone. However, the backplane is unnecessary. Figure 3.7 shows the result of CDGNSS positioning solution computed using data collected from the smartphone antenna while the device was held approximately steady in the hand of the author. The cluster of red represents the computed 3-dimensional position of the phone over a 300-second interval, superimposed on the photo and properly scaled. The authors hand moved some during the interval, as reflected in the figure. Figure 3.8 shows the residuals corresponding to the handheld CDGNSS solution of Figure 3.7. This plot shows how the residuals look in practice for a scenario in which the phone is held by a user. Two of the eight signals received were passing through the author's body. Despite this, the residuals are quite well-behaved, having a moderate standard deviation and no large biases. It is not uncommon for the residuals to look as good

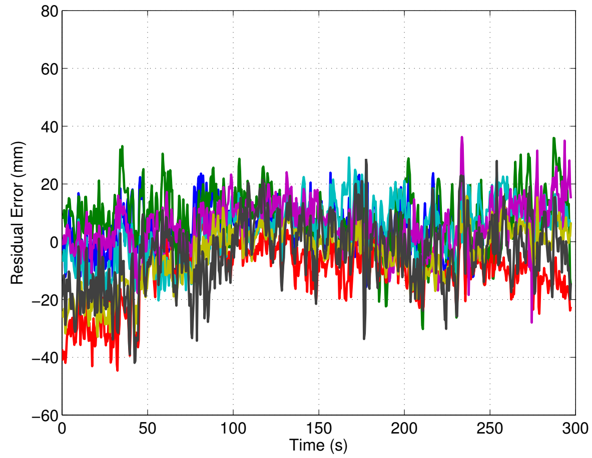

Figure 3.8: A successful CDGNSS solution using data collected from the antenna of a smartphone while held in the hand of the author. The cluster of red near represents the computed 3-dimensional position of the phone over a 300-second interval, superimposed on the photo and properly scaled.

as these, though cases do arise in which the residuals can be much worse, due to a combination of poor antenna gain in the direction of the non-reference satellite coupled with ample gain in the direction of a multipath signal.

Figure 3.9 shows a successful CDGNSS solution using data collected from the antenna of a smartphone while moved slowly in the hand of a user. The yellow star-shaped trace is the actual three-dimensional trajectory through which the user moved the smartphone's antenna, as recovered by processing of the GNSS carrier phase observables. The trajectory is accurate in an absolute sense to a few centimeters. The user had to move slowly because the carrier tracking loop bandwidth was narrowed to improve sensitivity; it took her about 35 seconds to complete the star.

Although the scenarios depicted in Figs. 3.6, 3.7, and 3.9 enjoyed a very short

Figure 3.9: A successful CDGNSS solution using data collected from the antenna of a smartphone while moved slowly in the hand of a user. The yellow star depicts the actual 3-dimensional trajectory of the smartphone's antenna over a 35-second interval, superimposed on the photo and properly scaled.

baseline to a reference antenna (less than 10 meters), similar ambiguity resolution performance is to be expected for baselines shorter than approximately 5 kilometers, as differential ionospheric and tropospheric delays are negligible in this short-baseline regime [98].

The possibility of CDGNSS-enabled centimeter positioning using a smartphone antenna has been previously conjectured [99], but—to the authors' knowledge—Figs. 3.6, 3.7, and 3.9 represent the first published demonstrations that this is indeed possible. This significant result portends a vast expansion of centimeter-accurate positioning into the mass market. However, serious challenges must be overcome before mass-market CDGNSS can become practical, as described next.

3.5 Existing Multipath Mitigation Techniques

Existing techniques for mitigating GNSS carrier phase multipath tend to be unsuitable for low-cost platforms. Signal-processing-based techniques include the Multipath-Estimating Delay-Lock Loop [100, 101], a coupled multipath estimating phase-lock and delay-lock loop [102], signal-to-noise-ratio-based multipath error correction [103], the enhanced strobe correlator [104], and ray-tracing [105]. However, these techniques either require (1) precise, centimeter-accurate *a priori* knowledge of the motion profile of the GNSS antenna [102] and, in some cases, knowledge of the range and bearing of nearby reflection surfaces [105], (2) extra computational power to generate measurements at more than the usual number of correlator taps [100, 101], (3) a lengthy measurement duration, e.g., hundreds of seconds, for the correct identification of the multipath error frequency [103], or (4) a high sampling rate—in excess of 20 (real-valued) mega-samples per second [104].

Each of these enumerated requirements inhibits this chapter's stated goal of fast centimeter positioning on low-cost, computationally limited platforms: (1) because a receiver will in most cases not have precise prior knowledge of its motion profile or of the relative position of nearby reflection surfaces; (2) because the platform is often computationally limited; (3) because hundreds of seconds of processing is too long; and (4) because a high sampling rate would add significant hardware cost to mass market receivers, whose narrow front-end bandwidth renders techniques such as that presented in [104] less effective [106]. Furthermore, many of these techniques have significantly reduced performance when the reflecting surface is less than about 10 meters from the receiving antenna [101, 104], a regime in which multipath-induced phase errors have been shown to be the largest [107].

Antenna-based multipath mitigation strategies, such as specially-designed groundplanes [108, 109] or antenna array solutions [110] are likewise inappropriate, as they require antenna setups that are at present far more expensive than the low-cost antennas that are this chapter's focus.

This chapter's exploration of random antenna motion for multipath mitigation is motivated by the inapplicability of existing multipath mitigation techniques to low-cost GNSS receivers.

3.6 CDGNSS Batch Estimator

The CDGNSS batch estimator employed in this chapter takes as its input double-differenced (DD) carrier phase measurements made between two GNSS receivers, a reference and a rover, and processes these, together with a prior location estimate of the rover antenna center of motion and a model of the magnitude of variations about this center, to estimate (1) a centimeter-accurate relative position time history between the two receivers, and (2) a vector of carrier-phase integer ambiguities.

This chapter employs batch estimation, as opposed to filtering, because batch estimation enables proper treatment of time correlation in the multipath-induced DD carrier phase measurement errors. Due to the estimator state's partial integer nature, state augmentation strategies typically employed to address time-correlated (colored) measurement errors in state estimation, such as those in [77, 90], actually weaken the mixed real-integer model, ultimately degrading the ambiguity resolution performance [93]. Batch estimation, by contrast, enables accurate and optimal treatment of measurement error time correlation in mixed real and integer estimation problems.

3.6.1 State

The batch estimator's state has a real-valued component that indirectly models the time-varying relative position between the reference and rover receiver, and an integer-valued component that models the so-called DD phase ambiguities. Such ambiguities are inherent in carrier phase differential positioning techniques; their resolution has been the topic of much past research [15, 17] and is required to produce a centimeter-accurate CDGNSS positioning solution.

Let k be the total number of measurement epochs input to the batch estimator and T be the time between consecutive epochs. The estimator's real-valued state component at $t_k = kT$, denoted $\mathbf{x}_k$, is given by

$$\mathbf{x}_k = [\mathbf{r}_\mathrm{C}^\mathsf{T}, \mathbf{q}^\mathsf{T}, \mathbf{v}_0^\mathsf{T}, \ldots, \mathbf{v}_{k-1}^\mathsf{T}]^\mathsf{T}, \tag{3.1}$$

where

$\mathbf{r}_\mathrm{C}$ is the 3×1 constant relative position vector between the reference antenna and the center of motion of the rover antenna;

$\mathbf{q}$ is the 3×1 constant relative position vector between the rover antenna center of motion $\mathbf{r}_\mathrm{C}$ and the rover antenna initial relative position $\mathbf{r}_0$ at t_0, i.e., $\mathbf{r}_0 = \mathbf{r}_\mathrm{C} + \mathbf{q}$; and

$\mathbf{v}_i$ for $i = 0, 1, \ldots, k-1$ is a 3×1 vector proportional to the change in relative position between the reference and rover antenna from t_i to t_{i+1}. The exact relationship between $\mathbf{v}_i$ and the change in position is given in the next subsection.

The vectors $\mathbf{q}$ and $\mathbf{v}_i$, $i = 0, 1, \ldots, k-1$, are modeled as independent, zero-mean, Gaussian random vectors with variance σ_{p}^2:

$$\mathbf{q}, \mathbf{v}_i \sim \mathcal{N}(\mathbf{0}_{3\times 1}, \sigma_{\mathrm{p}}^2 \mathbf{I}_{3\times 3}),\ i = 0, 1, \ldots, k-1 \tag{3.2}$$

The estimator's integer-valued state component at t_k, denoted $\mathbf{n}_k$, given by

$$\mathbf{n}_k = [N_1, N_2, \ldots, N_{M_k-1}]^{\mathsf{T}}, \tag{3.3}$$

where

M_k is the total number of satellites providing carrier phase measurements during at least one measurement epoch up to and including time t_k; and

N_i is the integer-valued phase ambiguity for the i^{th} satellite pair, $i = 1, 2 \ldots, M_k - 1$, assumed constant so long as both the reference and rover receivers retain phase lock on the signals tracked.

3.6.2 Relating the State to the Relative Rover Antenna Position

Let the rover antenna position relative to the reference antenna position at t_k be denoted $\mathbf{r}_k$. This vector sequence is assumed to evolve as an Ornstein-Uhlenbeck (OU) process—a mean-reverting first-order Gauss-Markov process. Such a process allows for adequate modeling of the time-correlated and mean-reverting motion a rover antenna would experience when moved randomly in the extended hand of an otherwise stationary user. Let $f = e^{-T/\tau_{\mathrm{p}}}$ be the correlation coefficient of the per-dimension time-varying changes in $\mathbf{r}_k$, where τ_{p} is the correlation time of these changes, in seconds. Under this model, $\mathbf{r}_k$ is related to the components of $\mathbf{x}_k$ by

$$\begin{aligned}
\mathbf{r}_0 &= \mathbf{r}_{\mathrm{C}} + \mathbf{q} \\
\mathbf{r}_k &= \mathbf{r}_{\mathrm{C}} + f\left(\mathbf{r}_{k-1} - \mathbf{r}_{\mathrm{C}}\right) + \sqrt{1-f^2}\,\mathbf{v}_{k-1},\ k = 1, 2, \ldots \\
&= \mathbf{r}_{\mathrm{C}} + \sum_{i=0}^{k-1} f^{k-i}\left(\mathbf{q} + f^{-1}\sqrt{1-f^2}\,\mathbf{v}_i\right),\ k = 1, 2, \ldots
\end{aligned} \tag{3.4}$$

To adapt (3.4) to enforce a static antenna constraint, one can set the standard deviation of $\mathbf{q}$ and $\mathbf{v}_i$, $i = 0, 1, \ldots, k-1$, to zero, i.e., $\sigma_{\mathrm{p}} = 0$.

3.6.3 Measurement Model

The batch estimator's measurement model relates a time history of DD carrier phase measurements to the real- and integer-valued state components. The DD phase measurement at time $t_i \leq t_k$ between satellites j and 1, with 1 denoting the common reference satellite, and the reference (A) and rover (B) receivers, is defined as

$$\phi^{\mathrm{j1}}_{\mathrm{AB},i} \triangleq \left[\phi^{\mathrm{j}}_{\mathrm{A},i} - \phi^{1}_{\mathrm{A},i}\right] - \left[\phi^{\mathrm{j}}_{\mathrm{B},i} - \phi^{1}_{\mathrm{B},i}\right], \tag{3.5}$$

for $j \in \{2, 3, \ldots, M_k\}$, and where $\phi^{\beta}_{\nu,i}$, $\nu \in \{\mathrm{A}, \mathrm{B}\}$, $\beta \in \{1, 2, \ldots, M_k\}$, is the undifferenced carrier phase measurement at t_i between receiver α and satellite β. As this chapter's focus is multipath mitigation, the rover-reference pair is assumed to operate in the short-baseline regime for which atmospheric errors in the DD phase measurements are negligible. In this regime, $\phi^{\mathrm{j1}}_{\mathrm{AB},i}$, which has units of cycles, can be related to $\mathbf{r}_k$ and $\mathbf{n}_k$ by the following nonlinear measurement model [57]:

$$\lambda\phi^{\mathrm{j1}}_{\mathrm{AB},i} = r^{\mathrm{j1}}_{\mathrm{AB},i} + \lambda N_{j-1} + w^{\mathrm{j1}}_{\mathrm{AB},i} \tag{3.6}$$

where

$$r^{\mathrm{j1}}_{\mathrm{AB},i} \triangleq \left(r^{\mathrm{j}}_{\mathrm{A},i} - r^{1}_{\mathrm{A},i}\right) - \left(r^{\mathrm{j}}_{\mathrm{B},i} - r^{1}_{\mathrm{B},i}\right) \tag{3.7}$$

is the DD range between the two receivers and two satellites and

λ is the GNSS signal wavelength;

N_{j-1} is the integer ambiguity for the $(j-1)^{\mathrm{th}}$ satellite pair, as defined previously;

$w^{j1}_{AB,i}$ is the DD carrier phase measurement error at t_i;

$r^{\beta}_{\alpha,i} \triangleq \|\mathbf{r}^{\beta}_i - \mathbf{r}_{\alpha,i}\|$, $\nu \in \{\text{A}, \text{B}\}$, $\beta \in \{1, 2, \ldots, M_k\}$, is the range between receiver α and satellite β at t_i, where $\|\cdot\|$ represents the Euclidean norm;

$\mathbf{r}_{\alpha,i}$ is the 3×1 absolute position of receiver $\nu \in \{\text{A}, \text{B}\}$ at t_i, the time of signal reception, in the global coordinate frame; and

$\mathbf{r}^{\beta}_i$ is the 3×1 absolute position of satellite $\beta \in \{1, 2, \ldots, M_k\}$ at the time of signal transmission, in the global coordinate frame.

Assuming that the position of the reference receiver is known and constant, i.e., $\mathbf{r}_{\text{A},i} = \mathbf{r}_{\text{A}}\ \forall i$, then (3.6) can be linearized about a guess $\bar{\mathbf{r}}_i$ of the relative rover position $\mathbf{r}_i \triangleq \mathbf{r}_{\text{B},i} - \mathbf{r}_{\text{A}}$, resulting in the linearized measurement model

$$\lambda\phi^{j1}_{AB,i} = \bar{r}^{j1}_{AB,i} + \mathbf{H}^{j1}_{AB,i}(\mathbf{r}_i - \bar{\mathbf{r}}_i) + \lambda N_{j-1} + w^{j1}_{AB,i}, \tag{3.8}$$

where $\bar{r}^{j1}_{AB,i}$ is the DD range between the two receivers and satellites j and 1 assuming $\mathbf{r}_i = \bar{\mathbf{r}}_i$, and

$$\mathbf{H}^{j1}_{AB,i} \triangleq \left.\frac{\partial r^{j1}_{AB,i}}{\partial \mathbf{r}_i}\right|_{\mathbf{r}_i = \bar{\mathbf{r}}_i} = \left(\hat{\bar{\mathbf{r}}}^{1}_{B,i}\right)^{\mathsf{T}} - \left(\hat{\bar{\mathbf{r}}}^{j}_{B,i}\right)^{\mathsf{T}}$$

is the 1×3 linearized measurement sensitivity matrix, with $\hat{\bar{\mathbf{r}}}^{\beta}_{B,i}$ being the unit vector pointing from $\mathbf{r}^{\beta}_i$ to $\bar{\mathbf{r}}_{\text{B},i} = \mathbf{r}_{\text{A}} + \bar{\mathbf{r}}_i$, $\beta \in \{1, 2, \ldots, M_k\}$. Rewriting (3.8) with the known terms on the left and the unknown terms on the right results in the following, for $i = 1, 2, \ldots, k$:

$$\lambda\phi^{j1}_{AB,i} - \bar{r}^{j1}_{AB,i} + \mathbf{H}^{j1}_{AB,i}\bar{\mathbf{r}}_i = \mathbf{H}^{j1}_{AB,i}\mathbf{r}_i + \lambda N_{j-1} + w^{j1}_{AB,i} \tag{3.9}$$

The estimator ingests, at t_k, $k = 1, 2, \ldots$, a $(M_k - 1)k \times 1$ vector $\mathbf{Y}_k$ of stacked inter-epoch measurement vectors from t_1 to t_k:

$$\mathbf{Y}_k \triangleq \begin{bmatrix} \mathbf{y}_1 \\ \mathbf{y}_2 \\ \vdots \\ \mathbf{y}_k \end{bmatrix} \tag{3.10}$$

where $\mathbf{y}_i$, $i = 1, 2, \ldots, k$, is an $(M_k - 1) \times 1$ vector containing the known quantities from the left-hand side of (3.9) at t_i for $j = 2, 3, \ldots, M_k$:

$$\mathbf{y}_i \triangleq \begin{bmatrix} \lambda\phi^{21}_{\mathrm{AB},i} - \bar{r}^{21}_{\mathrm{AB},i} + \mathbf{H}^{21}_{\mathrm{AB},i}\bar{\mathbf{r}}_i \\ \lambda\phi^{31}_{\mathrm{AB},i} - \bar{r}^{31}_{\mathrm{AB},i} + \mathbf{H}^{31}_{\mathrm{AB},i}\bar{\mathbf{r}}_i \\ \vdots \\ \lambda\phi^{M_k 1}_{\mathrm{AB},i} - \bar{r}^{\mathrm{j}1}_{\mathrm{AB},i} + \mathbf{H}^{M_k 1}_{\mathrm{AB},i}\bar{\mathbf{r}}_i \end{bmatrix}. \tag{3.11}$$

Using (3.9), it is now possible to linearly relate the real- and integer-valued state components in (3.1) and (3.3) to the DD carrier phase measurements in (3.10), incorporating the kinematics of the relative antenna position as modeled in (3.4). The linearized model becomes

$$\mathbf{Y}_k = \tilde{\mathbf{H}}_{\mathrm{x}k}\mathbf{C}_k\mathbf{x}_k + \tilde{\mathbf{H}}_{\mathrm{n}k}\mathbf{n}_k + \mathbf{W}_k, \tag{3.12}$$

where

$\tilde{\mathbf{H}}_{\mathrm{x}k}$ is the time-dependent measurement sensitivity matrix for the real-valued state component $\mathbf{x}_k$ (expanded below);

$\mathbf{C}_k$ is the time-dependent correlation matrix modeling the dynamics of the reference–rover three-dimensional relative position $\mathbf{r}_k$, as detailed in Sec. 3.6.2 (expanded below);

$\tilde{\mathbf{H}}_{\mathrm{n}k}$ is the measurement sensitivity matrix for the integer-valued state component (expanded below);

$\mathbf{W}_k$ is the discrete-time stacked DD measurement error vector, modeled as zero mean with covariance matrix $\mathbf{R}_k$, i.e., $\mathbf{E}\left[\mathbf{W}_k\right] = \mathbf{0}$ and $\mathbf{E}\left[\mathbf{W}_k\mathbf{W}_k^{\mathsf{T}}\right] = \mathbf{R}_k$ (expanded below).

$\tilde{\mathbf{H}}_{\mathrm{x}k}$, $\mathbf{C}_k$, $\tilde{\mathbf{H}}_{\mathrm{n}k}$, and $\mathbf{W}_k$ can be expanded as

$$\tilde{\mathbf{H}}_{\mathrm{x}k} \triangleq \begin{bmatrix} \mathbf{H}_{\mathrm{AB},1} & \mathbf{0} & \dots & \mathbf{0} \\ \mathbf{0} & \mathbf{H}_{\mathrm{AB},2} & \ddots & \vdots \\ \vdots & & & \mathbf{0} \\ \mathbf{0} & \mathbf{0} & & \mathbf{H}_{\mathrm{AB},k} \end{bmatrix} \tag{3.13}$$

$$\mathbf{C}_k \triangleq \mathbf{I}_{3\times 3} \otimes \begin{bmatrix} 1 & f^0 & 0 & \dots & \dots & 0 \\ 1 & f^1 & af^0 & 0 & \dots & 0 \\ \vdots & \vdots & \vdots & \ddots & \ddots & \vdots \\ 1 & f^{k-1} & af^{k-2} & \dots & af^0 & 0 \\ 1 & f^k & af^{k-1} & \dots & af^1 & af^0 \end{bmatrix} \tag{3.14}$$

$$\tilde{\mathbf{H}}_{\mathrm{n}k} \triangleq \begin{bmatrix} \lambda\mathbf{I}_{(\mathrm{M_k}-1)\times(\mathrm{M_k}-1)} \\ \lambda\mathbf{I}_{(\mathrm{M_k}-1)\times(\mathrm{M_k}-1)} \\ \vdots \\ \lambda\mathbf{I}_{(\mathrm{M_k}-1)\times(\mathrm{M_k}-1)} \end{bmatrix} \tag{3.15}$$

$$\mathbf{W}_k \triangleq \begin{bmatrix} \mathbf{w}_1 \\ \mathbf{w}_2 \\ \vdots \\ \mathbf{w}_k \end{bmatrix}, \tag{3.16}$$

where "$\otimes$" denotes the Kronecker product, f is the correlation coefficient of the time-varying reference–rover relative position changes, as introduced in (3.4), $a \triangleq$

$\sqrt{1-f^2}$,

$$\mathbf{w}_i \triangleq \begin{bmatrix} w_{\mathrm{AB},i}^{21} \\ w_{\mathrm{AB},i}^{31} \\ \vdots \\ w_{\mathrm{AB},i}^{M_k 1} \end{bmatrix}, \ i = 1, 2, \ldots, k$$

and

$$\mathbf{H}_{\mathrm{AB},i} \triangleq \begin{bmatrix} \mathbf{H}_{\mathrm{AB},i}^{21} \\ \mathbf{H}_{\mathrm{AB},i}^{31} \\ \vdots \\ \mathbf{H}_{\mathrm{AB},i}^{M_k 1} \end{bmatrix}, \ i = 1, 2, \ldots, k.$$

The measurement error covariance matrix $\mathbf{R}_k$ facilitates proper modeling of the magnitude and time correlation of the DD phase measurement errors, which, similar to the rover antenna position, are assumed to evolve as an OU process. $\mathbf{R}_k$ can be expanded as

$$\mathbf{R}_k \triangleq \mathbf{R}_\phi \otimes \mathbf{D}_k, \tag{3.17}$$

where

$$\mathbf{R}_\phi \triangleq \sigma_\phi^2 \begin{bmatrix} 4 & 2 & \ldots & 2 \\ 2 & 4 & & \vdots \\ \vdots & & \ddots & 2 \\ 2 & \ldots & 2 & 4 \end{bmatrix} \tag{3.18}$$

models the *intra*-epoch measurement error correlation resulting from the presence of a common reference satellite in the DD measurements [see [45], Eq. (19)], and σ_ϕ^2 is the average variance of the reference and rover antenna undifferenced phase error:

$$\sigma_\phi^2 \triangleq \frac{\sigma_{\phi,\mathrm{A}}^2 + \sigma_{\phi,\mathrm{B}}^2}{2}. \tag{3.19}$$

$\mathbf{D}_k$ models the *inter*-epoch measurement error correlation, i.e., the correlation in time. The measurement error time history for each DD satellite pair is modeled as an OU process, which is the simplest process that accurately models the time-correlated- and mean-reverting-nature of the DD phase errors. Choosing an OU process also simplifies the relationship between statistics of the antenna motion, also modeled as an OU process [see (3.4)], to the statistics of DD measurement errors, as will be detailed later on. $\mathbf{D}_k$ can be expanded as

$$\mathbf{D}_k \triangleq \begin{bmatrix} h(0) & h(1) & \dots & h(k-1) \\ h(1) & h(0) & \dots & h(k-2) \\ \vdots & \vdots & \vdots & \vdots \\ h(k-2) & h(k-3) & \dots & h(1) \\ h(k-1) & h(k-2) & \dots & h(0) \end{bmatrix}, \tag{3.20}$$

where $h(i)$ is the autocorrelation function of the DD reference and rover antenna phase errors, defined as

$$h(i) \triangleq \frac{\sigma^2_{\phi,\mathrm{A}} g^i_{\mathrm{A}} + \sigma^2_{\phi,\mathrm{B}} g^i_{\mathrm{B}}}{\sigma^2_{\phi,\mathrm{A}} + \sigma^2_{\phi,\mathrm{B}}}, \;\; i = 1, 2, \dots, k, \tag{3.21}$$

and

$$g_{\mathrm{A}} \triangleq e^{-T/\tau_{\phi,\mathrm{A}}}$$

$$g_{\mathrm{B}} \triangleq e^{-T/\tau_{\phi,\mathrm{B}}}$$

are the correlation factors of the undifferenced rover and reference phase errors, which are modeled as exponentially decreasing with correlation times $\tau_{\phi,\mathrm{A}}$ and $\tau_{\phi,\mathrm{B}}$, respectively.

3.6.4 State Estimation

Optimal state estimates $\hat{\mathbf{x}}_k$ and $\hat{\mathbf{n}}_k$, $k = 1, 2, \dots$, are produced by incorporating all measurements and *a priori* information up to and including time t_k.

A square-root information implementation of a batch estimator is employed for an accurate and computationally-efficient solution [44, 59].

A priori state information is provided to the estimator to enforce the models for $\mathbf{q}$ and $\mathbf{v}_i$, $i = 1, 2 \ldots, k$, detailed in (3.2), and to provide an approximation for the relative rover antenna center of motion $\mathbf{r}_{\mathrm{C}}$. This latter information is provided to the estimator in the form of a normalized square-root information equation:

$$\bar{\mathbf{z}}_{\mathrm{x}k} = \bar{\mathbf{R}}_{\mathrm{xx}k}\mathbf{x}_k + \bar{\mathbf{w}}_{\mathrm{x}k} \tag{3.22}$$

where

$\bar{\mathbf{z}}_{\mathrm{xk}} \triangleq \bar{\mathbf{R}}_{\mathrm{xx}k}\bar{\mathbf{x}}_k$ is the $3(k+2) \times 1$ nonhomogeneous term;

$\bar{\mathbf{x}}_k \triangleq \left[\bar{\mathbf{r}}_{\mathrm{C}}^{\mathsf{T}}, \mathbf{0}_{3\times1}^{\mathsf{T}}, \ldots, \mathbf{0}_{3\times1}^{\mathsf{T}}\right]$ is the prior estimate for the real-valued state component;

$\bar{\mathbf{R}}_{\mathrm{xx}k}$ is the square-root information matrix (SRIM) containing the prior information certainty corresponding to $\bar{\mathbf{x}}_k$ (expanded below); and

$\bar{\mathbf{w}}_{\mathrm{x}k}$ is the $3(k+2) \times 1$ error vector, modeled as zero mean with unit covariance, i.e., $\mathbf{E}\left[\bar{\mathbf{w}}_{\mathbf{x}k}\right] = \mathbf{0}_{3(\mathrm{k}+2)\times1}$ and $\mathbf{E}\left[\bar{\mathbf{w}}_{\mathbf{x}k}\bar{\mathbf{w}}_{\mathbf{x}k}^{\mathsf{T}}\right] = \mathbf{I}_{3(\mathrm{k}+2)\times3(\mathrm{k}+2)}$.

$\bar{\mathbf{R}}_{\mathrm{xx}k}$ is a block diagonal matrix, expanded as

$$\bar{\mathbf{R}}_{\mathrm{xx}k} \triangleq \begin{bmatrix} \frac{1}{\sigma_{\mathrm{r_C}}}\mathbf{I}_{3\times3} & \mathbf{0}_{3\times3} & \ldots & \mathbf{0}_{3\times3} \\ \mathbf{0}_{3\times3} & \frac{1}{\sigma_{\mathrm{p}}}\mathbf{I}_{3\times3} & \ldots & \mathbf{0}_{3\times3} \\ \vdots & \vdots & \ddots & \vdots \\ \mathbf{0}_{3\times3} & \mathbf{0}_{3\times3} & \ldots & \frac{1}{\sigma_{\mathrm{p}}}\mathbf{I}_{3\times3} \end{bmatrix}, \tag{3.23}$$

where $\sigma_{\mathrm{r_C}}$ is the per-dimension error standard deviation of $\bar{\mathbf{r}}_{\mathrm{C}}$, in meters.

The carrier phase measurements are also modeled by a normalized square-root information equation through the following transformation of $\mathbf{Y}_k$:

$$\mathbf{z}_k \triangleq \mathbf{R}_{\mathrm{a}k}^{-\mathsf{T}} \mathbf{Y}_k \tag{3.24}$$

$$= \mathbf{H}_{\mathrm{x}k}\mathbf{x}_k + \mathbf{H}_{\mathrm{n}k}\mathbf{n}_k + \mathbf{w}_k \tag{3.25}$$

where

$\mathbf{R}_{\mathrm{a}k} \triangleq \mathrm{chol}\left(\mathbf{R}_k\right)$ is the Choleski factorization, i.e., the inverse square root, of the measurement error covariance matrix $\mathbf{R}_k$;

$\mathbf{z}_k$ is the $k(M_k - 1) \times 1$ nonhomogeneous term corresponding to $\mathbf{x}_k$ and $\mathbf{n}_k$;

$\mathbf{H}_{\mathrm{x}k} \triangleq \mathbf{R}_{\mathrm{a}k}^{-\mathsf{T}} \tilde{\mathbf{H}}_{\mathrm{x}k}\mathbf{C}_k$ is the normalized measurement sensitivity matrix for the real-valued state component $\mathbf{x}_k$;

$\mathbf{H}_{\mathrm{n}k} \triangleq \mathbf{R}_{\mathrm{a}k}^{-\mathsf{T}} \tilde{\mathbf{H}}_{\mathrm{n}k}$ is the normalized measurement sensitivity matrix for the integer-valued state component $\mathbf{n}_k$; and

$\mathbf{w}_k \triangleq \mathbf{R}_{\mathrm{a}k}^{-\mathsf{T}} \mathbf{W}_k$ is the normalized measurement error, modeled as zero mean with unit covariance, i.e., $\mathbf{E}\left[\mathbf{w}_k\right] = \mathbf{0}_{\mathrm{k(M_k-1)\times 1}}$ and $\mathbf{E}\left[\mathbf{w}_k\mathbf{w}_k^{\mathsf{T}}\right] = \mathbf{I}_{\mathrm{k(M_k-1)\times k(M_k-1)}}$.

Optimal estimates of the real- and integer-valued state elements can be found by choosing $\mathbf{x}_k$ and $\mathbf{n}_k$ to minimize the following cost function:

$$\begin{aligned} J\left(\mathbf{x}_k, \mathbf{n}_k\right) =& \| \underbrace{\mathbf{H}_{\mathrm{x}k}\mathbf{x}_k + \mathbf{H}_{\mathrm{n}k}\mathbf{n}_k - \mathbf{z}_k}_{\text{Normalized Measurement Error}} \|^2 \\ &+ \| \underbrace{\bar{\mathbf{R}}_{\mathrm{xx}k}\mathbf{x}_k - \bar{\mathbf{z}}_{\mathrm{x}k}}_{\text{Normalized Prior Error}} \|^2 \end{aligned} \tag{3.26}$$

where $\|\cdot\|$ represents the Euclidean norm. Eq. (3.26) can be written equivalently as

$$J\left(\mathbf{x}_k, \mathbf{n}_k\right) = \left\| \underbrace{\begin{bmatrix} \mathbf{H}_{\mathrm{x}k} & \mathbf{H}_{\mathrm{n}k} \\ \bar{\mathbf{R}}_{\mathrm{xx}k} & \mathbf{0} \end{bmatrix}}_{\mathbf{H}} \begin{bmatrix} \mathbf{x}_k \\ \mathbf{n}_k \end{bmatrix} - \underbrace{\begin{bmatrix} \mathbf{z}_k \\ \bar{\mathbf{z}}_{\mathrm{x}k} \end{bmatrix}}_{\mathbf{z}} \right\|^2 . \tag{3.27}$$

By QR factorization [111], the block matrix $\mathbf{H}$ in (3.27) can be transformed into the product of a square, orthonormal matrix and an upper triangular matrix:

$$\mathbf{Z} = \mathbf{Q}_{\mathrm{b}}\mathbf{R}_{\mathrm{b}} \tag{3.28}$$

By left multiplying $\mathbf{H}$ and $\mathbf{z}$ of (3.27) by $\mathbf{Q}_{\mathrm{b}}^{\mathsf{T}}$, the cost function can be written equivalently as

$$J\left(\mathbf{x}_k, \mathbf{n}_k\right) = \left\| \begin{bmatrix} \mathbf{R}_{\mathrm{xx}k} & \mathbf{R}_{\mathrm{xn}k} \\ \mathbf{0} & \mathbf{R}_{\mathrm{nn}k} \\ \mathbf{0} & \mathbf{0} \end{bmatrix} \begin{bmatrix} \mathbf{x}_k \\ \mathbf{n}_k \end{bmatrix} - \begin{bmatrix} \mathbf{z}_{\mathrm{x}k} \\ \mathbf{z}_{\mathrm{n}k} \\ \mathbf{z}_{\mathrm{r}} \end{bmatrix} \right\|^2, \tag{3.29}$$

where

$\mathbf{R}_{\mathrm{xx}k}$ is the SRIM corresponding to $\mathbf{x}_k$ and $\mathbf{z}_{\mathrm{x}k}$;

$\mathbf{R}_{\mathrm{xn}k}$ is the SRIM corresponding to $\mathbf{n}_k$ and $\mathbf{z}_{\mathrm{x}k}$;

$\mathbf{z}_{\mathrm{xk}}$ is the nonhomogeneous term corresponding to $\mathbf{x}_k$ and $\mathbf{n}_k$;

$\mathbf{R}_{\mathrm{nn}k}$ is the SRIM corresponding to $\mathbf{n}_k$ and $\mathbf{z}_{\mathrm{n}k}$;

$\mathbf{z}_{\mathrm{xk}}$ is the nonhomogeneous term corresponding to $\mathbf{n}_k$; and

$\mathbf{z}_{\mathrm{r}}$ is the residual nonhomogeneous term.

This transformation leaves the cost in a convenient form that isolates a term involving only the integer-valued state component:

$$\begin{aligned} J\left(\mathbf{x}_k, \mathbf{n}_k\right) = & \underbrace{\left\|\mathbf{R}_{\mathrm{xx}k}\mathbf{x}_k + \mathbf{R}_{\mathrm{xn}k}\mathbf{n}_k - \mathbf{z}_{\mathrm{x}k}\right\|^2}_{\text{Term involving the integer- and real-valued states}} \\ & + \underbrace{\left\|\mathbf{R}_{\mathrm{nn}k}\mathbf{n}_k - \mathbf{z}_{\mathrm{n}k}\right\|^2}_{\text{Term involving only the integer-valued state}} + \underbrace{\left\|\mathbf{z}_{\mathrm{r}}\right\|^2}_{\text{Residual term}} \end{aligned} \tag{3.30}$$

Minimization of (3.30) proceeds as follows: First, one finds, via efficient integer least-squares techniques [15, 33], the integer-valued vector state estimate $\hat{\mathbf{n}}_k$ that minimizes the second term on the right-hand side, the term involving only the integer-valued state. This is known as integer ambiguity resolution. Next, $\hat{\mathbf{n}}_k$ is inserted into the first term, the term involving both the integer- and real-valued states. At this point, it is possible to find the real-valued state estimate $\hat{\mathbf{x}}_k$ that reduces the first term to zero. By this process the state that minimizes $J(\mathbf{x}_k, \mathbf{n}_k)$ is found subject to an integer constraint on $\mathbf{n}_k$.

3.6.5 Phase Residuals

In addition to a time history of centimeter-accurate position estimates, the CDGNSS batch estimator outputs a time history of phase residuals $\tilde{\mathbf{Y}}_k$, which amount to departures of each DD phase measurement from phase alignment at the estimated phase center of the antenna. The vector of phase residuals is defined as

$$\tilde{\mathbf{Y}}_k \triangleq \mathbf{Y}_k - \mathbf{h}_k(\hat{\mathbf{x}}_k),$$

where

$$\mathbf{h}_k(\hat{\mathbf{x}}_k) \triangleq \begin{bmatrix} \mathbf{r}_{\mathrm{AB},1}(\hat{\mathbf{x}}_k) + \lambda \mathbf{I}_{(\mathrm{M_k}-1)\times(\mathrm{M_k}-1)} \hat{\mathbf{n}}_k \\ \mathbf{r}_{\mathrm{AB},2}(\hat{\mathbf{x}}_k) + \lambda \mathbf{I}_{(\mathrm{M_k}-1)\times(\mathrm{M_k}-1)} \hat{\mathbf{n}}_k \\ \vdots \\ \mathbf{r}_{\mathrm{AB},k}(\hat{\mathbf{x}}_k) + \lambda \mathbf{I}_{(\mathrm{M_k}-1)\times(\mathrm{M_k}-1)} \hat{\mathbf{n}}_k \end{bmatrix} \tag{3.31}$$

and

$$\mathbf{r}_{\mathrm{AB},i}\left(\hat{\mathbf{x}}_k\right) \triangleq \begin{bmatrix} r^{21}_{\mathrm{AB},i}\left(\hat{\mathbf{x}}_k\right) \\ r^{31}_{\mathrm{AB},i}\left(\hat{\mathbf{x}}_k\right) \\ \vdots \\ r^{\mathrm{M_k}1}_{\mathrm{AB},i}\left(\hat{\mathbf{x}}_k\right) \end{bmatrix}, \quad i = 1, 2, \ldots, k. \tag{3.32}$$

The quantity $r^{\mathrm{j}1}_{\mathrm{AB},i}\left(\hat{\mathbf{x}}_k\right),\ j = 2, 3, \ldots, M_k$ is the DD range between satellites j and the reference satellite 1 at time t_i, which can be computed from the time-varying estimated reference-to-rover relative antenna position $\mathbf{r}_i$ and the position of the reference antenna $\mathbf{r}_{\mathrm{A}}$ using (4.20); $\mathbf{r}_i$ is derived from $\hat{\mathbf{x}}_k$ using using (3.4).

Phase residuals are examined in the next section to aid in motivating antenna motion as an effective strategy to improve the performance of CDGNSS integer ambiguity resolution.

3.7 Carrier Phase Multipath Error Model

In the short-baseline CDGNSS regime (i.e., when the rover and reference antennas are separated by less than about 5 km), multipath errors remain substantial in DD carrier phase measurements whereas all other modeling errors are effectively cancelled by the DD operation detailed in (4.17) [112]. This explains why multipath errors are the primary impediment to fast carrier phase ambiguity resolution in the short-baseline regime [103, 113].

This section exploits an existing analytical model for carrier phase multipath to develop an approximate statistical relationship between (1) rover antenna quality and dynamics, and (2) carrier phase multipath errors. Subsequent sections will analyze ambiguity resolution performance in terms of multipath errors to complete the linkage from antenna quality and dynamics to ambiguity resolution success rate.

3.7.1 Single Reflection Multipath Error Model

Multipath-induced error in the phase estimates produced by a GNSS receiver's phase-locked loop as it tracks the carrier phase of a particular signal from a specific satellite can be approximated, in radians, by the following single-reflection error model [114]:

$$\psi \approx \arctan \frac{\alpha \sin \theta}{1 + \alpha \cos \theta}. \tag{3.33}$$

In this model, α is the power ratio and θ is the phase difference, in radians, between the reflected and line-of-sight (LOS) signals received by a GNSS antenna. Reflected signals are typically associated with low-elevation LOS signals and have significant non-right-hand-circularly-polarized (non-RHCP) components [115]. To attenuate reflected signals, high-quality antennas are designed to have a high axial ratio (a high level preference for RHCP) gain patterns that reject low-elevation signals. Because lower-quality antennas are worse in each of these properties, they attenuate signal reflections to a lesser extent. Thus, in the remainder of this chapter, α is considered a proxy for reciprocal antenna quality, with α decreasing as antenna quality increases.

Although multipath commonly involves multiple reflections, the single-reflection model in (3.33) remains useful because errors can often be traced to a single dominant reflection [116]. The phase difference θ can be expanded as [105]

$$\theta = 2\pi \left(\frac{d_{\mathrm{ref}} - d_{\mathrm{los}}}{\lambda} \right), \tag{3.34}$$

where d_{ref} is the total distance traveled by the reflecting signal and d_{los} is the total distance traveled by the line-of-sight signal from the satellite to the receiving antenna, in meters. The next two subsections invoke (3.33) and (3.34) to illustrate how ψ is affected by satellite motion, receiver motion, and antenna quality.

3.7.2 Influence of Motion on Phase Errors

Carrier phase multipath has a spatial correlation on the order of one wavelength—approximately 19 centimeters at the GPS L1 frequency [117]. This spatial sensitivity has two important consequences: (1) multipath errors for each satellite signal are largely uncorrelated (between signals) at a particular location, and (2) the time correlation of errors for each signal is strongly influenced by receiver motion. The second of these consequences is further explained here.

Due to satellite motion, the difference $d_{\mathrm{ref}} - d_{\mathrm{los}}$, and, by extension, ψ, varies over time. For static antennas, ψ changes at a rate proportional to the distance between the receiving antenna and the closest reflecting surface [105, 112]. As most reflection surfaces are nearby (within 10 meters), carrier phase errors with correlation times in the hundreds of seconds are common [87, 112]. For moving antennas, ψ varies as a function of both satellite motion and receiver antenna motion. Due to the close proximity of the receiver antenna to the reflection surface, receiver motion—even compact wavelength-scale motion—induces significant changes to $d_{\mathrm{ref}} - d_{\mathrm{los}}$, and, by extension, to ψ.

To illustrate the influence of motion on phase errors, carrier phase data were captured from a smartphone-grade antenna both while the antenna was static and while it was moved in a quasi-random manner within a wavelength-scale volume. The data capture setup was as follows: (1) radio frequency (RF) signals were received through the smartphone's internal antenna, RF filters, and low-noise amplifier and were captured and digitized for external processing (see [36], Fig. 1, for further details); (2) data for the static antenna scenario were obtained while the phone rested on a flat plastic surface affixed to the top of a 2-meter tripod; (3) data for the dynamic antenna scenario were obtained while the smartphone was moved randomly in the outstretched hand of an otherwise stationary user. In both scenarios, the same set of satellites was tracked, as data were captured at nearly the same time and location.

Fig. 3.10 shows DD the phase residuals and Fig. 3.11 shows the corresponding autocorrelation functions for the static (top panels) and dynamic (bottom panels) scenarios. It is clear that the phase residuals transform from slowly-varying ($>$ 100-second correlation) when the antenna is static to quickly-varying (sub-second correlation) when the antenna is dynamic.

3.7.3 Relationship between Antenna Quality and Dynamics and Phase Error Statistics

This section formalizes the relationship between antenna quality and dynamics, characterized by α, σ_{p} and τ_{p}, and the undifferenced phase error, characterized by either $\{\sigma_{\phi,\mathrm{B}},\ \tau_{\phi,\mathrm{B}}\}$ or $\{\sigma_{\phi,\mathrm{A}},\ \tau_{\phi,\mathrm{A}}\}$, the rover and reference antenna phase error statistics, respectively. Let w_{α}^{β}, for $\nu \in \{\mathrm{A}, \mathrm{B}\}$, and $\beta \in \{1, 2, \ldots, M_k\}$ be the undifferenced contribution to the double differenced carrier phase measurement noise term $w_{\mathrm{AB},i}^{\mathrm{j1}}$ introduced in (3.8). Atmospheric and clock errors are ignored in w_{α}^{β} because they cancel in the double difference operation. Multipath errors are assumed to dominate the remaining carrier phase noise so that $w_{\alpha}^{\beta} \triangleq \psi$. The quantities $\{\sigma_{\phi,\mathrm{A}},\ \tau_{\phi,\mathrm{A}}\}$ and $\{\sigma_{\phi,\mathrm{B}},\ \tau_{\phi,\mathrm{B}}\}$ are thus interpreted as the standard deviation and time correlation of ψ for the respective antenna. For notational convenience in this section, $\{\sigma_{\phi,\mathrm{u}},\ \tau_{\phi,\mathrm{u}}\}$ represents the generalized statistics of the undifferenced phase error, with u referring to either A or B.

Due to the strongly nonlinear nature of (3.33), the statistical relationship between phase errors and antenna quality and dynamics is difficult to define as closed-form expression. Instead, a Monte-Carlo-type simulation study was performed to approximate this relationship; the study's procedure is detailed in Appendix 3.12.1.

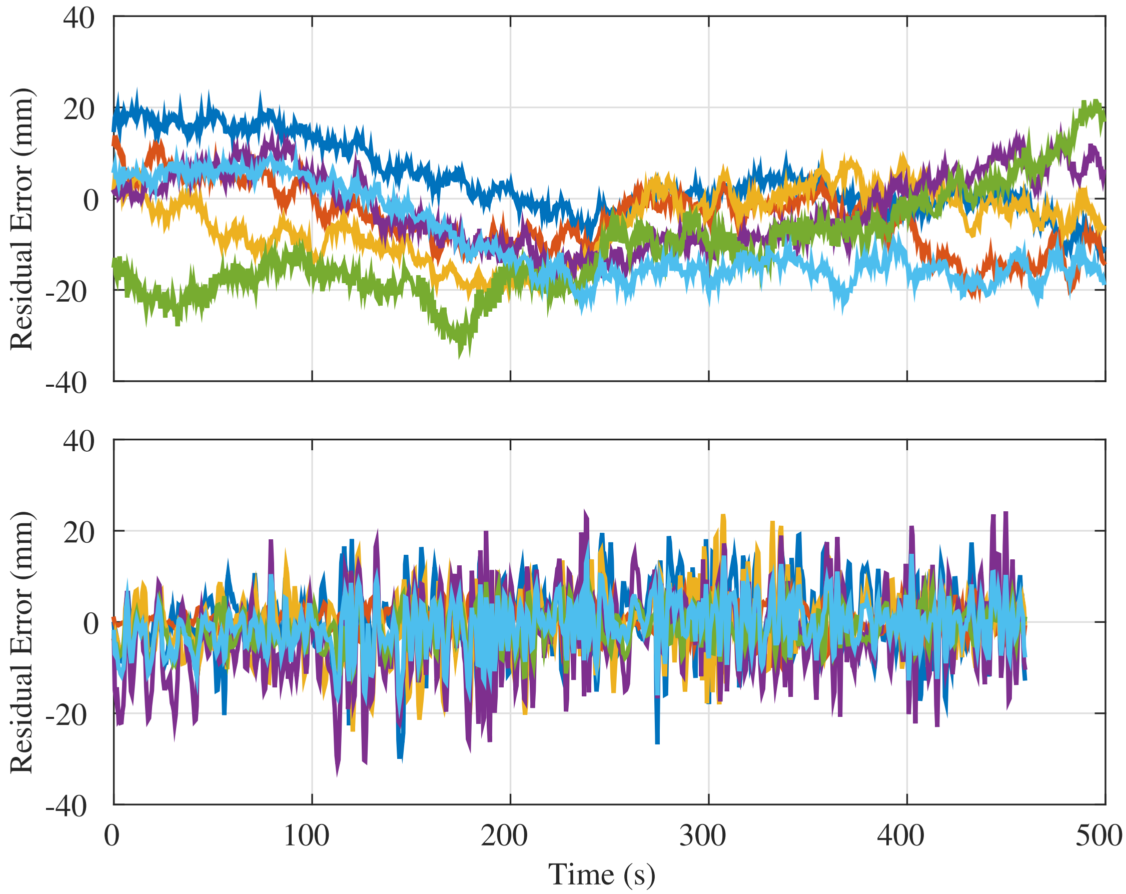

Figure 3.10: Time histories of phase residuals for a batch of data captured from a smartphone-grade antenna while static (top panel) and while in motion (bottom panel). Each trace represents a DD phase residual history for a different satellite pair. A survey-grade antenna was used as the reference antenna, which remained static throughout the data capture interval.

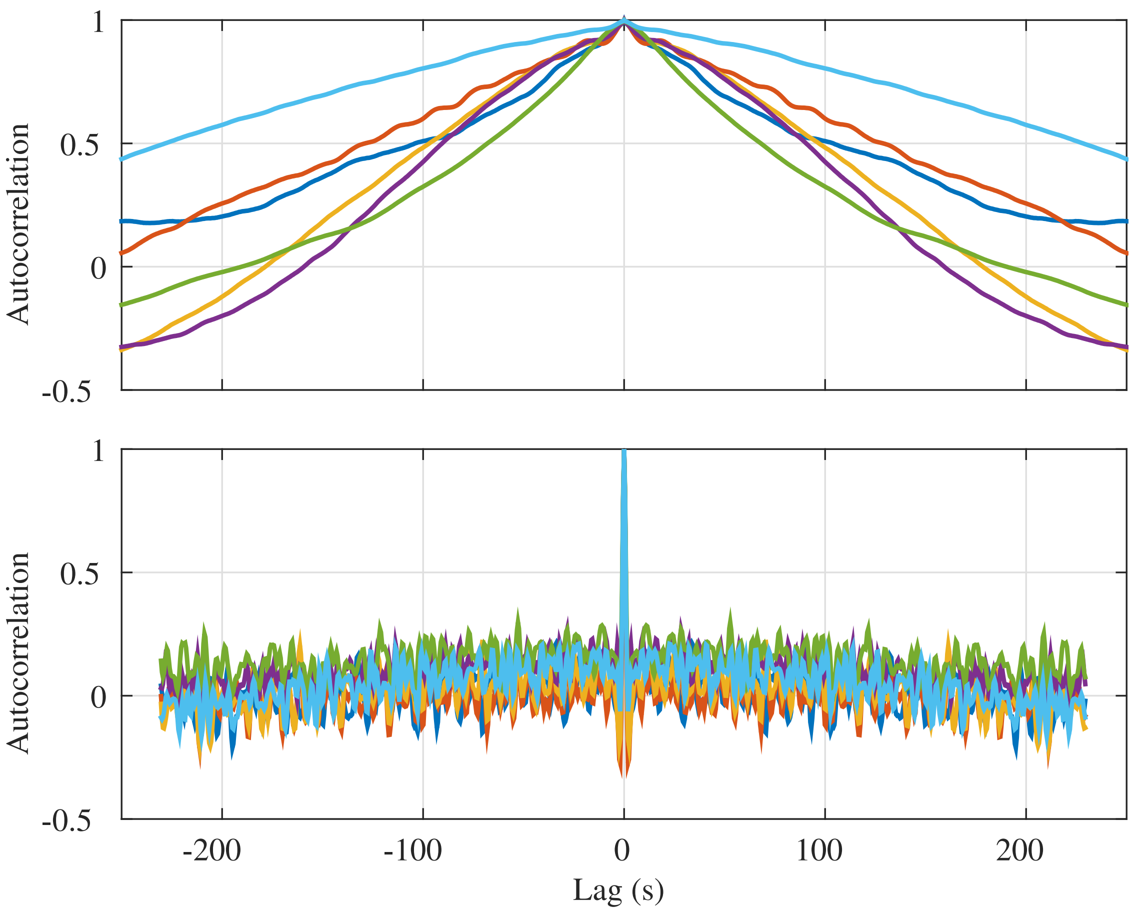

Figure 3.11: Autocorrelation functions corresponding to the phase residuals in Fig. 3.10.

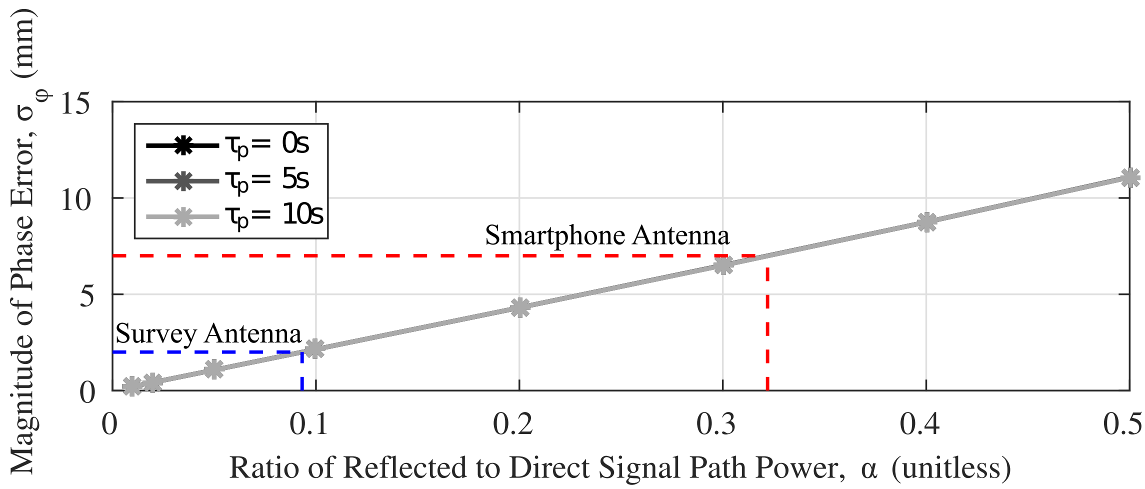

Figure 3.12: Results of a Monte-Carlo-type simulation study showing the phase error standard deviation $\sigma_{\phi,\mathrm{u}}$ as a function of the antenna quality, characterized by α, and the correlation time of the antenna dynamics, characterized by τ_p. The traces for all three values of τ_p are coincident, indicating that $\sigma_{\phi,\mathrm{u}}$ does not depend on τ_p. The dependence of $\sigma_{\phi,\mathrm{u}}$ on α is approximately linear with the slope shown. Points along the $\sigma_{\phi,\mathrm{u}}(\alpha)$ trace corresponding to a survey-grade and smartphone-grade antenna have been marked. These are based on empirical values for $\sigma_{\phi,\mathrm{u}}$ [2].

Figures 3.12 and 3.13 indicate the significant relationships revealed by the study, which can be summarized as follows:

- $\sigma_{\phi,\mathrm{u}} \cong 21.9 \cdot \alpha$ for $0 \leq \alpha \leq 0.5$. A linear relationship is consistent with (3.33) for small α, since $\psi \to \alpha \sin\theta$ as $\alpha \to 0$.
- $\tau_{\phi,\mathrm{u}} \cong 0.21 \cdot \tau_\mathrm{p} \cdot e^{-2.7\sigma_\mathrm{p}}$ for $0 \leq \tau_\mathrm{p} \leq 10$ seconds.
- $\sigma_{\phi,\mathrm{u}}$ does not depend significantly on σ_p or τ_p, and $\tau_{\phi,\mathrm{u}}$ does not depend on α.

The next section characterizes the dependence of CDGNSS integer ambiguity resolution on $\{\sigma_{\phi,\mathrm{u}}, \tau_{\phi,\mathrm{u}}\}$, so that, together with the results of this section, one can

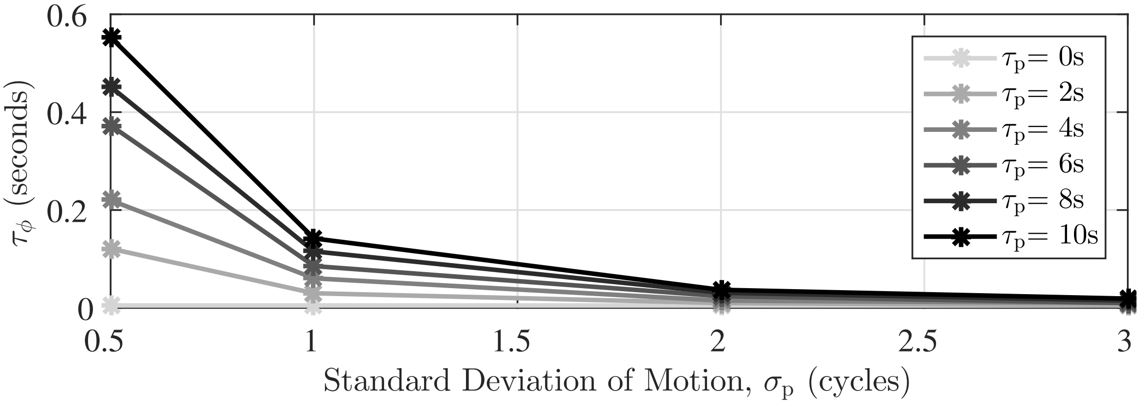

Figure 3.13: Results of a Monte-Carlo-type simulation study showing the phase error correlation time $\tau_{\phi,\mathrm{u}}$ as a function of the standard deviation and correlation time of the antenna dynamics, σ_{p} and τ_{p}, respectively. It is clear that $\tau_{\phi,\mathrm{u}}$ decreases exponentially in σ_{p} and is approximately linear in τ_{p}.

ultimately characterize ambiguity resolution performance in terms of antenna quality and dynamics.

3.8 Effect of Antenna Quality and Dynamics on Ambiguity Resolution

This chapter's primary claim is that gentle wavelength-scale random antenna motion is an effective strategy to reduce TAR when performing a CDGNSS solution based on data collected from a low-quality antenna. Such motion improves the so-called ambiguity success rate (ASR), i.e., the probability that all integer ambiguities are successfully resolved, as compared to a static antenna CDGNSS solution. This section completes the linkage from $\{\alpha,\ \sigma_{\mathrm{p}},\tau_{\mathrm{p}}\}$ to ASR and thus to TAR.

Previous work has developed closed-form expressions relating the undifferenced phase error statistics $\{\sigma_{\phi,\mathrm{u}},\ \tau_{\phi,\mathrm{u}}\}$ to the so-called Ambiguity Dilution of Precision (ADOP) [118, 119], a scalar metric that can be used to compute a tight approximation of ASR [73]. These expressions, however, make one of two simplifying assumptions: they apply either under a short-time assumption, where phase error time correlation is considered but satellite motion is assumed negligible, or under a long-time assumption, where satellite motion is considered but phase error time correlation is assumed negligible. It does not appear possible to develop a closed-form approximation of ADOP which accounts for both satellite motion and error time correlation, yet it can be shown by simulation that both of these significantly affect ADOP, and thus ASR. Moreover, neither the short- nor long-term analytical expressions from [118, 119] account for the effect of receiver antenna trajectory uncertainty within the CDGNSS estimator on ASR.

3.8.1 Approach

This chapter's approach is to employ Monte-Carlo simulation and the full batch CDGNSS estimator introduced in Sec. 4.2, complete with a statistical antenna trajectory model, to determine the relationship between $\{\alpha, \sigma_{\mathrm{p}}, \tau_{\mathrm{p}}\}$ and ASR. The relationship is then validated with real data. The simulation study takes the following steps: (1) the values of $\{\alpha, \sigma_{\mathrm{p}}, \tau_{\mathrm{p}}\}$ given in Table 3.3 are used to generate a simulated rover antenna motion trajectory and are also mapped to corresponding values for $\tau_{\phi,\mathrm{u}}$ and $\sigma_{\phi,\mathrm{u}}$ using the model from Sec. 3.7; (2) the simulated antenna motion trajectory and the values for $\tau_{\phi,\mathrm{u}}$ and $\sigma_{\phi,\mathrm{u}}$ are used to generate simulated undifferenced carrier phase data for each satellite in the simulation; (3) the simulated carrier phase data are fed to the batch CDGNSS estimator to produce a series of batch solutions, and (4) analytical bounds on, and empirical estimates of, ASR are computed from the batch estimator's outputs after each measurement epoch; analytical bounds are computed using the estimator's state covariance matrix and

Table 3.3: Model Parameters for Simulation Study of ASR

Motion Model				Quality		
	τ_{p} (sec)	σ_{p} (cycles)	$\tau_{\phi,\mathrm{u}}$ (sec)		α	$\sigma_{\phi,\mathrm{u}}$ (mm)
Static	n/a	0	100	Survey	0.09	2
Dynamic	2	0.5	0.12	Smartphone	0.32	7

empirical estimates are computed by comparing the batch estimator's integer ambiguity state estimate to the truth values. For all tests, the reference antenna is assumed to be survey-grade and static. Further details of the simulation study's procedure are found in Appendix 3.12.2.

3.8.2 ASR Sensitivity to Antenna Quality

The simulation study considered survey- and smartphone-grade rover antennas, with the α values shown in Table 3.3. The corresponding $\sigma_{\phi,\mathrm{u}}$ values characterize the magnitude of the simulated multipath-induced errors on the DD phase measurements. Both reference and rover antennas were assumed to be static for the study of ASR dependence on antenna quality. The results given in Fig. 3.14 show that the measured ASR (dark traces) closely track the upper and lower bounds (dashed traces) for each antenna type and that antenna quality strongly influences ASR, with the survey-grade antenna having a 90% TAR—the time required to reach an ASR exceeding 0.9—more than 10 times shorter than the smartphone-grade antenna.

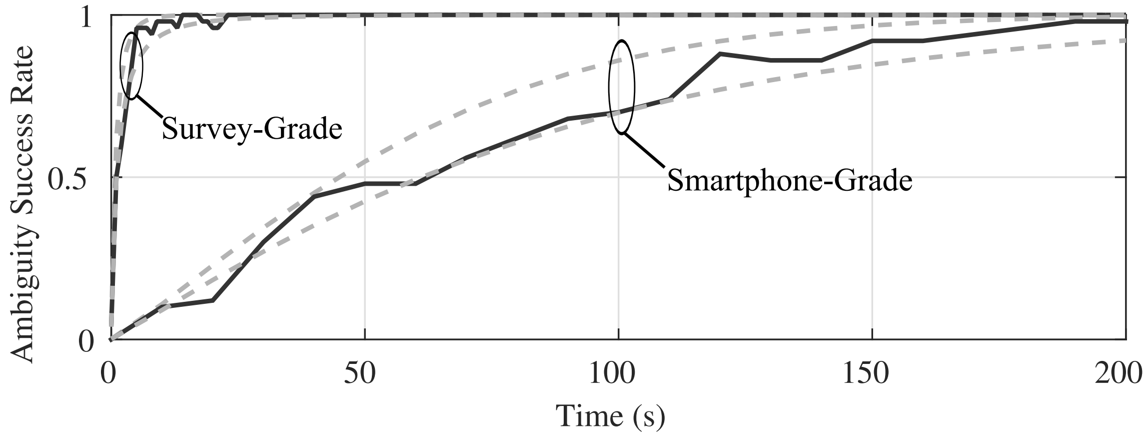

Figure 3.14: ASR as a function of the total measurement time for two antenna grades: smartphone- and survey-grade. The dark solid traces denote the empirical estimate of ASR, obtained via Monte Carlo analysis, while the lighter dashed traces denote the analytically computed upper and lower bounds of ASR.

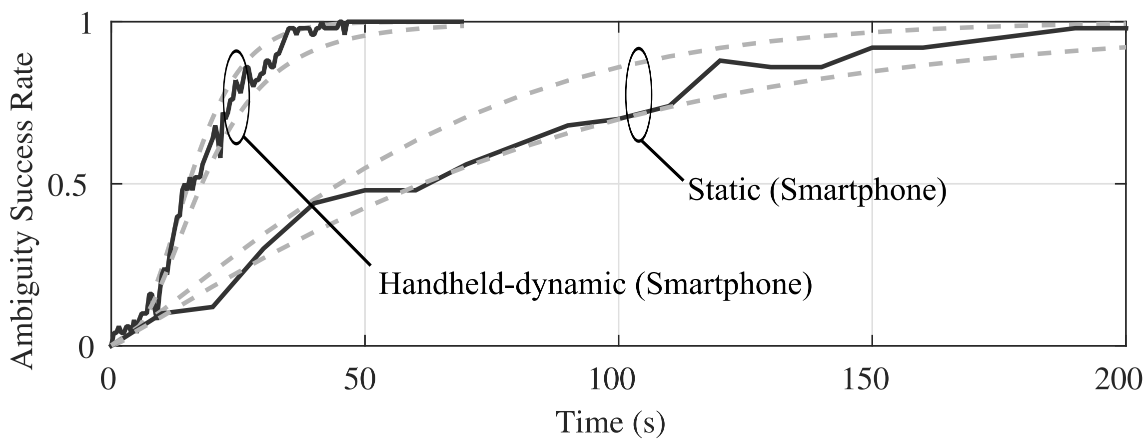

Figure 3.15: ASR as a function of the total measurement time for a smartphone-grade rover antenna in two different dynamics scenarios. The dark solid traces denote the empirical estimate of ASR, obtained via Monte-Carlo simulation and analysis, while the lighter dashed traces denote the analytically computed upper and lower bounds of ASR.

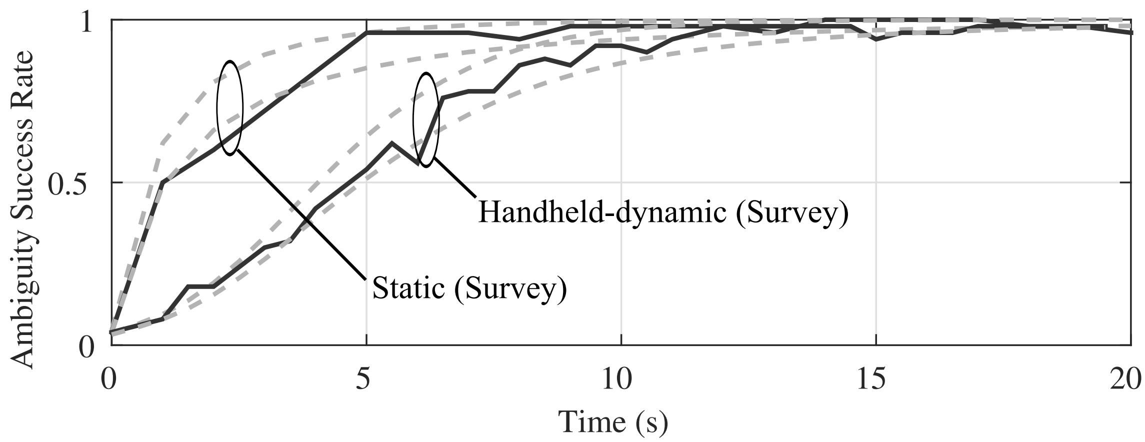

Figure 3.16: As Fig. 3.15 but for a survey-grade rover antenna. Note the shorter time interval as compared to Fig. 3.15.

3.8.3 ASR Sensitivity to Antenna Dynamics

The simulation study considered two rover antenna dynamics scenarios, static and gentle wavelength-scale random motion, labeled dynamic in Table 3.3. The $\{\tau_{\mathrm{p}},\sigma_{\mathrm{p}}\}$ pairs for each scenario were mapped to $\tau_{\phi,\mathrm{u}}$ values characterizing the correlation time of the simulated multipath-induced errors on the DD phase measurements using the model from Sec. 3.7. Figs. 3.15 and 3.16 show the results for the smartphone- and survey-grade rover antennas, respectively.

For the smartphone antenna, antenna motion significantly reduces TAR. In this case, the information gained by more rapid phase decorrelation exceeded the information lost by not having a tight antenna position constraint. Comparison of Figs. 3.15 and 3.14 reveals that a moving smartphone-grade antenna can rival the TAR of a static survey-grade antenna. This is a significant result: it indicates that centimeter-accurate CDGNSS positioning on mass-market receivers can be made practically rapid. The result also holds, with even better TAR, for the next highest grade above smartphone-grade antennas, the low-quality patch antenna described in [36], though the static-to-dynamic improvement is not so drastic. The result is

Table 3.4: Model Parameters for Empirical Study of ASR

	Rover				Reference	
	τ_{p} (sec)	σ_{p} (cycles)	$\tau_{\phi,\text{B}}$ (sec)	$\sigma_{\phi,\text{B}}$ (mm)	$\tau_{\phi,\text{A}}$ (sec)	$\sigma_{\phi,\text{A}}$ (mm)
Static	n/a	0	300	6	100	2.5
Dynamic	1	1	0.01	6	100	2.5

confirmed with real data in Sec. 3.9.

Interestingly, Fig. 3.16 reveals that motion lengthens TAR for a survey-grade rover antenna. It remains true that the phase measurement errors decorrelate more rapidly when the survey-grade antenna is moved, but because the magnitude of the phase errors is already so small, the information gained from faster phase error decorrelation does not compensate for the loss in information due to the added uncertainty (lack of constraint) in the motion model.

3.9 ASR Analysis using Real Data

This section provides a demonstration using real data of the improvement to ASR that comes from motion for low-cost antennas.

3.9.1 Data Collection and Alignment

Raw digitized intermediate-frequency (IF) GPS L1 C/A data were collected simultaneously by two receivers, a reference and a rover. The reference antenna was a survey-grade Trimble Zephyr and the rover antenna was a low-cost Taoglas patch. 5000 seconds of static rover data were collected, followed immediately by

900 seconds of dynamic rover data. During the dynamic dataset the rover antenna was moved in a random, wavelength-scale, three-dimensional pattern while held in the hand of an otherwise stationary user. The 3-dimensional motion profile of the rover antenna can be approximately modeled as an OU process with the values for τ_{p} and σ_{p} found in the bottom row of Table 3.4. The reference antenna remained stationary throughout data collection.

Each receiver ran a version of the GRID software-defined GNSS receiver [79], which processed the raw IF data and produced undifferenced code- and carrier-phase measurements. Each receiver's clock offset from GPS time was calculated at each measurement epoch from code phase measurements, enabling the carrier phase time histories to be timestamped in a common time base to approximately 15 ns accuracy. The rover's phase measurements were then interpolated to the time instants of the reference's measurements and the time histories were differenced according to (4.17) to form 7 DD carrier-phase time histories from the 8 highest elevation GPS satellites overhead at the time of the recording.

3.9.2 Phase Error Characterization

The carrier phase time histories produced from the recorded data exhibited errors whose statistics are summarized in Table 3.4 as $\{\tau_{\phi,\mathrm{B}}, \sigma_{\phi,\mathrm{B}}\}$ and $\{\tau_{\phi,\mathrm{A}}, \sigma_{\phi,\mathrm{A}}\}$ for the rover and reference antennas, respectively. These values were computed empirically from the DD residuals produced by CDGNSS batch processing over the full static and dynamic datasets. One exception is the value $\tau_{\phi,\mathrm{B}} = 0.01$ s for the dynamic dataset which, to avoid inaccuracy due to quantization effects, was calculated from the motion statistics τ_{p} and σ_{p} via the model in Sec. 3.7.3. The time correlation $\tau_{\phi,\mathrm{A}}$ is shorter than $\tau_{\phi,\mathrm{B}}$ because the reference antenna was further from reflecting surfaces than the rover antenna.

3.9.3 Data Processing

The DD carrier-phase time histories were split into 20 150-second and 12 65-second non-overlapping batches for the static and dynamic data sets, respectively. Each batch was provided separately to the CDGNSS estimator for processing along with the antenna motion and phase error statistics outlined in Table 3.4. For each batch, the estimator output the following at each measurement epoch k (on the basis of the measurements ingested from epoch 0 to k): (1) an estimate of the integer-valued state $\hat{\mathbf{n}}_k$, and (2) the square-root information matrix $\mathbf{R}_{\mathrm{nn}k}$ denoting the filter's confidence in this integer-valued state estimate. Using these, empirical ASR and analytical ASR bounds were computed as described in Appendix 3.12.2.

3.9.4 Results

Fig. 3.17 plots ASR estimates and bounds as a function of measurement time for the two rover antenna dynamics scenarios characterized by the motion and phase error statistics in Table 3.4. It is apparent that ASR performance improved with rover antenna motion; the time for ASR to reach 0.9, i.e., the 90% TAR, was reduced by over 50% for the dynamic vs. the static scenario.

3.10 Ambiguity Resolution with a Provided Motion Profile

Previous sections have established that for low-quality antennas, antenna motion reduces TAR. In this case, the tradeoff between loss of information due to lack of a motion constraint and gain in information from more quickly decorrelating phase measurement errors favors motion. But if the moving antenna's precise motion profile were somehow provided to the estimator, there would be no tradeoff: the receiver would enjoy the more rapid error decorrelation without losing the motion

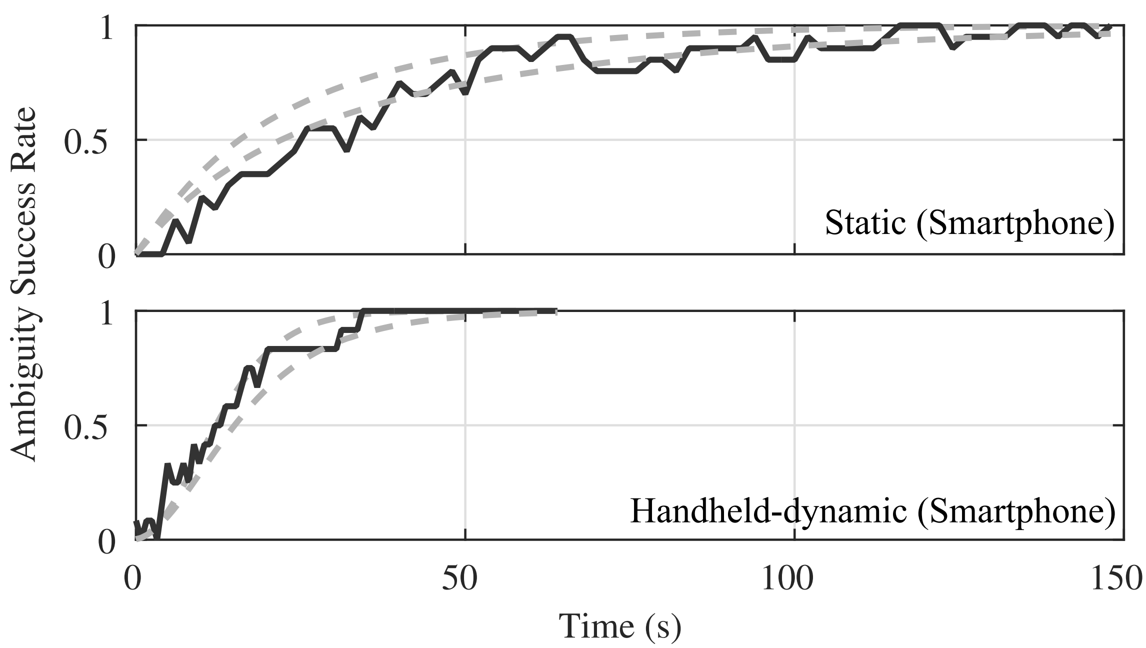

Figure 3.17: ASR as a function of measurement time for two different antenna dynamics scenarios. The dark solid traces denote the empirical estimate of ASR, obtained from analysis of many disjoint real data intervals, while the lighter dashed traces denote the upper and lower ASR bounds, computed analytically based on the $\mathbf{R}_{\mathrm{nn}k}$ matrix.

constraint. Such a motion profile could be approximated from inertial sensors or from processing of images captured by a camera attached to the receiver, as in [37]. The profile may only be known to within a translation, rotation, or scale factor. In the limit of an error-free motion profile known to within a translation, the motion constraint becomes as effective as a static constraint.

Motion-profile-aided ambiguity resolution with inertially-derived trajectories has been shown to reduce the ambiguity search volume [120], but this earlier work did not characterize improvement in terms of TAR nor attempt demonstration with real data. Known motion profiles have also been used for multipath mitigation, whether to enable estimation of multipath parameters [102] or synthetic aperture processing [94]. The current chapter's approach, described below, is similar to that of [94] except that it operates on the usual carrier phase observables instead of coherently processing the low-level correlation products.

3.10.1 Augmenting the CDGNSS Estimator with a Motion Profile

An *a priori* motion profile is incorporated into the CDGNSS estimator by augmenting the rover antenna relative position model of (3.4):

$$\mathbf{r}_k = \mathbf{r}_{\mathrm{C}} + \sum_{i=1}^{k} \mathbf{u}_i + \sum_{i=1}^{k} f^{k-i} \sqrt{1 - f^2} \mathbf{v}_i \tag{3.35}$$

where $\mathbf{u}_i$ is a 3×1 vector of the change in antenna position from t_{i-1} to t_i. Collectively, $\mathbf{u}_i$ for $i = 1, 2, \ldots, k$ form the *a priori* antenna motion profile. The real-valued state components $\mathbf{v}_i$ for $i = 1, 2, \ldots, k$ now model the changes to $\mathbf{r}_k$ from t_{i-1} to t_i not already captured by the *a priori* motion profile. Thus, the per-dimension standard deviation of $\mathbf{v}_i$, denoted σ_{p}, now models the uncertainty of $\mathbf{u}_i$ for $i = 1, 2, \ldots, k$.

Incorporating the augmented kinematic model of (3.35) into the batch estimator's measurement model results in the following augmented measurement model:

$$\mathbf{Y}_k - \mathbf{G}_k\mathbf{U}_k = \mathbf{H}_{\mathrm{x}k}\mathbf{C}_k\mathbf{x}_k + \mathbf{H}_{\mathrm{n}k}\mathbf{n}_k + \mathbf{W}_k \tag{3.36}$$

where

$$\mathbf{U}_k \triangleq \begin{bmatrix} \mathbf{u}_1 \\ \mathbf{u}_2 \\ \vdots \\ \mathbf{u}_k \end{bmatrix} \tag{3.37}$$

is a $3k \times 1$ vector containing the *a priori* knowledge of the change in antenna position from t_{i-1} to t_i for $i = 1, 2, \ldots, k$ and

$$\mathbf{G}_k = \begin{bmatrix} \mathbf{H}_{\mathrm{AB},1} & \mathbf{0} & \ldots & \mathbf{0} \\ \mathbf{H}_{\mathrm{AB},2} & \mathbf{H}_{\mathrm{AB},2} & \ddots & \vdots \\ \vdots & \vdots & \ddots & \mathbf{0} \\ \mathbf{H}_{\mathrm{AB},k} & \mathbf{H}_{\mathrm{AB},k} & & \mathbf{H}_{\mathrm{AB},k} \end{bmatrix} \tag{3.38}$$

is the time-dependent lower-triangular measurement sensitivity matrix for $\mathbf{U}_k$.

3.10.2 Applying a Motion Profile to Real Data

An analysis of the TAR improvement offered by an *a priori* motion profile was performed with real data. The motion profile was obtained and was applied within the estimator as follows:

1. The absolute rover antenna three-dimensional trajectory was computed by performing a CDGNSS solution on the basis of the entire 900 second batch of dynamic data mentioned previously using phase measurements from all 12 satellites overhead at the time of the recording.

2. An unknown three-dimensional translation was added to the computed trajectory to obtain a translation-ambiguous motion profile. Such a translation ambiguity would also be present in a motion profile obtained using an inertial or vision system.

3. This motion profile was provided to the CDGNSS estimator in the form epoch-by-epoch antenna position changes, as the quantities $\mathbf{u}_i$, for $i \ldots k$ in (3.35). These vectors were stacked into a $3k \times 1$ vector $\mathbf{U}_k$ and integrated into the estimator's measurement model as in (3.36).

4. The assumed accuracy of the motion profile can be conveyed to the estimator through the statistics of the unknown receiver position, i.e., σ_p and τ_p. As the limiting case of a noise-free profile was most interesting for the current chapter, it was assumed that $\sigma_\mathrm{p} = 0$ and $\tau_\mathrm{p} = \infty$.

3.10.3 Results

Fig. 3.18 shows that, for the data set studied, which is typical, motion profile aiding reduced the empirical 90% TAR by approximately 30%. The dark solid trace in the lower panel hangs below the ASR bounds because the motion profile was not, in fact, error free as the estimator was configured to assume. The bounds predict a reduction in 90% TAR for the error-free case of slightly more than 30%. Other tests revealed that the percent by which motion profile aiding improves TAR increases when there are fewer satellite signals available, i.e., when the initialization scenario is more challenging.

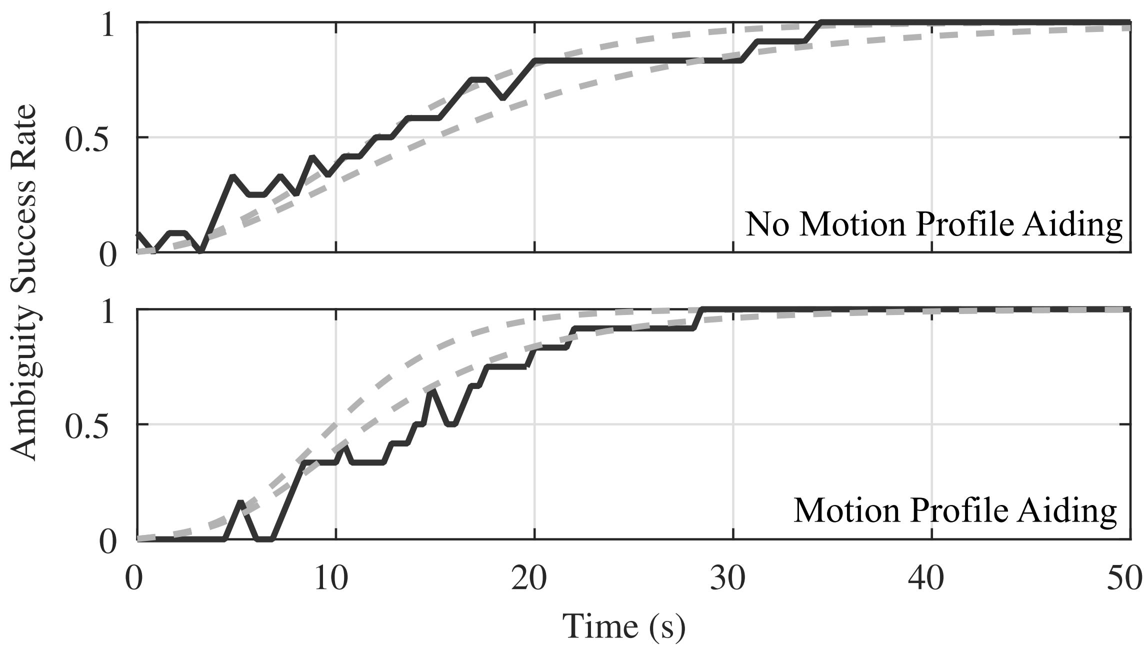

Figure 3.18: ASR as a function of the total measurement time for a dynamic scenario without (top panel) and with (bottom panel) motion profile aiding. The dark solid traces denote the empirical estimate of ASR, while the lighter dashed traces denote the analytically-computed ASR upper and lower bounds.

3.11 Conclusions

Using both simulated and empirical data it was shown that wavelength-scale random antenna motion is an effective strategy for significantly speeding integer ambiguity resolution when performing a CDGNSS solution using a low-cost GNSS antenna. Empirical resolution time was reduced by over 50% when the antenna was moved as compared to static. It was further shown that if *a priori* knowledge of the antenna's motion profile is available, such a constraint further reduces resolution time: an additional 30% reduction was shown for an empirical scenario in which a mm-accurate motion profile was known to within a translation. These results are significant: they portend an expansion of CDGNSS positioning into the mass market, where low-cost, low-quality antennas are abundant and CDGNSS initialization time is seen as a primary limiting factor.

3.12 Appendix

3.12.1 Multipath Simulation Study

This section describes the Monte-Carlo-type simulation study performed to approximate the statistical relationship between phase errors and antenna quality and dynamics.

1. A 200-second one-dimensional antenna position trajectory was simulated at 100 Hz with variations modeling an Ornstein-Uhlenbeck process characterized by a fixed standard deviation σ_{p} and correlation time τ_{p}. Only one dimension needs to be simulated because a three-dimensional antenna reference frame can always be rotated to align one dimension parallel to the direction of the reflected signal, making phase errors largely unaffected by positional variations in the other two dimensions.

2. The simulated one-dimensional positional variations (assumed aligned with direction of the reflected signal) are assumed equivalent to variations in the term $d_{\mathrm{ref}} - d_{\mathrm{los}}$ in (3.34). These positional variations can then be converted into a phase difference time history using (3.34).

3. 10 initial phase offsets, evenly spaced between 0 and 2π, are added to the simulated phase difference time history to generate 10 phase difference time histories. This guarantees that the phase difference means over all 10 time histories are evenly distributed between 0 and 2π, appropriately modeling real-world scenarios.

4. Each of the 10 phase difference time histories is converted to a phase measurement error time history using (3.33), assuming a constant α.

5. The standard deviation $\sigma_{\phi,\mathrm{u}}$ and correlation time $\tau_{\phi,\mathrm{u}}$ are computed for each of the simulated 200-second phase error time histories. These values are then averaged across all 10 time histories and stored.

6. Simulation input parameters, σ_{p}, τ_{p}, and α are modified and steps (1)–(5) are repeated to obtain averaged $\sigma_{\phi,\mathrm{u}}$ and $\tau_{\phi,\mathrm{u}}$ terms on the basis of these new values. The range of input parameter values over which data were simulated and averaged $\sigma_{\phi,\mathrm{u}}$ and $\tau_{\phi,\mathrm{u}}$ values were computed is listed in Table 3.5.

3.12.2 Details of Simulation Study of ASR

This section describes the details of the simulation study employed to determine the sensitivity of ASR to antenna quality and antenna dynamics.

Table 3.5: Range of σ_{p}, τ_{p}, and α over which data were simulated

Characteristic	Range
Antenna Quality	$0.1 \leq \alpha \leq 1$
Antenna Motion Correlation Time (s)	$0 \leq \tau_{\mathrm{p}} \leq 10$
Antenna Motion Standard Deviation (cycles)	$0.5 \leq \sigma_{\mathrm{p}} \leq 4$

3.12.2.1 Data Simulation

Carrier phase measurements are simulated as would be received by an antenna located on roof of the W.R. Woolrich building in Austin, Texas during a 6 hour period of the early morning hours of December 14, 2014. These simulated measurements properly account for satellite motion, receiver motion, and phase measurement error.

The position of each satellite tracked is computed in the Earth-Centered Earth-Fixed (ECEF) reference frame for each time epoch, using the broadcast satellite ephemerides. The simulated rover antenna trajectory conforms to either a static or a dynamic scenario as modeled by an Ornstein Uhlenbeck process with parameters outlined in Table 3.3. The reference antenna is taken to be static. Once satellite and receiver positions are determined for all desired time epochs, the true range from the rover and reference antennas to each satellite is computed at each epoch, resulting in error-free undifferenced carrier phase measurement time-histories.

Phase error time histories are simulated according to an Ornstein Uhlenbeck process characterized by a value of $\sigma_{\phi,\mathrm{u}}$ corresponding to a particular antenna quality and a value of $\tau_{\phi,\mathrm{u}}$ antenna-motion–phase-noise corresponding to particular antenna dynamics. Table 3.3 lists $\sigma_{\phi,\mathrm{u}}$ values corresponding to the two antenna qualities to be tested, a survey-grade antenna and a smartphone-grade antenna, and $\tau_{\phi,\mathrm{u}}$ values corresponding to the two antenna dynamics scenarios to be tested, a static and a dynamic scenario. The $\sigma_{\phi,\mathrm{u}}$ values were deduced empirically from thousands of seconds of data collected from both antenna types while the antenna was static and the $\tau_{\phi,\mathrm{u}}$ values were deduced, for the static scenario, from earlier work by others [87], and for the dynamic scenario, from the antenna-motion–phase-error relationship detailed in Fig. 3.13 using the antenna motion statistics of Table 3.3.

Once simulated, these phase error time histories are added to previously simulated error-free carrier phase measurement time-histories to produce high-fidelity undifferenced carrier phase measurement time histories. Note that other commons sources of error such as atmospheric- and clock-induced errors are not simulated as they are assumed to be cancelled out during the subsequent double-differencing operation.

3.12.2.2 Processing and Analysis

For each scenario, data are simulated as above, passed through the CDGNSS estimator, and the outputs of the estimator are used to compute ASR a function of the total measurement duration t and one of either varying antenna quality or antenna dynamics, depending on the scenario under test. All other parameters are held constant. In particular, for each scenario, the test procedure will be to:

1. Fix the time between subsequent measurement epochs to 0.5 seconds for the dynamic antenna scenario and 10 seconds for the static antenna scenario.

2. Fix the number of satellites used in the CDGNSS solution M_k to 8.

3. Fix the rover antenna quality to be of smartphone-grade and the dynamics to be static when not being varied.

4. Fix the reference antenna to be stationary and of survey-grade quality throughout.

5. Simulate 50 non-overlapping 200 second batches of undifferenced carrier phase measurements according to the desired motion and phase error statistics detailed in Table 3.3.

6. Double difference the simulated undifferenced phase measurements according to (4.17), resulting in 50 DD batches.

7. Feed each DD batch, one at a time, into the CDGNSS estimator. For each batch, compute a CDGNSS solution on the basis epochs 0 through l, where $0 \leq l \leq k$. Increase l by 1, computing a new CDGNSS solution after each increase.

8. After each CDGNSS solution, compute (1) an empirical estimate of ASR, (2) an ADOP-based estimate of ASR (see [118, 119]), and (3) a covariance-based analytical upper and lower bound of ASR. The empirical ASR was computed via Monte-Carlo simulation from the 50 batches of simulated DD phase data, as follows:

   (a) For each time epoch k, the estimator computes an estimate of the integer-valued ambiguities $\hat{\mathbf{n}}_k$ on the basis of the data ingested from time 0 to k.

   (b) The integer estimates $\hat{\mathbf{n}}_k$, for $k = 1, 2, \ldots,$ are compared against the true vector of integer ambiguities $\mathbf{n}$. For each k, if $\hat{\mathbf{n}}_k$ matches $\mathbf{n}$, a flag is set at time t_k to "1"; if incorrect, the flag is set to "0".

   (c) At each t_k, the flags produced in step 2 are averaged across 50 batches to generate an empirical ASR value at each time epoch.

The lower and upper bounds on ASR were computed analytically at each epoch using the estimator-produced integer-state information matrix $\mathbf{R}_{\mathrm{nn}k}$; refer to section IV of [33] for details on computing these bounds.

Chapter 4

VISRTK: A Framework for Fast, Accurate, and Robust Smartphone Pose Determination

This chapter presents and analyzes an estimation framework that combines monocular camera images with GNSS carrier phase measurements for fast, robust, precise, and globally-referenced mobile device position and orientation (pose) determination. The framework, which will be termed VISRTK after the common industry synonym for CDGNSS, Real Time Kinematic (RTK), augments the bundle-adjustment- (BA-)-based structure from motion (SFM) algorithm with carrier phase differential GNSS (CDGNSS) algorithm in a way that preserves both the sparseness of the Jacobian matrix in BA and the integer structure of the ambiguities in CDGNSS. In doing so, the proposed fused framework is able to exploit the computational efficiency of BA and the precision of CDGNSS to efficiently and accurately determine the pose of the mobile device in a global reference frame. Comparisons to existing approaches which combine GNSS and camera measurements for globally-referenced pose determination reveal that these do not combine measurements as tightly nor optimally as the proposed approach, resulting in the proposed approach having a faster, more robust, and more accurate solution. Empirical simulation results and results using real data in the form of images and GNSS carrier phase measurements captured from a low-cost GNSS receiver and smartphone platform show that the proposed estimation framework (1) achieves centimeter- and sub-degree-accurate pose estimates, (2) leads to faster resolution of the CDGNSS integer ambiguities as compared to standalone CDGNSS, and (3) is able to use prior information from previously-localized point features for instantaneous CDGNSS integer-ambiguity resolution.

4.1 Introduction

The need for centimeter- and sub-degree-accurate device position and orientation (together known as "pose") is present in many applications, including, but not limited to, surveying, photogrammetry, semi-autonomous and autonomous driving, and augmented and virtual reality. However, obtaining such accuracy has so-far been costly, particularly for consumer mass-market applications. Current solutions require either GPS-aided inertial navigation systems (INS) or motion-capture systems costing in the thousands of dollars [121–123].

The wide adoption of smartphones has resulted in rapid accuracy improvements to and a reduction in cost of microelectromechanical systems (MEMS) inertial sensors, GNSS chips, and camera technology, all of which are embedded sensors inside these devices. Over the past decade, many researchers have studied the viability of these smartphone sensors for precise pose determination. Research in coupling a smartphone-grade inertial measurement unit (IMU), magnetometer, and GNSS receiver has shown orientation accuracies of around 1–2 degrees and positional accuracies of a few meters [121, 124, 125] during continuous GNSS tracking. However, in the absence of continuous GPS measurements the accuracy degrades to a few degrees and many tens of meters in a matter of seconds [121, 124]. Despite these improvements, these pose accuracies—even with continuous tracking—are not good enough for many applications, including surveying and virtual reality.

Recent work by the authors has investigated ways to improve the pose accuracy of low-cost platforms to less than a decimeter in position and a degree in orientation, while also maintaining a slow degradation in accuracy in the event of a GNSS outage. In particular, [2] has shown that centimeter-accurate position estimation is possible with a smartphone antenna and software-based GNSS receiver, while [126] has shown in simulation that coupling this technology with image measurements can facilitate sub-degree orientation as well.

Over the base 20 years, researchers in the computer vision, estimation, and mathematical communities have developed a great body of literature in the areas of photogrammetry, structure from motion (SFM), multiple view geometry, and visual simultaneous localization and mapping algorithm (SLAM) [127–130]. All of these research areas describe a similar topic approached from multiple starting disciplines by which the end goal is to locate a receiver or map its surroundings using vision, and, in some cases, coupling vision measurements with other sensors. The current work builds on this great body of literature by combining these techniques with a centimeter-accurate positioning technique from the navigation community known as Real Time Kinematic (RTK) or carrier phase differential GNSS (CDGNSS).

Researchers in the computer vision community have developed a BA-based SLAM algorithm capable of running in real-time on a smartphone processor [131]. The resulting accuracies are sub-degree accurate, although the resulting pose estimates contain scale, rotational, and translational ambiguities which prevent it from being globally referenced.

Other prior work in the computer vision community combines GNSS and image measurements to get globally referenced pose. However, this combination is done in the most decoupled manner possible—by computing a least-squares solution between the (1) GPS and (2) BA-based camera trajectories to solve for the scale, rotational, and translational ambiguities needed to bring the BA-based trajectory into a global reference frame. Unfortunately, this approach—which will be subsequently referred to as the Horn transform—does not enable the optimal sharing of GNSS and image measurement information. Relative errors in the BA trajectory, for instance, will remain in the final solution, albeit now in a globally-referenced frame.

The prior work by the current authors outlined in [32, 126] showed that the centimeter-accurate carrier-phase differential GNSS (CDGNSS) positioning algorithm can be fused in a with BA in a loosely-coupled manner (although more tightly-coupled then the horn-transform method) to produce centimeter-accurate position and sub-degree accurate device orientation [32, 126]. However, this work (1) used external, high-cost GNSS and camera sensors and (2) did not fuse the measurements as optimally as the proposed approach, and (3) only offered a simulation study of the results. This loosely-coupled approach, for instance, does not enable the vision measurements to aid in resolving the CDGNSS ambiguities needed before a centimeter-accurate position trajectory can be determined.

In contrast to the prior work by the authors and others, the current chapter proposes combining GNSS and smartphone camera measurements in the most optimal manner yet for absolute pose determination. In contrast to previous work, the current approach is a tightly-coupled fusion of the CDGNSS and bundle-adjustment (BA) algorithms. As such, this approach is faster, in that it can resolve the CDGNSS ambiguities faster that standalone CDGNSS, and more accurate, it that it enables vision measurements to aid in detecting and minimizing the effects of carrier phase outlier and cycle slips. It is also more elegant while being no more computationally demanding than the approach of [126]. Finally, it enables prior information regarding the position of point features computed earlier to be easily integrated with current GNSS phase and point feature measurements to compute a pose estimate much more rapidly than could be achieved on the basis of current measurements alone. Such prior information then enables the current CDGNSS ambiguities to be resolved almost instantaneously, a technique by which we will term Jumpstart VISRTK.

4.2 VISRTK Batch Estimator

The VISRTK batch estimator takes as its input double-differenced (DD) carrier phase measurements made between two GNSS receivers, a reference and a rover and image feature measurements and processes these, together with any prior information on the point feature locations, to estimate (1) the camera position and orientation at each measurement epoch and (2) a vector of carrier-phase integer ambiguities. The estimator will preserve and exploit the sparse structure of the Jacobian matrix, as is typically done in vision-only Bundle Adjustment [132], for a computationally efficient result, while using the Least-Squares Ambiguity Decorrelation Adjustment (LAMBDA) [15] and corresponding search function to solve for the integer ambiguities and lock them in prior to solving for the rest of the state, thus improving the ultimate accuracy of their estimates.

4.2.1 State

The estimator's state is as follows:

$$\mathbf{X}_{\mathrm{BA}} = \begin{bmatrix} \mathbf{X}_{\mathcal{C}} \\ \mathbf{N} \\ \mathbf{X}_{\mathcal{P}} \end{bmatrix} \tag{4.1}$$

where

$\mathbf{X}_{\mathcal{C}}$ is a $6L \times 1$ vector modeling the position and attitude of the camera at each pose (expanded below), where L is the total number of poses,

$\mathbf{N}$ is a $P \times 1$ integer-valued vector of carrier phase ambiguities (expanded below), where $P+1$ is the total number of GNSS signals tracked (the "+1" denotes the reference signal), and

$\mathbf{X}_{\mathcal{P}}$ is a $3M \times 1$ vector modeling the feature point positions (expanded below), where M is the total number of feature points.

$\mathbf{X}_{\mathcal{C}}$, $\mathbf{N}$, and $\mathbf{X}_{\mathcal{P}}$ can be expanded as

$$\begin{aligned}
\mathbf{X}_{\mathcal{C}} &= \left[\left(\mathbf{x}_{\mathcal{G}}^{\mathcal{C}_1}\right)^T \quad x\left(\mathbf{q}_{\mathcal{G}}^{\mathcal{C}_1}\right)^T \quad \ldots \quad \left(\mathbf{x}_{\mathcal{G}}^{\mathcal{C}_L}\right)^T \quad \left(\mathbf{q}_{\mathcal{G}}^{\mathcal{C}_L}\right)^T \right]^T \\
\mathbf{N} &= \left[N^1 \quad N^2 \quad \ldots \quad N^P \right]^T \\
\mathbf{X}_{\mathcal{P}} &= \left[\left(\mathbf{x}_{\mathcal{G}}^{\mathcal{P}_1}\right)^T \quad \left(\mathbf{x}_{\mathcal{G}}^{\mathcal{P}_2}\right)^T \quad \ldots \quad \left(\mathbf{x}_{\mathcal{G}}^{\mathcal{P}_M}\right)^T \right]^T
\end{aligned} \tag{4.2}$$

where

$\mathbf{x}_{\mathcal{G}}^{\mathcal{C}_i}$ is a 3×1 vector modeling the position of the camera at pose i, $i = 1, 2 \ldots, L$, in the global earth-centered-earth-fixed (ECEF) coordinate system,

$\mathbf{q}_{\mathcal{G}}^{\mathcal{C}_i}$ is a 3×1 quaternion vector representation of the attitude of the camera at pose i, $i = 1, 2 \ldots, L$, in the global earth-centered-earth-fixed (ECEF) coordinate system,

N^k is the integer-valued phase ambiguity for the k^{th} satellite pair, $k = 1, 2 \ldots, P$, assumed constant so long as both the reference and rover GNSS receivers retain phase lock on the signals tracked, and

$\mathbf{x}_{\mathcal{G}}^{\mathcal{P}_j}$ is a 3×1 vector modeling the position of the j^{th} point feature, $j = 1, 2 \ldots, M$, in the global earth-centered-earth-fixed (ECEF) coordinate system.

4.2.2 Measurement Models

The batch estimator's measurement model relates the point feature and GNSS carrier-phase measurements to the state.

4.2.2.1 Point Feature Measurement Model

The measurement of the j^{th} point feature taken at pose i is modeled as

$$\mathbf{y}_i^{\mathrm{p}_j} = \mathbf{h}_y\left(\mathbf{x}_{\mathcal{C}_i}^{p_j}\right) + \mathbf{w}_i^{p_j} = \begin{bmatrix} \frac{x_{\mathcal{C}_i}^{p_j}}{z_{\mathcal{C}_i}^{p_j}} & \frac{y_{\mathcal{C}_i}^{p_j}}{z_{\mathcal{C}_i}^{p_j}} \end{bmatrix}^T + \mathbf{w}_i^{p_j} \tag{4.3}$$

where $\mathbf{h}_s(\cdot)$ is the non-linear perspective projection measurement model, relating the 2×1 point feature measurement $\mathbf{y}_i^{\mathrm{p}_j}$ to the 3×1 position of the j^{th} point feature referenced to the i^{th} the camera frame $\mathbf{x}_{\mathcal{C}_i}^{p_j}$. $\mathbf{w}_i^{p_j}$ is zero-mean Gaussian white noise. $\mathbf{x}_{\mathcal{C}_i}^{p_j}$ is related to the state variables through the equation:

$$\mathbf{x}_{\mathcal{C}}^{p_j} = \begin{bmatrix} x_{\mathcal{C}}^{p_j} \\ y_{\mathcal{C}}^{p_j} \\ z_{\mathcal{C}}^{p_j} \end{bmatrix} = \left(R\left(\mathbf{q}_{\mathcal{G}}^{\mathcal{C}}\right)\right)^T \left(\mathbf{x}_{\mathcal{G}}^{p_j} - \mathbf{x}_{\mathcal{G}}^{\mathcal{C}}\right) \tag{4.4}$$

where $R(\cdot)$ is the 3×3 rotation-matrix-representation of the camera attitude defined by $\mathbf{q}_{\mathcal{G}}^{\mathcal{C}}$. As described in [126], it is assumed that a calibrated camera is used and that any distortion caused by the lens is removed by passing the raw measurements through the inverted distortion model prior to passing the measurements to the estimators. This enables the distortion-free point feature measurements to be aptly described by the pinhole-type prospective projection model of (4.3).

The non-linear point feature measurement model of (4.3) can be linearized with respect to the state to form the following linearized measurement model

$$\mathbf{y}_i^{\mathrm{p}_j} \approx \mathbf{h}_y\left(\bar{\mathbf{x}}_{\mathcal{G}}^{\mathcal{C}_i}, \bar{\mathbf{q}}_{\mathcal{G}}^{\mathcal{C}_i}, \bar{\mathbf{x}}_{\mathcal{G}}^{p_j}\right) + H_i^j|_{\bar{\mathbf{x}}_{\mathrm{BA}}} \Delta\mathbf{X}_{\mathrm{BA}} + \mathbf{w}_i^{p_j} \tag{4.5}$$

where

$$H_i^j|_{\bar{\mathbf{x}}_{\mathrm{BA}}} = \frac{\partial \mathbf{h}_y}{\partial \mathbf{X}_{\mathrm{BA}}} \tag{4.6}$$

$$= \left[0, \ldots, 0, \frac{\partial \mathbf{h}_y}{\partial \mathbf{x}_{\mathcal{G}}^{\mathcal{C}_i}}, \frac{\partial \mathbf{h}_y}{\partial \delta \mathbf{e}_{\mathcal{G}}^{\mathcal{C}_i}}, 0, \ldots, 0, \frac{\partial \mathbf{h}_y}{\partial \mathbf{x}_{\mathcal{G}}^{\mathcal{P}_j}}, 0, \ldots, 0\right]\Bigg|_{\bar{\mathbf{x}}_{\mathrm{BA}}} \tag{4.7}$$

is the $1 \times (6L + P + 3M)$ Jacobian matrix, $\delta \mathbf{e}_{\mathcal{G}}^{\mathcal{C}_i}$ is the 3×1 minimal attitude representation of the differential quaternion $\delta \mathbf{q}_{\mathcal{G}}^{\mathcal{C}_i}$ [126, 133]. As specified in [126], "differential quaternions represent a small rotation from the current attitude to give an updated estimate of the attitude through the equation

$$\mathbf{q}' = \delta \mathbf{q}(\delta \mathbf{e}) \otimes \mathbf{q} \tag{4.8}$$

where $\mathbf{q}'$ is the updated attitude estimate, $\otimes$ represents quaternion multiplication, and $\delta \mathbf{q}(\delta \mathbf{e})$ is the differential quaternion". $\frac{\partial \mathbf{h}_y}{\partial \mathbf{x}_{\mathcal{G}}^{\mathcal{C}_i}}$, $\frac{\partial \mathbf{h}_y}{\partial \delta \mathbf{e}_{\mathcal{G}}^{\mathcal{C}_i}}$, and $\frac{\partial \mathbf{h}_y}{\partial \mathbf{x}_{\mathcal{G}}^{\mathcal{P}_j}}$ are the partial derivatives of (4.3) with respect to the relevant state elements and can be expanded as:

$$\frac{\partial \mathbf{h}_y}{\partial \mathbf{x}_{\mathcal{G}}^{\mathcal{C}_i}} = \frac{\partial \mathbf{h}_y}{\partial \mathbf{x}_{\mathcal{C}}^{\mathcal{P}_j}} \frac{\partial \mathbf{x}_{\mathcal{C}}^{\mathcal{P}_j}}{\partial \mathbf{x}_{\mathcal{G}}^{\mathcal{C}_i}} \tag{4.9}$$

$$\frac{\partial \mathbf{h}_y}{\partial \delta \mathbf{e}_{\mathcal{G}}^{\mathcal{C}_i}} = \frac{\partial \mathbf{h}_y}{\partial \mathbf{x}_{\mathcal{C}}^{\mathcal{P}_j}} \frac{\partial \mathbf{x}_{\mathcal{C}}^{\mathcal{P}_j}}{\partial \delta \mathbf{e}_{\mathcal{G}}^{\mathcal{C}_i}} \tag{4.10}$$

$$\frac{\partial \mathbf{h}_y}{\partial \mathbf{x}_{\mathcal{G}}^{\mathcal{P}_j}} = \frac{\partial \mathbf{h}_y}{\partial \mathbf{x}_{\mathcal{C}}^{\mathcal{P}_j}} \frac{\partial \mathbf{x}_{\mathcal{C}}^{\mathcal{P}_j}}{\partial \mathbf{x}_{\mathcal{G}}^{\mathcal{P}_j}} \tag{4.11}$$

where

$$\left.\frac{\partial \mathbf{h}_y}{\partial \mathbf{x}_{\mathcal{C}}^{p_j}}\right|_{\bar{\mathbf{x}}} = \begin{bmatrix} \frac{1}{\bar{z}_{\mathcal{C}}^{p_j}} & 0 & \frac{-\bar{x}_{\mathcal{C}}^{p_j}}{\left(\bar{z}_{\mathcal{C}}^{p_j}\right)^2} \\ 0 & \frac{1}{\bar{z}_{\mathcal{C}}^{p_j}} & \frac{-\bar{y}_{\mathcal{C}}^{p_j}}{\left(\bar{z}_{\mathcal{C}}^{p_j}\right)^2} \end{bmatrix} \tag{4.12}$$

$$\left.\frac{\partial \mathbf{x}_{\mathcal{C}}^{\mathcal{P}_j}}{\partial \mathbf{x}_{\mathcal{G}}^{\mathcal{C}_i}}\right|_{\bar{\mathbf{x}}} = -\left(R\left(\bar{\mathbf{q}}_{\mathcal{G}}^{\mathcal{C}}\right)\right)^T \tag{4.13}$$

$$\left.\frac{\partial \mathbf{x}_{\mathcal{C}}^{\mathcal{P}_j}}{\partial \delta\mathbf{e}_{\mathcal{G}}^{\mathcal{C}_i}}\right|_{\bar{\mathbf{x}}} = -2\left(R\left(\bar{\mathbf{q}}_{\mathcal{G}}^{\mathcal{C}}\right)\right)^T \left[\left(\bar{\mathbf{x}}_{\mathcal{G}}^{p_j} - \bar{\mathbf{x}}_{\mathcal{G}}^{\mathcal{C}}\right)\times\right] \tag{4.14}$$

$$\left.\frac{\partial \mathbf{x}_{\mathcal{C}}^{\mathcal{P}_j}}{\partial \mathbf{x}_{\mathcal{G}}^{\mathcal{P}_j}}\right|_{\bar{\mathbf{x}}} = \left(R\left(\bar{\mathbf{q}}_{\mathcal{G}}^{\mathcal{C}}\right)\right)^T \tag{4.15}$$

where $[(\cdot)\times]$ represents the cross product equivalent matrix of the argument defined as [126]

$$[\mathbf{x}\times] = \begin{bmatrix} 0 & -x_3 & x_2 \\ x_3 & 0 & -x_1 \\ -x_2 & x_1 & 0 \end{bmatrix} \tag{4.16}$$

where x_i is the ith element of $\mathbf{x}$.

4.2.2.2 GNSS Carrier Phase Measurement Model

The DD GNSS carrier phase measurement of satellite pair k taken at the time of pose i, t_i, is modeled as

$$y_{\phi,i}^k \triangleq \left[\phi_{\mathrm{A},i}^{\mathrm{k}} - \phi_{\mathrm{A},i}^{1}\right] - \left[\phi_{\mathrm{B},i}^{\mathrm{k}} - \phi_{\mathrm{B},i}^{1}\right], \tag{4.17}$$

where

$\phi_{\alpha,i}^{\beta}$, $\alpha \in \{\mathrm{A},\mathrm{B}\}$, $\beta \in \{1,2,\ldots,P\}$, is the undifferenced carrier phase measurement at t_i between receiver α and satellite β. As seen, satellite 1 is the common reference satellite. $y_{\phi,i}^k$, which as units of meters, can be related to the camera position and integer ambiguity state elements $\mathbf{x}_{\mathcal{G}}^{\mathcal{C}_i}$ and N^k of (4.2) by the following nonlinear measurement model [57]:

$$y^k_{\phi,i} = h_\phi\left(\mathbf{x}^{\mathcal{C}_i}_{\mathcal{G}}, \mathbf{q}^{\mathcal{C}}_{\mathcal{G}}, N^k\right) + w^{\mathrm{j1}}_{\mathrm{AB},i} \tag{4.18}$$

$$= r^{\mathrm{k}}_{\mathrm{AB},i} + \lambda N^k + w^{\mathrm{k}}_{\mathrm{AB},i} \tag{4.19}$$

where

$$r^{\mathrm{k}}_{\mathrm{AB},i} \triangleq \left(r^{\mathrm{k}}_{\mathrm{A},i} - r^{1}_{\mathrm{A},i}\right) - \left(r^{\mathrm{k}}_{\mathrm{B},i} - r^{1}_{\mathrm{B},i}\right) \tag{4.20}$$

is the DD range between the two receivers and two satellites and

λ is the GNSS signal wavelength;

N^k is the integer ambiguity for the k^{th} satellite pair, as defined previously;

$w^{\mathrm{k}}_{\mathrm{AB},i}$ is the DD carrier phase measurement error at t_i;

$r^\beta_{\alpha,i} \triangleq \left\|\mathbf{x}^\beta_i - \mathbf{x}_{\alpha,i}\right\|$, $\alpha \in \{\mathrm{A},\mathrm{B}\}$, $\beta \in \{1, 2, \ldots, M_k\}$, is the range between receiver α and satellite β at t_i, where $\|\cdot\|$ represents the Euclidean norm; $r^\beta_{B,i}$ is expanded below to relate this range to the estimator state elements.

$r^\beta_{\mathrm{A},i} \triangleq \left\|\mathbf{x}^\beta_i - \mathbf{x}_{\alpha,i}\right\|$, $\beta \in \{1, 2, \ldots, P\}$, is the range between the antenna of reference receiver A and satellite β at t_i, where $\|\cdot\|$ represents the Euclidean norm;

$r^\beta_{\mathrm{B},i} \triangleq \left\|\mathbf{x}^\beta_i - \mathbf{x}_{\alpha,i}\right\| = \left\|\mathbf{x}^\beta_i - \left(\mathbf{x}^{\mathcal{C}_i}_{\mathcal{G}} + R\left(\mathbf{q}^{\mathcal{C}}_{\mathcal{G}}\right)\mathbf{x}^{\mathcal{A}_{\mathrm{B}}}_{\mathcal{C}}\right)\right\|$, $\beta \in \{1, 2, \ldots, P\}$, is the range between the antenna of mobile receiver B—the receiver attached to the camera—and satellite β at t_i.

$\mathbf{x}_{\alpha,i}$ is the 3×1 absolute position of the GNSS antenna of receiver $\alpha \in \{\mathrm{A},\mathrm{B}\}$ at the time of signal reception t_i, in the global coordinate frame; and

$\mathbf{x}^\beta_i$ is the 3×1 absolute position of satellite $\beta \in \{1, 2, \ldots, P\}$ at the time of signal transmission, in the global coordinate frame.

$\mathbf{x}_{\mathcal{C}}^{\mathcal{A}_{\mathrm{B}}}$ is the 3×1 position of receiver B's GNSS antenna in the camera coordinate frame, which is constant so long as the antenna and camera are rigidly connected to the same platform.

$r_{B,i}^{\beta}$ is the range between the antenna of mobile receiver B—the receiver attached to the camera—and satellite β at t_i. It can be related to the state elements through the following model

$$r_{B,i}^{\beta} \triangleq \left\| \mathbf{x}_i^{\beta} - \mathbf{x}_{B,i} \right\| \tag{4.21}$$

$$= \left\| \mathbf{x}_i^{\beta} - \left(\mathbf{x}_{\mathcal{G}}^{\mathcal{C}_i} + R\left(\mathbf{q}_{\mathcal{G}}^{\mathcal{C}}\right)\right) \mathbf{x}_{\mathcal{C}_i}^{\mathcal{A}} \right\|, \ \beta \in \{1, 2, \ldots, P\}, \tag{4.22}$$

where $\mathbf{x}_{\mathcal{C}_i}^{\mathcal{A}}$ is the fixed 3×1 position of receiver B's GNSS antenna in the $\mathcal{C}_i$ frame. This term is typically non-zero due to the physical offset between the GNSS antenna's phase center and the center of the camera lens.

The non-linear GNSS carrier phase measurement model of (4.18) can be linearized with respect to the state information to form the following linearized measurement model:

$$y_{\phi,i}^{k} \approx h_{\phi}\left(\bar{\mathbf{x}}_{\mathcal{G}}^{\mathcal{C}_i}, \bar{\mathbf{q}}_{\mathcal{G}}^{\mathcal{C}}, \bar{N}^k\right) + H_{\phi,i}^{k}|_{\bar{\mathbf{X}}_{\mathrm{BA}}} \Delta \mathbf{X}_{\mathrm{BA}} + w_{\mathrm{AB},i}^{\mathrm{j1}} \tag{4.23}$$

where

$$H_{\phi,i}^{k}|_{\bar{\mathbf{X}}_{\mathrm{BA}}} = \frac{\partial h_{\phi}}{\partial \mathbf{X}_{\mathrm{BA}}} \tag{4.24}$$

$$= \left.\left[0, \ldots, 0, \frac{\partial h_{\phi}}{\partial \mathbf{x}_{\mathcal{G}}^{\mathcal{C}_i}}, \frac{\partial h_{\phi}}{\partial \delta \mathbf{e}_{\mathcal{G}}^{\mathcal{C}_i}}, 0, \ldots, 0, \frac{\partial h_{\phi}}{\partial N^k}, 0, \ldots, 0\right]\right|_{\bar{\mathbf{X}}_{\mathrm{BA}}} \tag{4.25}$$

is the $1 \times (6L + P + 3M)$ Jacobian matrix, where $\frac{\partial h_{\phi}}{\partial \mathbf{x}_{\mathcal{G}}^{\mathcal{C}_i}}$, $\frac{\partial h_{\phi}}{\partial \delta \mathbf{e}_{\mathcal{G}}^{\mathcal{C}_i}}$, and $\frac{\partial h_{\phi}}{\partial N^k}$ are the partial derivatives of (4.3) with respect to the relevant state elements and can be expanded as:

$$\left.\frac{\partial h_\phi}{\partial \mathbf{x}_{\mathcal{G}}^{\mathcal{C}_i}}\right|_{\bar{\mathbf{X}}} = \left(\hat{\bar{\mathbf{r}}}_{\mathrm{B},i}^{1} - \hat{\bar{\mathbf{r}}}_{\mathrm{B},i}^{j}\right)^{\mathsf{T}} \tag{4.26}$$

$$\left.\frac{\partial h_\phi}{\partial \delta\mathbf{e}_{\mathcal{G}}^{\mathcal{C}_i}}\right|_{\bar{\mathbf{X}}} =2\left(\hat{\bar{\mathbf{r}}}_{\mathrm{B},i}^{1} - \hat{\bar{\mathbf{r}}}_{\mathrm{B},i}^{j}\right)^{\mathsf{T}}\left[R\left(\bar{\mathbf{q}}_{\mathcal{G}}^{\mathcal{C}}\right)\mathbf{x}_{\mathcal{C}_i}^{\mathcal{A}}\times\right] \tag{4.27}$$

$$\left.\frac{\partial h_\phi}{\partial N^k}\right|_{\bar{\mathbf{X}}} = \lambda \tag{4.28}$$

$$\tag{4.29}$$

where

$$\hat{\bar{\mathbf{r}}}_{\mathrm{B},i}^{\beta} \triangleq \frac{\mathbf{x}_i^{\beta} - \bar{\mathbf{x}}_{B,i}}{\left\|\mathbf{x}_i^{\beta} - \mathbf{x}_{B,i}^{-}\right\|} \tag{4.30}$$

is the unit vector pointing from $\bar{\mathbf{x}}_{\mathrm{B},i}$ to $\mathbf{x}_i^k$. $\bar{\mathbf{x}}_{B,i}$ is the prior position estimate of receiver B's GNSS antenna phase center, which can be modeled as a function of prior state elements as follows:

$$\bar{\mathbf{x}}_{B,i} = \left(\bar{\mathbf{x}}_{\mathcal{G}}^{\mathcal{C}_i} + R\left(\bar{\mathbf{q}}_{\mathcal{G}}^{\mathcal{C}}\right)\right)\mathbf{x}_{\mathcal{C}_i}^{\mathcal{A}}. \tag{4.31}$$

4.2.3 State Estimation

Optimal maximum *a posteriori* state estimates, $\hat{\mathbf{x}}_k$ and $\hat{\mathbf{n}}_k$, $k = 1, 2, \ldots$, can be produced by incorporating all GNSS carrier phase and feature point measurements into a cost function and minimizing the cost as a function of the state.

4.2.3.1 Cost Function

The cost function can be written as a function of the state $\mathbf{X}_{BA}$ as follows:

$$\begin{aligned} f_{\mathrm{NL}}\left(\mathbf{X}_{BA}\right) = \sum_{i=1}^{L}\Bigg[&\left\|R_{y_{\phi,i}}^{-1/2}\left(\mathbf{y}_{\phi,i} - \mathbf{h}_\phi\left(\mathbf{x}_{\mathcal{G}}^{\mathcal{C}_i}, \mathbf{q}_{\mathcal{G}}^{\mathcal{C}_i}, \mathbf{N}\right)\right)\right\| \\ &+ \sum_{j=1}^{M}\left\|R_{\mathbf{y}_i^{\mathrm{p}_j}}^{-1/2}\left(\mathbf{y}_i^{\mathrm{p}_j} - \mathbf{h}_y\left(\mathbf{x}_{\mathcal{G}}^{\mathcal{C}_i}, \mathbf{q}_{\mathcal{G}}^{\mathcal{C}_i}, \mathbf{x}_{\mathcal{G}}^{p_j}\right)\right)\right\|\Bigg] \end{aligned} \tag{4.32}$$

where $\mathbf{y}_i^{\mathrm{p}_j}$ and $\mathbf{h}_y\left(\mathbf{x}_{\mathcal{G}}^{\mathcal{C}_i}, \mathbf{q}_{\mathcal{G}}^{\mathcal{C}_i}, \mathbf{x}_{\mathcal{G}}^{p_j}\right)$, for $i = 1, 2 \ldots, L$, $j = 1, 2 \ldots, M$, are the point feature measurements and measurement models, as defined previously, $\mathbf{y}_{\phi,i}$ and $\mathbf{h}_\phi\left(\mathbf{x}_{\mathcal{G}}^{\mathcal{C}_i}, \mathbf{q}_{\mathcal{G}}^{\mathcal{C}}, N\right)$ are stacked vectors of the previously defined GNSS carrier phase measurements and measurement models at pose i for $i = 1, 2 \ldots, L$, expanded as

$$\mathbf{y}_{\phi,i} \triangleq \left[y_{\phi,i}^1, y_{\phi,i}^2, \ldots, y_{\phi,i}^P\right]^T \tag{4.33}$$

$$\mathbf{h}_\phi\left(\mathbf{x}_{\mathcal{G}}^{\mathcal{C}_i}, \mathbf{q}_{\mathcal{G}}^{\mathcal{C}}, N\right) \triangleq \begin{bmatrix} h_\phi\left(\mathbf{x}_{\mathcal{G}}^{\mathcal{C}_i}, \mathbf{q}_{\mathcal{G}}^{\mathcal{C}}, N^1\right) \\ h_\phi\left(\mathbf{x}_{\mathcal{G}}^{\mathcal{C}_i}, \mathbf{q}_{\mathcal{G}}^{\mathcal{C}}, N^2\right) \\ \vdots \\ h_\phi\left(\mathbf{x}_{\mathcal{G}}^{\mathcal{C}_i}, \mathbf{q}_{\mathcal{G}}^{\mathcal{C}}, N^P\right) \end{bmatrix}, \tag{4.34}$$

and

$$\mathbf{R}_{\mathbf{y}_i^{\mathrm{p}_j}} \triangleq \sigma_{p_i^j}^2 \begin{bmatrix} 1 & 0 & \ldots & 0 \\ 0 & 1 & & \vdots \\ \vdots & & \ddots & 0 \\ 0 & \ldots & 0 & 1 \end{bmatrix} \tag{4.35}$$

and

$$\mathbf{R}_{y_{\phi,i}} \triangleq \sigma_{\phi_i}^2 \begin{bmatrix} 4 & 2 & \ldots & 2 \\ 2 & 4 & & \vdots \\ \vdots & & \ddots & 2 \\ 2 & \ldots & 2 & 4 \end{bmatrix} \tag{4.36}$$

are the measurement covariance matrices for the feature point and carrier phase measurements, respectively, whose inverse square root are used to normalize the noise in the measurements. $\sigma_{p_i^j}$ is the standard deviation of the point feature measurement noise, in pixels, for $i = 1, 2 \ldots, L$, $j = 1, 2 \ldots, M$, and σ_{ϕ_i} is the standard deviation of the undifferenced carrier phase measurements, in meters, for $i = 1, 2 \ldots, L$. The measurement noise is assumed zero mean and uncorrelated in time. Such is a reasonable assumption for feature point measurements, in general, and for a GNSS receiver antenna that is in motion.

Minimization of (4.32) is performed by linearizing the function about an initial guess of the state $\bar{\mathbf{X}}_{BA}$ and then solving for the incremental state update $\Delta\mathbf{X}_{BA}$, as described in the next two subsections.

4.2.3.2 Linearized Cost Function

The linearized form of (4.32) can be written as a function of $\Delta\mathbf{X}_{BA}$ as follows:

$$f_{\mathrm{L}}\left(\Delta\mathbf{X}_{BA}\right)|_{\bar{\mathbf{X}}_{BA}} = \sum_{i=1}^{L}\left[\left\|R_{y_{\phi,i}}^{-1/2}\left(\bar{\mathbf{z}}_{\phi,i} - H_{\phi,i}\Delta\mathbf{X}_{BA}\right)\right\| + \sum_{j=1}^{M}\left\|R_{\mathbf{y}_i^{\mathrm{p}j}}^{-1/2}\left(\bar{\mathbf{z}}_i^j - H_i^j\Delta\mathbf{X}_{BA}\right)\right\|\right] \tag{4.37}$$

where

$$\bar{\mathbf{z}}_i^j \triangleq \mathbf{y}_i^{\mathrm{p}j} - \mathbf{h}_y\left(\bar{\mathbf{x}}_{\mathcal{G}}^{\mathcal{C}_i}, \bar{\mathbf{q}}_{\mathcal{G}}^{\mathcal{C}_i}, \bar{\mathbf{x}}_{\mathcal{G}}^{p_j}\right) \tag{4.38}$$

and

$$\bar{\mathbf{z}}_{\phi,i} \triangleq \mathbf{y}_{\phi,i} - \mathbf{h}_\phi\left(\bar{\mathbf{x}}_{\mathcal{G}}^{\mathcal{C}_i}, \bar{\mathbf{q}}_{\mathcal{G}}^{\mathcal{C}}, \bar{N}\right). \tag{4.39}$$

$H_{\phi,i}$ is a vector of stacked Jacobian matrices of the GNSS carrier phase measurement model at pose i, $i = 1, 2 \ldots, L$, giving

$$H_{\phi,i} \triangleq \left[H_{\phi,i}^1|_{\bar{\mathbf{X}}_{\mathrm{BA}}}, H_{\phi,i}^2|_{\bar{\mathbf{X}}_{\mathrm{BA}}}, H_{\phi,i}^P|_{\bar{\mathbf{X}}_{\mathrm{BA}}}\right]^T, \tag{4.40}$$

and H_i^j is the Jacobian matrix of the point feature measurement model, defined previously.

4.2.3.3 Minimization of the Linearized Cost Function

According to the first-order necessary conditions for the minimization of a linear function, the minimization of (4.37) can be achieved by setting its gradient with respect $\Delta\mathbf{X}_{BA}$ to zero and solving for $\Delta\mathbf{X}_{BA}$ [77]. This gives

$$
\begin{aligned}
0 =& \nabla_{\Delta\mathbf{X}_{BA}} f_1\left(\Delta\mathbf{X}_{BA}\right) && (4.41)\\
=& \sum_{i=1}^{L}\Bigg[-\left(H_{\phi,i}\right)^T R_{y_{\phi,i}}^{-1}\left(\bar{\mathbf{z}}_{\phi,i} - H_{\phi,i}\Delta\mathbf{X}_{BA}\right) && (4.42)\\
&+ \sum_{j=1}^{M} -(H_i^j)^T R_{\mathbf{y}_i^{\mathrm{p}j}}^{-1}\left(\bar{\mathbf{z}}_i^j - H_i^j\Delta\mathbf{X}_{BA}\right)\Bigg]. && (4.43)
\end{aligned}
$$

Bringing the unknown terms to the left-hand side and known terms to the right-hand side of the equation, we arrive at

$$
\begin{aligned}
&\sum_{i=1}^{L}\left[(H_{\phi,i})^T R_{y_{\phi,i}}^{-1} H_{\phi,i} + \sum_{j=1}^{M}(H_i^j)^T R_{\mathbf{y}_i^{\mathrm{p}j}}^{-1} H_i^j\right]\Delta\mathbf{X}_{BA} \qquad (4.44)\\
=&\sum_{i=1}^{L}\left[(H_{\phi,i})^T R_{y_{\phi,i}}^{-1}\bar{\mathbf{z}}_{\phi,i} + \sum_{j=1}^{M}(H_i^j)^T R_{\mathbf{y}_i^{\mathrm{p}j}}^{-1}\bar{\mathbf{z}}_i^j\right]
\end{aligned}
$$

After performing the summations, (4.44) can be re-written in matrix form, giving

$$
\begin{bmatrix} U & W \\ W^T & V \end{bmatrix}
\underbrace{\begin{bmatrix} \begin{bmatrix} \Delta\mathbf{X}_{\mathcal{C}} \\ \Delta\mathbf{N} \end{bmatrix} \\ \Delta\mathbf{X}_{\mathcal{P}} \end{bmatrix}}_{\Delta\mathbf{X}_{BA}}
=
\begin{bmatrix} \begin{bmatrix} \boldsymbol{\epsilon}_c \\ \boldsymbol{\epsilon}_n \end{bmatrix} \\ \boldsymbol{\epsilon}_p \end{bmatrix}, \qquad (4.45)
$$

where $\Delta\mathbf{X}_{\mathcal{C}}$, $\Delta\mathbf{N}$, and $\Delta\mathbf{X}_{\mathcal{P}}$ are the components of $\Delta\mathbf{X}_{BA}$ corresponding to increments to the the camera pose, the carrier phase integer ambiguity, and the point feature state elements, respectively. Note that, due to the integer nature of $\mathbf{N}$, $\Delta\mathbf{N}$ is also integer, and thus we cannot solve for an exact solution to (4.45). We shall instead solve for $\Delta\mathbf{X}_{BA}$ subject to this integer-state constraint, which minimizes the difference between both sides of (4.45).

V in (4.45) is sparse. By sparse, we mean that V is block diagonal with 3×3 block diagonal elements corresponding to each point feature location. Such sparsity can be taken advantage of here in our combined CDGNSS-BA estimator—as in traditional image-only bundle adjustment problems [127]—to more efficiently solve for the minimizing $\Delta \mathbf{X}_{BA}$ in (4.45); rather than inverting the entire matrix on the left side of (4.45), we can first pre-multiply both sides of (4.45) by a special matrix [127], giving

$$
\begin{aligned}
&\begin{bmatrix} I & -W\left(V\right)^{-1} \\ 0 & I \end{bmatrix} \begin{bmatrix} U & W \\ W^T & V \end{bmatrix} \begin{bmatrix} \begin{bmatrix} \Delta \mathbf{X}_{\mathcal{C}} \\ \Delta \mathbf{N} \end{bmatrix} \\ \Delta \mathbf{X}_{\mathcal{P}} \end{bmatrix} \\
&= \begin{bmatrix} U - W\left(V\right)^{-1} W^T & 0 \\ W^T & V \end{bmatrix} \begin{bmatrix} \begin{bmatrix} \Delta \mathbf{X}_{\mathcal{C}} \\ \Delta \mathbf{N} \end{bmatrix} \\ \Delta \mathbf{X}_{\mathcal{P}} \end{bmatrix} \qquad (4.46) \\
&= \begin{bmatrix} I & -W\left(V\right)^{-1} \\ 0 & I \end{bmatrix} \begin{bmatrix} \begin{bmatrix} \boldsymbol{\epsilon}_c \\ \boldsymbol{\epsilon}_n \end{bmatrix} \\ \boldsymbol{\epsilon}_p \end{bmatrix},
\end{aligned}
$$

and then solve for $\Delta \mathbf{X}_{\mathcal{C}}$, $\Delta \mathbf{N}$, and $\Delta \mathbf{X}_{\mathcal{P}}$ incrementally, as follows

$$
\begin{bmatrix} \Delta \hat{\mathbf{X}}_{\mathcal{C}} \\ \Delta \hat{\mathbf{N}} \end{bmatrix} = \left(U - W\left(V\right)^{-1} W^T\right)^{-1} \left(\begin{bmatrix} \boldsymbol{\epsilon}_c \\ \boldsymbol{\epsilon}_n \end{bmatrix} - W\left(V\right)^{-1} \boldsymbol{\epsilon}_p \right) \qquad (4.47)
$$

where the "$\hat{}$" on $\Delta \mathbf{X}_{\mathcal{C}}$ and $\Delta \mathbf{N}$ denotes these being estimates on the basis of float ambiguities. That is, these are the estimates on the basis of non-integer-constrained estimate for $\Delta \mathbf{N}$. The integer-constrained or "fixed" estimate of $\Delta \mathbf{N}$, denoted $\Delta \check{\mathbf{N}}$, can be determined using the Least-squares Ambiguity Decorrelation Adjustment (LAMBDA) method [15] to solve the following minimization problem

$$
\Delta \check{\mathbf{N}} = \underset{\Delta \mathbf{N} \in \mathbb{Z}^P}{\operatorname{argmin}} \left(\Delta \hat{\mathbf{N}} - \Delta \mathbf{N} \right)^T Q_{\mathbf{N}}^{-1} \left(\Delta \hat{\mathbf{N}} - \Delta \mathbf{N} \right) \qquad (4.48)
$$

where

$$\begin{bmatrix} Q_{\mathbf{X}_\mathcal{C}} & Q_{\mathbf{X}_\mathcal{C}\mathbf{N}} \\ Q_{\mathbf{N}\mathbf{X}_\mathcal{C}} & Q_{\mathbf{N}} \end{bmatrix} \triangleq U - W\left(V\right)^{-1} W^T. \tag{4.49}$$

The fixed ambiguity estimate $\Delta\check{\mathbf{N}}$ can then be used to determine $\Delta\check{\mathbf{X}}_\mathcal{C}$, the estimate of $\Delta\mathbf{X}_\mathcal{C}$ on the basis of integer-constrained ambiguities [15]:

$$\Delta\check{\mathbf{X}}_\mathcal{C} = \Delta\hat{\mathbf{X}}_\mathcal{C} - Q_{\mathbf{X}_\mathcal{C}\mathbf{N}} Q_{\mathbf{N}}^{-1} \left(\Delta\hat{\mathbf{N}} - \Delta\mathbf{N}\right)^T \tag{4.50}$$

Lastly, the state increment for the point feature positions $\Delta\mathbf{X}_\mathcal{P}$ can be determined via back-substitution, giving

$$\Delta\check{\mathbf{X}}_\mathcal{P} = \left(V\right)^{-1} \left(\boldsymbol{\epsilon}_p - W^T \begin{bmatrix} \Delta\check{\mathbf{X}}_\mathcal{C} \\ \Delta\check{\mathbf{N}} \end{bmatrix}\right). \tag{4.51}$$

We now have all the components to form the state increment estimate

$$\Delta\hat{\mathbf{X}}_{\mathrm{BA}} = \begin{bmatrix} \check{\mathbf{X}}_\mathcal{C} \\ \check{\mathbf{N}} \\ \check{\mathbf{X}}_\mathcal{P} \end{bmatrix} \tag{4.52}$$

that minimizes the linearized cost function of (4.37).

4.2.3.4 Solution Computational efficiency

Note that the only matrix inversions necessary during this minimization were V^{-1}, which, due to the sparse block-matrix-form of V, is computationally efficient to compute, and $\left(U - W\left(V\right)^{-1} W^T\right)$ in (4.47), which, although not sparse like V, is only of dimension $6L + P$.

4.2.3.5 Levenberg-Marquardt Algorithm

The procedure outlined in Sec. 4.2.3.3 to determine the state increment estimate $\Delta\hat{\mathbf{X}}_{\mathrm{BA}}$ defines one iteration of the Levenberg-Marquardt algorithm (LMA), a popular iterative non-linear solver. To converge on the solution, it is often the case that multiple LMA iterations are needed. The full procedure for LMA is as follows:

1. Given a prior for the state $\bar{\mathbf{X}}_{\mathrm{BA}}$, use the procedure of Sec. 4.2.3.3 to determine the state increment estimate $\Delta\hat{\mathbf{X}}_{\mathrm{BA}}$.

2. Accumulate $\Delta\hat{\mathbf{X}}_{\mathrm{BA}}$ with the prior state estimate, giving the updated state estimate,

$$\hat{\mathbf{X}}_{\mathrm{BA}} \triangleq \bar{\mathbf{X}}_{\mathrm{BA}} \tilde{+} \Delta\hat{\mathbf{X}}_{\mathrm{BA}} \tag{4.53}$$

   where the $\tilde{+}$ term represents the accumulation of all state elements via standard addition except for the quaternion elements, which must be accumulated via quaternion multiplication as outlined in (4.8).

3. Insert $\hat{\mathbf{X}}_{\mathrm{BA}}$ into (4.32) and compute a new cost.

4. Compare this new cost to the old cost computed on behalf of the estimate from the previous LMA iteration or the initial guess, if this is the first iteration.

5. If the cost decreased, then $\hat{\mathbf{X}}_{\mathrm{BA}}$ is set to be the prior, giving

$$\bar{\mathbf{X}}_{\mathrm{BA}} = \hat{\mathbf{X}}_{\mathrm{BA}}, \tag{4.54}$$

   and the algorithm skips to the last step.

6. If the cost has increased, then the diagonal elements of U and V are inflated by a multiplicative factor as follows [126, 127]:

$$\begin{aligned} U^*_{ij} &= \begin{cases} (1+\lambda)U_{ii} & ;\ i=j \\ U_{ij} & ;\ \text{otherwise} \end{cases} \\ V^*_{ij} &= \begin{cases} (1+\lambda)V_{ii} & ;\ i=j \\ V_{ij} & ;\ \text{otherwise} \end{cases} \end{aligned} \tag{4.55}$$

and the minimization procedure of Eqs. (4.47)– (4.52) is repeated with U^* and V^* in place of U and V to obtain a new $\hat{\mathbf{X}}_{\text{BA}}$ and thus a new cost. This current step is repeated, multiplying λ by a factor of 10 each repeat until the cost has decreased (as compared to the cost from the previous LMA iteration). Then, skip to step 3.

7. Check for LMA convergence is determined by comparing (1) the norm of the estimated state increment vector and (2) the change in the cost at the end of each iteration to threshold values [126]. If both threshold checks are passed, then the algorithm is declared to have converged and this procedure exits. Otherwise return to step 1, and repeat.

4.2.4 Covariance

The covariance matrix of the VISRTK solution, assuming an entirely real-valued state, could be solved for by inverting the LHS matrix of the normal equation in (4.45), as is typical in batch least squares estimation [77], giving

$$P_{xx} = \begin{bmatrix} U & W \\ W^T & V \end{bmatrix}^{-1}. \tag{4.56}$$

Furthermore, this inversion can be simplified [126, 127], giving

$$P_{\text{xx}} = \begin{bmatrix} \overbrace{\begin{bmatrix} P_{\text{cc}} & P_{\text{cn}} \\ P_{\text{nc}} & P_{\text{nn}} \end{bmatrix}}^{A} & \begin{bmatrix} P_{\text{cp}} \\ P_{\text{np}} \end{bmatrix} \\ \begin{bmatrix} P_{\text{cp}}^T & P_{\text{np}}^T \end{bmatrix} & P_{\text{pp}} \end{bmatrix}, \tag{4.57}$$

where

$$A = \begin{bmatrix} P_{\text{cc}} & P_{\text{cn}} \\ P_{\text{nc}} & P_{\text{nn}} \end{bmatrix} \triangleq \left(U - WV^{-1}W^T\right)^{-1} \tag{4.58}$$

is the joint camera pose–integer ambiguity covariance matrix, with P_{cc}, P_{nn}, and P_{cn} being the camera pose, integer ambiguity and camera pose/integer ambiguity cross covariance matrices, respectively. Additionally,

$$P_{\text{pp}} \triangleq V^{-T} W^T A W V^{-1} + V^{-1} \tag{4.59}$$

is the point feature position covariance matrix and

$$\begin{bmatrix} P_{\text{cp}} \\ P_{\text{np}} \end{bmatrix} \triangleq -AWV^{-1} \tag{4.60}$$

is a matrix containing the cross-covariances between the camera pose and integer ambiguity states and the point feature position state.

However, since the state component $\mathbf{N}$ is constrained to be integer-valued, it is often the case that it is resolved correctly by the VISRTK estimator. Consequently, the covariance can be adjusted to reflect the (significant) increase in accuracy to the other state components under the assumption that $\mathbf{N}$ is correct. In particular, the covariance for the non-integer-valued state elements conditioned on $\mathbf{N}$ can be shown to be:

$$P_{\text{cc}|\mathbf{N}} = P_{\text{cc}} - P_{\text{cn}} P_{\text{nn}}^{-1} P_{\text{cn}}^T \tag{4.61}$$

and

$$P_{\text{pp}|\mathbf{N}} = P_{\text{pp}} - P_{\text{np}}^T P_{\text{nn}}^{-1} P_{\text{np}} \tag{4.62}$$

4.3 VISRTK Comparison to Existing Estimation Architectures

The current chapter is not the first to suggest combining image measurements with GNSS measurements in a bundle-adjustment-type estimation framework as outlined in the previous section. This section will discuss trade-offs between the current chapter's framework and two existing approaches.

4.3.1 Similarity Transform

One existing way to combine GNSS measurements with image measurements is to do so in a very loosely coupled manner by computing camera pose and point feature position estimates using standard bundle adjustment in the vision coordinate frame, then computing a similarity transformation, i.e., a translation vector, rotation matrix, and scale factor, to translate the estimates from the vision frame into the globally-referenced GNSS reference frame.

A similarity transformation is computed by minimizing the squared difference between the the camera positions computed via GNSS measurements those computed via standalone bundle adjustment and translated into the GNSS frame. Such minimization can be solved in closed form using the so-called Horn transformation [134] if the GNSS antenna and camera centers are aligned or iteratively using a modified form of the Horn transformation [126] if the centers are offset (but still rigidly connected) as is more commonly the case.

The Horn Transform minimizes the following cost function [126]:

$$\begin{aligned} g\left(s, \mathbf{x}_{\mathcal{G}}^{\mathcal{V}}, \mathbf{q}_{\mathcal{G}}^{\mathcal{V}}\right) = & \frac{1}{2} \sum_{i=1}^{L} \left|\left| \frac{1}{\sqrt{s}} \left(\hat{\mathbf{x}}_{\mathcal{G}}^{A_i} - \mathbf{x}_{\mathcal{G}}^{\mathcal{V}} - R\left(\mathbf{q}_{\mathcal{G}}^{\mathcal{V}}\right) R\left(\hat{\mathbf{q}}_{\mathcal{V}}^{\mathcal{C}_i}\right) \mathbf{x}_{\mathcal{C}}^{A}\right) \right.\right. \\ & \left.\left. - \sqrt{s} R\left(\mathbf{q}_{\mathcal{G}}^{\mathcal{V}}\right) \hat{\mathbf{x}}_{\mathcal{V}}^{\mathcal{C}_i} \right|\right|^2 \end{aligned} \tag{4.63}$$

where s, $\mathbf{x}_{\mathcal{G}}^{\mathcal{V}}$, and $\mathbf{q}_{\mathcal{G}}^{\mathcal{V}}$ are the scale-factor, translation, and rotation unknowns, respectively, parameterizing the transform from the vision frame to the GNSS reference frame, $\hat{\mathbf{x}}_{\mathcal{V}}^{\mathcal{C}_i}$ and $\hat{\mathbf{q}}_{\mathcal{V}}^{\mathcal{C}_i}$ are the estimates of the camera position and attitude, respectively, in the vision frame at each epoch i for $i = 1, 2 \ldots, L$, computed from the stand-alone bundle adjustment algorithm, and $\hat{\mathbf{x}}_{\mathcal{G}}^{A_i}$ is the position of the GNSS antenna phase center in the GNSS reference frame, computed from the GNSS measurements.

Once the parameter estimates $\hat{s}$, $\hat{\mathbf{x}}_{\mathcal{G}}^{\mathcal{V}}$, and $\hat{\mathbf{q}}_{\mathcal{G}}^{\mathcal{V}}$ characterizing the similarity transform from the vision to the GNSS reference frame similarity transform are determined, the camera pose and feature point position estimates can be transformed into the GNSS reference frame, giving

$$\begin{aligned}
\hat{\mathbf{x}}_{\mathcal{G}}^{\mathcal{C}_i} &= \hat{\mathbf{x}}_{\mathcal{V}}^{\mathcal{C}_i} + \mathbf{x}_{\mathcal{G}}^{\mathcal{V}} \\
\hat{\mathbf{q}}_{\mathcal{G}}^{\mathcal{C}_i} &= \mathbf{q}_{\mathcal{G}}^{\mathcal{V}} \otimes \mathbf{q}_{\mathcal{V}}^{\mathcal{C}_i} \\
\hat{\mathbf{x}}_{\mathcal{G}}^{\mathcal{P}_j} &= + \hat{\mathbf{x}}_{\mathcal{G}}^{\mathcal{V}}
\end{aligned} \tag{4.64}$$

for $i = 1, 2 \ldots, L$.

Despite that the end result of the horn transform being that the camera pose and feature positions are in the globally reference GNSS reference frame, the downside to this loosely-coupled similarity transform approach is as follows. Errors in the camera pose and point feature position estimates computed via BA in the vision frame will still remain in the GNSS frame after applying the similarity transform. This downside is particularly notable over datasets during which the camera is traveling a far distance or there is little point feature overlap between consecutive camera frames. In these scenarios, the camera pose errors will accumulate from frame-to-frame resulting in a significant camera position and orientation drift.

4.3.2 Loosely Coupled

A second existing way to combine GNSS measurements with image measurements is to do so by combining GNSS *position* measurements with camera feature point measurements into a weighted cost function and minimizing the cost as a function of the camera poses and feature point positions. The position measurements are obtained by a computing a standard pseudorange- or CDGNSS-based solution. By analogy to the coupling of an IMU+GNSS data, this level of coupling—at the level of GNSS positioning solutions—is termed *loosely coupled*. In particular, the cost function that is minimized is as follows:

$$g_{\mathrm{NL}}\left(\mathbf{X}_{BA}\right) = \sum_{i=1}^{L}\left[\left\|R_{x_{\mathcal{G},i}^{\mathcal{A}}}^{-1/2}\left(\tilde{\mathbf{x}}_{\mathcal{G},i}^{\mathcal{A}} - \left(\mathbf{x}_{\mathcal{G}}^{\mathcal{C}_i} + R\left(\mathbf{q}_{\mathcal{G}}^{\mathcal{C}}\right)\mathbf{x}_{\mathcal{C}}^{\mathcal{A}_{\mathrm{B}}}\right)\right)\right\| \right.$$
$$\left. + \sum_{j=1}^{M}\left\|R_{\mathbf{y}_i^{\mathrm{p}_j}}^{-1/2}\left(\mathbf{y}_i^{\mathrm{p}_j} - \mathbf{h}_y\left(\mathbf{x}_{\mathcal{G}}^{\mathcal{C}_i}, \mathbf{q}_{\mathcal{G}}^{\mathcal{C}_i}, \mathbf{x}_{\mathcal{G}}^{p_j}\right)\right)\right\|\right] \tag{4.65}$$

where $\tilde{\mathbf{x}}_{\mathcal{G},i}^{\mathcal{A}}$ is the measurement of the position of the GNSS antenna at epoch i, $i = 1, 2 \ldots, L$ and the other terms are as defined previously.

Like the previously discussed similarity transform approach, the end result of this loosely-coupled approach is that estimates of camera pose and point feature positions are in a global coordinate frame. Unlike, the similarity transform approach, which simply scales, rotates, and translates the BA-based camera pose and point feature position estimates from the camera coordinate system into the global coordinate system, this approach enables the GNSS measurements to correct relative errors in the BA camera pose and point feature position estimates. This is due to the presence of the GNSS position measurements in the first part of the cost function of (4.65).

4.3.3 Tightly Coupled VISRTK (Current Solution)

The current chapter's approach combines GNSS carrier phase and point feature measurements to simultaneously compute (1) camera pose and point feature position estimates in the global coordinate frame and (2) CDGNSS integer ambiguities. By analogy to the coupling of an IMU+GNSS data, this level of coupling—at the level of GNSS carrier phase observables—is termed *tightly coupled*. As with the loosely coupled approach discussed previously, this approach enables the GNSS measurements to correct relative errors in the camera pose and point feature position estimates through a least squares cost minimization (see (4.32)). As compared to the loosely coupled approach, however, this tightly-coupled approach has the following advantages:

- *More Robust:* Much like the benefit that IMU measurements offer to an IMU-CDGNSS framework, the added information from the feature point measurements are in effect a tight constraint on the receiver motion profile. As such, these measurements can be used within the estimator to detect phase measurement outliers and cycle slips and compensate for these. This results in a more accurate camera positioning solution than would have been achievable on the basis of carrier phase measurement alone or a loosely-coupled approach.

- *Faster Initialization:* The motion profile constraint that results from the feature point measurements can additionally be used to reduce the CDGNSS time to ambiguity resolution (TAR) as compared to the TAR achievable on the basis of carrier phase measurement alone, as shown in [35] for an arbitrarily provided motion profile. Sections 4.4 and 4.6 will demonstrate this benefit using simulated and real data, respectively.

- *More Optimal:* The current approach is optimal under the maximum *a posteriori* criteria. It enables the CDGNSS carrier phase and image measurements to be fused into the same non-linear estimator, rather than in two separate estimators, as in the loosely coupled approach, where losses resulting from the non-linearity of the CDGNSS measurement model and the carrier phase integer ambiguity resolution prevent the two methods from being equivalent.

4.3.4 Iterative Loosely Coupled

Yet another approach would be an iterative, back and forth loosely-coupled solution where the output from of the loosely coupled solution described previously is used as a prior in re-computing a CDGNSS solution, the output of which is then again provided to the loosely-coupled algorithm. This is repeated a number of times until convergence. This approach, while removing the optimality downside of the loosely coupled approach, is no better than the tightly coupled solution and would also be more computationally demanding. As such, the approach will not be considered in the subsequent analysis.

4.4 VISRTK Demonstration on Simulated Data

This section analyzes the results of the VISRTK algorithm run on simulated data with noise statistics that model a smartphone camera and GNSS antenna setup. Figure 4.1 shows the results. The red dots in the center of the figure represent the estimated position of the feature points, which were simulated to be uniformly distributed around a cylinder of radius 4 meters. 15 camera poses were simulated in total. Point feature measurements were simulated as would be collected from a series of 15 images, one taken at each camera pose. Additionally, carrier phase measurements were simulated to be collected from signals received by a GNSS antenna fixed atop the camera at the same time epoch that each image was taken. Epochs are simulated to be spaced 30 seconds apart, with the camera moving counterclockwise around the cylinder's center. The cylinder is assumed non-transparent, so only measurements from non-occluded point features are simulated at each epoch. A second GNSS receiver, acting as the reference, with a survey-grade antenna was simulated to be positioned at the center of the cylinder, also collecting carrier phase measure-

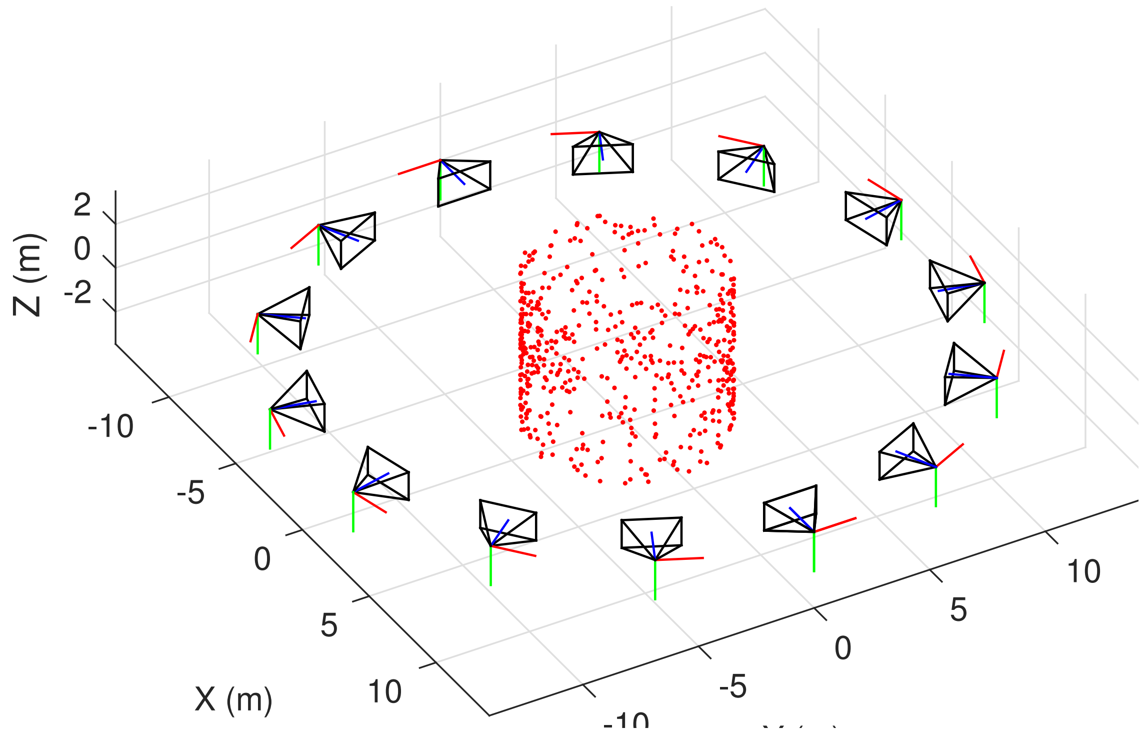

Figure 4.1: Using VISRTK, a three-dimensional, globally referenced, scene is reconstructed from simulated data. The red dots represent the estimated position of the feature points, which were simulated to be uniformly distributed along an cylinder of radius 4 meters. 15 camera poses were simulated in total, evenly distributed around the cylinder's center at a radius of 14 meters. Measurements of each feature point in view and a single epoch of GNSS carrier phase measurements were simulated to be collected at each pose. The reference frame of the plot is in the ECEF coordinate frame, with the origin translated to be that of the reference GNSS antenna, which was simulated to be located at the origin of the cylinder, also collecting GNSS carrier phase measurements.

Table 4.1: Simulated Data Parameters

$\sigma_{p_i^j}$	$\sigma_{\phi_i,\mathrm{B}}$	$\sigma_{\phi_i,\mathrm{A}}$	$\mathbf{x}_{\mathcal{C}_i}^{\mathcal{A}}$	Point Density	Num. SVs	Time Between Epochs
1 pixel	8 mm	2 mm	[0, -.05, -.015] m	3 points/m^2	6	30 s

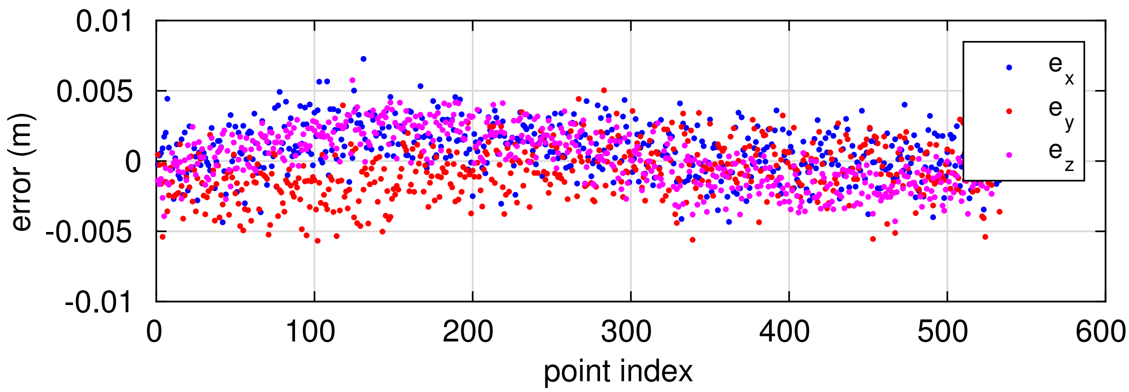

Figure 4.2: VISRTK 3-dimensional point position estimate errors for the 533 points from the simulated seen shown in Fig. 4.1. Errors are in the sub-centimeter range.

ments from the same set of satellites. The GNSS carrier phase measurements from this reference antenna were double-differenced with those collected by the antenna atop the camera. The remainder of the simulation parameters are listed in Table 4.1.

Figures 4.2 and 4.3 display the point feature position and camera pose errors, respectively, from a VISRTK solution computed using measurements from all 15 poses. To compute these errors the known truth values at each point or camera pose index are subtracted from the VISRTK state estimates. A majority of the point feature position estimates are accurate to less than 0.5 millimeters. The camera positions are accurate to less than 1 cm and the camera orientations are

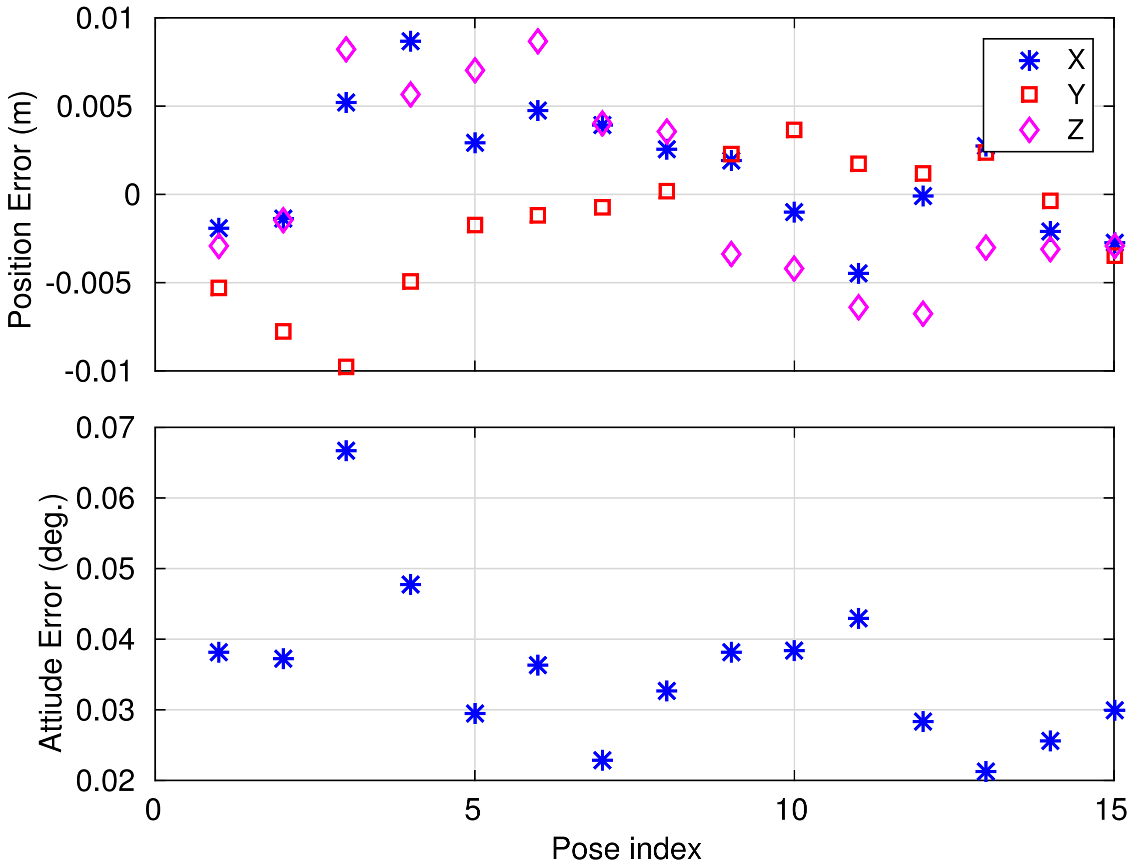

Figure 4.3: VISRTK 3-dimensional camera position (top panel) and attitude (bottom panel) estimate errors for the 15 camera poses illustrated in Fig. 4.1. Camera positional errors are in the sub-centimeter range and attitude errors are in the sub-degree range.

accurate to less than 0.1 degrees.

4.5 Demonstrating VISRTK Key Advantages

This section demonstrates using simulated data two advantages of the VISRTK estimation architecture over the two preexisting estimation architectures discussed in Sec. 4.3, the similarity transform architecture and the loosely-coupled architecture.

4.5.1 Reduced Time to Successful Ambiguity Resolution

One advantage of VISRTK over the existing approaches is that it enables information the image measurements to aid in the resolution of the CDGNSS integer ambiguities, enabling a shorter TAR as compared to existing approaches. Feature point measurements and carrier phase ambiguities are jointly processed within the same non-linear cost function (see (4.32)), enabling the feature point measurements to aid in the estimation of the integer ambiguity vector $\mathbf{N}$. Such aiding is not possible in existing frameworks, e.g., the Horn transform and loosely-coupled framework, as a standalone CDGNSS solution is carried out in advance. Consequently, for these existing frameworks, the information transfer is one way; from the standalone CDGNSS solution (in which the integer ambiguities were already resolved) to the horn transform or loosely coupled framework.

Figure 4.4 compares the VISRTK ambiguity success rate (ASR) as a function of the number of measurement epochs used in the solution to that of (1) a standalone CDGNSS solution computed on behalf of GNSS carrier phase measurements only and (2) a standalone CDGNSS solution with a noise-free antenna motion profile prior, i.e., assuming the between-epoch relative trajectory of the GNSS antenna is

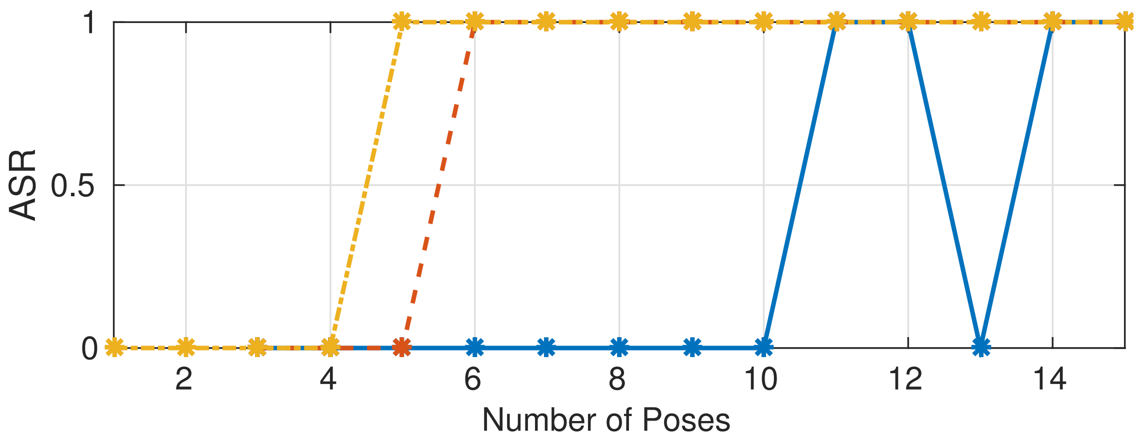

Figure 4.4: Plot comparing the VISRTK ASR (orange dashed trace), the standalone CDGNSS ASR (blue solid trace), and the CDGNSS ASR given a perfect motion profile (yellow dash-dotted trace) as a function of the number of measurement epochs used in the solution. All were computed on the basis of simulated data, characterized in Table 4.1. It is clear that the motion constraint offered by the addition of feature point measurements enables faster ambiguity resolution for VISRTK, approaching the TAR of the CDGNSS solution in which an error-free motion constraint was provided.

known perfectly and provided to the standalone CDGNSS estimator (see [35]). All three solutions were computed using simulated measurements from the simulation scenario depicted in Fig. 4.4, the parameters for which are listed in Table 4.1. It is clear from the figure that the information provided to the VISRTK estimator by the feature point measurements resulted in faster ambiguity resolution than standalone CDGNSS for which no feature point measurements were available. This benefit to TAR is similar to that gained by a CDGNSS solution with an *a priori* motion profile, as evidenced by the orange and yellow traces in Fig. 4.4 both outperforming that of the blue trace. The feature point measurements effectively act as a near-perfect antenna motion constraint within VISRTK, constraining the relative camera pose and positions. As seen in the figure, however, the effective motion profile constraint offered by the image measurements, while very good, is still noisy, degrading its benefit to ASR as compared to that of a perfect motion profile prior.

4.5.2 Jumpstart VISRTK

A second advantage of VISRTK is that it can incorporate prior information on the position of identified point features to improve the estimability of the estimator's state, particularly, the integer ambiguity state component $\mathbf{N}$. This process shall be termed "Jumpstart VISRTK," as this information results in a speed up or *jumpstart* of the ambiguity resolution process, in many cases, leading to single-epoch or instantaneous ambiguity resolution, e.g., successful ambiguity resolution requiring only one epoch of measurements.

To include *a priori* point feature position information within the batch estimation framework, the cost function of (4.32) is expanded as follows:

$$
\begin{aligned}
f_{\mathrm{NL}}\left(\mathbf{X}_{BA}\right) = \sum_{i=1}^{L} \Bigg[& \underbrace{\left\| R_{y_{\phi,i}}^{-1/2}\left(\mathbf{y}_{\phi,i} - \mathbf{h}_{\phi}\left(\mathbf{x}_{\mathcal{G}}^{\mathcal{C}_i}, \mathbf{q}_{\mathcal{G}}^{\mathcal{C}_i}, \mathbf{N}\right)\right)\right\|}_{\text{Term involving GNSS measurements}} \\
& \underbrace{+ \sum_{j=1}^{M} \left\| R_{\mathbf{y}_i^{\mathrm{p}_j}}^{-1/2}\left(\mathbf{y}_i^{\mathrm{p}_j} - \mathbf{h}_y\left(\mathbf{x}_{\mathcal{G}}^{\mathcal{C}_i}, \mathbf{q}_{\mathcal{G}}^{\mathcal{C}_i}, \mathbf{x}_{\mathcal{G}}^{p_j}\right)\right)\right\|}_{\text{Term involving point feature measurements}} \Bigg] \\
& + \underbrace{\sum_{j=1}^{M} \left\| R_{\bar{\mathbf{x}}_{\mathcal{G}}^{\mathrm{p}_j}}^{-1/2}\left(\bar{\mathbf{x}}_{\mathcal{G}}^{\mathrm{p}_j} - \mathbf{x}_{\mathcal{G}}^{\mathrm{p}_j}\right)\right\|}_{\text{Term involving } a\ priori \text{ point feature information}}
\end{aligned}
\tag{4.66}
$$

where $\bar{\mathbf{x}}_{\mathcal{G}}^{\mathrm{p}_j}$, $j = 1, 2, \ldots, M$ are the 3×1 point position priors and

$$
R_{\bar{\mathbf{x}}_{\mathcal{G}}^{\mathrm{p}_j}} \triangleq \sigma_{\bar{\mathbf{x}}_{\mathcal{G}}^{\mathrm{p}_j}}^{2} \mathbf{I}_{3\times 3}, \ \ j = 1, 2, \ldots, M \tag{4.67}
$$

3×3 measurement covariance matrices associated with these priors, where $\sigma_{\bar{\mathbf{x}}_{\mathcal{G}}^{\mathrm{p}_j}}$, $j = 1, 2, \ldots, M$ model the per-dimension standard deviation. For the subset of feature points, $k \subseteq \{1, 2, \ldots, M\}$, for which no prior information is available, the standard deviation associated with these points is set to infinity, i.e., $\sigma_{\bar{\mathbf{x}}_{\mathcal{G}}^{\mathrm{p}_k}} = \infty$, $k \subseteq \{1, 2, \ldots, M\}$.

Figure 4.5 illustrates a reconstructed scene whereby 50 feature points (shown in blue) have centimeter-accurate positional priors that are provided to the VISRTK estimator and used to compute single-epoch VISRTK solution. Using this prior information along with measurements of the 50 feature points and the GNSS carrier phase measurements from this 1 camera frame, the camera's pose was estimated in the global ECEF reference frame to sub-centimeter and sub-degree accuracy. Accordingly, the carrier phase integer ambiguities were also successfully estimated.

Figure 4.6 illustrates the results of a VISRTK solution computed using point feature and GNSS measurements from 15 cameras frames. The blue points are the points for which a positional prior was available, the same 50 points and point priors used in Fig. 4.5. The red points, in contrast, are points for which no prior information was available. Through linearization and iterative minimization of the augmented cost function of (4.66), the positional priors were able to aid in the estimation of all state components, including the CDGNSS integer ambiguity state vector.

Figure 4.7 compares the ASR of Jumpstart VISRTK solution whose results are visualized in Fig. 4.6 to that of standalone CDGNSS solution. It is clear that the VISRTK solution for which prior information on the location of the 50 feature points was available enables accurate integer ambiguity resolution, even on the basis of measurements from the first camera frame. Accordingly, unlike would be the case when incorporating prior point feature position information into the Horn or

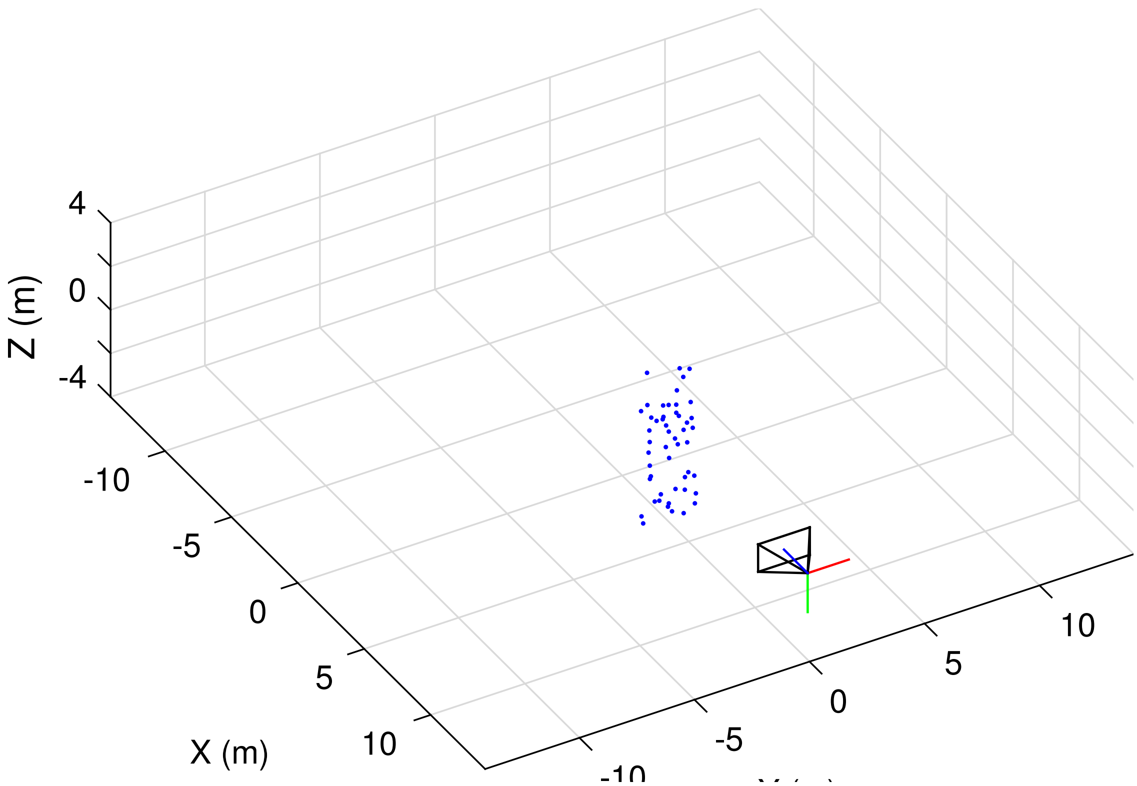

Figure 4.5: A 3D reconstruction using Jumpstart VISRTK from simulated GNSS and GNSS carrier phase data collected by the first camera frame of the simulation scenario outlined in. The 50 points shown (in blue) are the only points observable from the measurements made by a single camera frame as they have positional prior information associated with them. This prior information along with the GNSS and feature point measurements was by VISRTK to accurate estimate the pose of the camera as well as successfully resolve the carrier phase ambiguities.

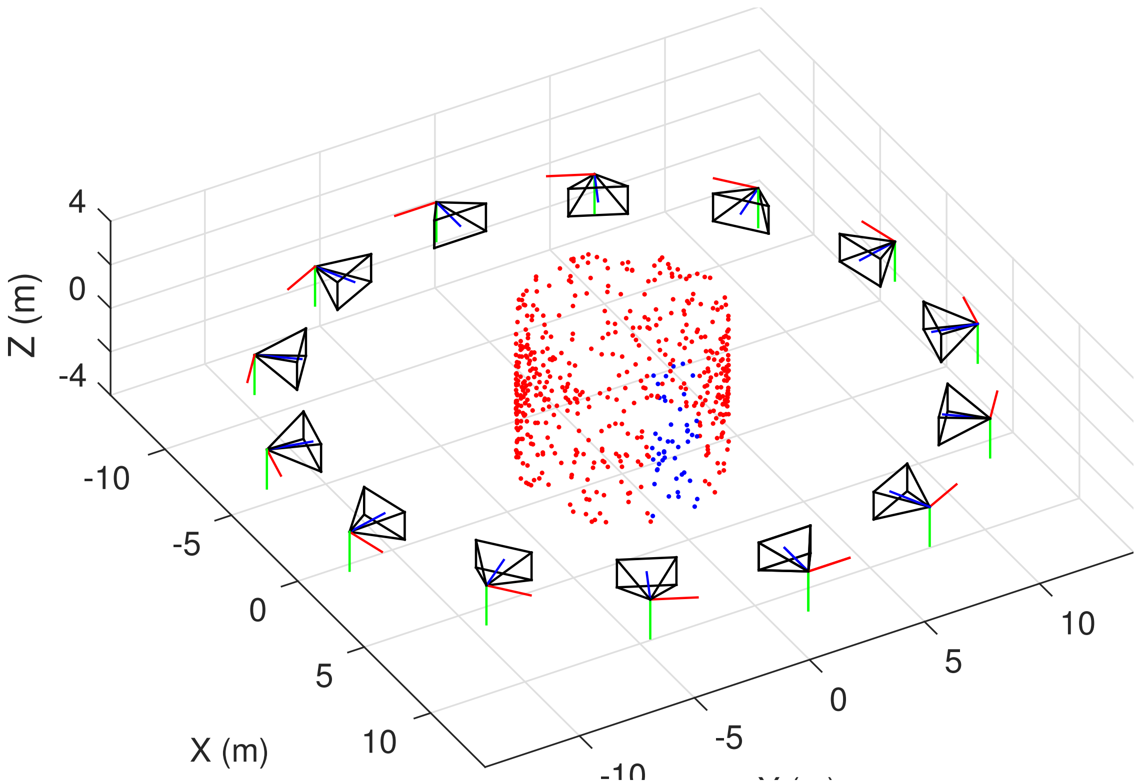

Figure 4.6: A 3D reconstruction using Jumpstart VISRTK from simulated feature point and GNSS carrier phase measurements collected by the first camera frame of the simulation scenario illustrated in Fig. 4.1. The 50 points (shown in blue) have positional prior information associated with them and are thus the only points whose positions are observable on the basis of measurements from a single camera pose. This positional prior information along with the GNSS and feature point measurements were ingested by VISRTK and used to accurately estimate the pose of the camera, while successfully resolving the carrier phase ambiguities associated with the GNSS carrier phase measurements.

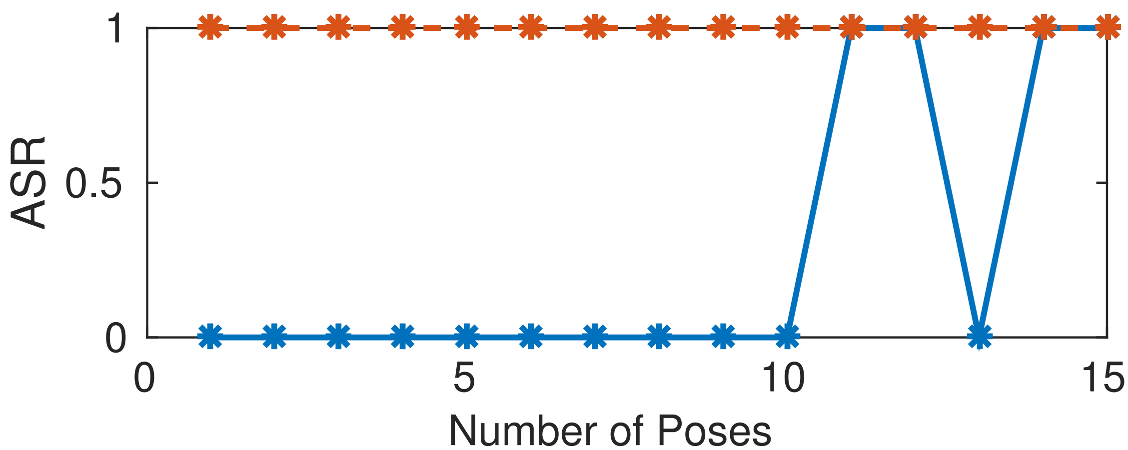

Figure 4.7: Plot comparing the VISRTK ASR (orange dashed trace) and the standalone CDGNSS ASR (blue solid trace) as a function of the number of measurement epochs used in the solution. Both were computed on the basis of simulated data, characterized in Table 4.1, whose results are simulated in Fig. 4.6. Centimeter-accurate positional priors on the 50 points illustrated in blue in Fig. 4.6 were used in VISRTK to enable instantaneous ambiguity resolution.

loosely-coupled frameworks described in Sec. 4.3, Jumpstart VISRTK enables the carrier phase ambiguity resolution to be aided by this prior information and, in this simulated scenario, resolved instantaneously, on the basis of feature point and GNSS measurements from only one camera frame. Furthermore, as illustrated by the blue trace, when resolving the integer ambiguities using standard CDGNSS in which no vision measurements are available, it takes 14 frames of GNSS measurements to resolve the ambiguities correctly.

4.6 VISRTK Demonstration on Real Data

This section describes the results of a VISRTK solution computed using real data. Data were collected using a VISRTK platform consisting of a Samsung Galaxy Note 4 smartphone whose camera was used to take images while a low-cost 25 millimeter GPS patch antenna affixed atop the smartphone was used to collect GPS data. Figure 4.8 illustrates this platform.

4.6.1 Data Collection and Processing

The procedure for collecting images and GPS data for VISRTK processing was as follows:

1. The VISRTK platform pictured in Fig. 4.8 was affixed atop a tripod with the smartphone's camera pointed downward, slightly, toward a scene on the ground. Fig. 4.9 shows the scene.

2. A photo was taken of the scene while raw intermediate-frequency (IF) GPS samples were collected from the GPS antenna affixed atop the smartphone.

3. The tripod was moved 25 degrees counter-clockwise in a 2-meter-radius arc

Figure 4.8: The VISRTK platform consisting of a Samsung Galaxy Note 4 smartphone whose camera was used to take images while a low-cost 25 millimeter Abracon GPS patch antenna affixed atop the smartphone was used to collect raw intermediate frequency (IF) GPS data. While a user is shown holding the platform here, to enable spatial synchronization between the images taken and GNSS data collected from the antenna, most of the data was collected with the platform atop a tripod.

around the scene.

4. Another photo was taken, again, while was static in the new location.

5. Steps 3 and 4 were repeated until the platform completed a full 360-degree arc around the scene. 14 photos at 14 different poses were taken in all, spaced approximately uniformly around the scene. Consecutive poses are separated in time by approximately 30 seconds.

6. Raw IF GPS samples were collected continuously throughout from the GPS antenna affixed atop the smartphone and also from a nearby survey-grade antenna, acting as a reference.

7. Immediately prior to the above data collection, 15 minutes of raw IF GPS samples were collected from the high-quality patch antenna shown on top of the sewer grate in Fig. 4.9. These data will be used to determine the accuracy of the VISRTK solution, as detailed in Sec. 4.6.2.3.

The collected data were next prepared and processed through the VISRTK algorithm as follows:

1. The smartphone and reference antenna raw IF data streams were provided as inputs to a software GNSS receiver known as GRID [78–80]. GRID processed the data and produced as its output undifferenced carrier-phase measurement time histories for each signal tracked. The time histories were timestamped to nanosecond accuracy in GPS time.

2. The undifferenced carrier phase measurements produced from the rover antenna (on the VISRTK platform) were time aligned with those from the reference antenna via interpolation. The aligned time histories were double differ-

Figure 4.9: One of the 14 images taken of a scene using the VISRTK platform illustrated in Fig. 4.8. The scene, which is on the roof of WRW building at The University of Texas at Austin, consists of (1) a drop-light, (2) a large metal beam, and (3) a high-quality GPS patch antenna. Measurements from the this GPS antenna will later be used to provide ground truth when evaluating the accuracy of a VISRTK solution.

enced according to (4.17) to form 6 DD carrier-phase time histories from the 7 highest-elevation GPS satellite signals present in the data.

3. Standalone CDGNSS processing was used to produce from the DD carrier phase measurement time history a centimeter-accurate position time history. This position time history was then used to identify and store 14 measurement epochs during which the tripod was static and a new images was taken.

4. The 14 images were pre-processed using a freely-available structure from motion tool known as VisualSFM [135–137]. VisualSFM identified feature points common between 3 or more images and produced measurements of these points. The tool also provided, in the "vision" reference frame, estimates of the position of each identified point as well the position and orientation (pose) of the camera lens when each image was taken.

5. The VisualSFM-produced camera pose estimates in the vision reference frame and the CDGNSS-produced antenna positions in the global reference frame (computed in Step 9) were used to compute a similarity transform between the two reference frames (see the Horn Transform of Eq. (4.63). This transform produced the scale-factor, translation, and rotation matrix parameters that were subsequently used to transform the VisualSFM point feature position and camera pose estimates into the global reference frame (see (4.64)).

6. The resulting transformed estimates were used to form an initial guess for the VISRTK state ($\bar{\mathbf{X}}_{\mathrm{BA}}$).

7. Finally, a VISRTK solution was computed using the iterative LMA outlined in Sec. 4.2.3.5 with $\bar{\mathbf{X}}_{\mathrm{BA}}$, the VisualSFM-produced point feature measurements, and the DD GNSS carrier phase time history used as inputs.

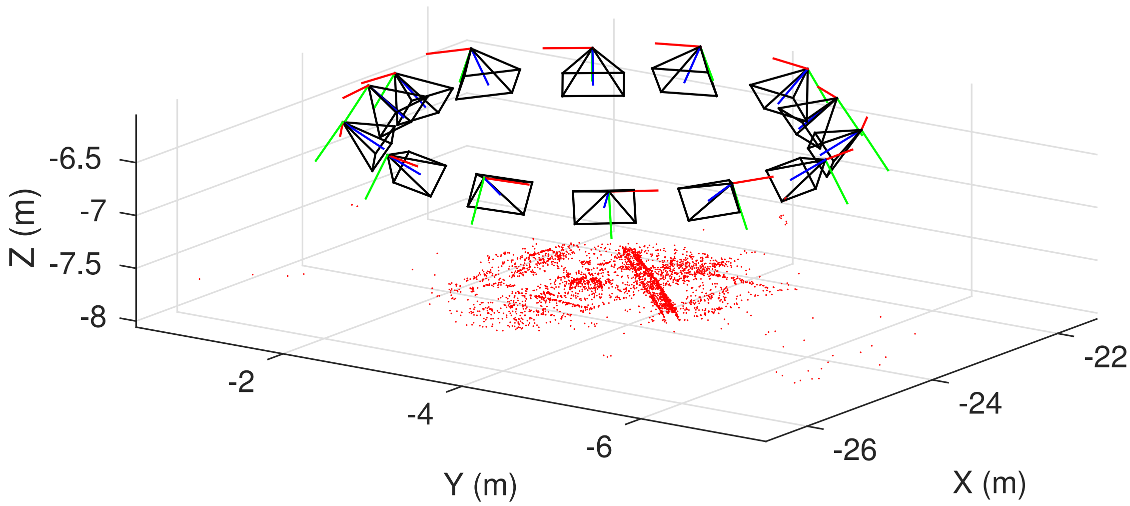

Figure 4.10: Using VISRTK, a three-dimensional, globally referenced, scene is reconstructed from real data collected using the low-cost platform illustrated in Fig. 4.8. The red dots represent the estimated position of the feature points identified in at least three of the 14 images taken around the scene, while the square-shaped objects above the points represent the estimated pose of the camera while each image was taken. The reference frame of the plot is in the East-North-Up (ENU) coordinate frame, with the origin translated to be that of the reference GNSS antenna, which was located east of the scene.

Output from VISRTK are the camera pose estimates, point feature position estimates, and carrier phase integer ambiguity estimates.

4.6.2 Reconstruction Results

Figure 4.10 illustrates the results of VISRTK using measurements from all 14 frames of the data collected via the data collection procedure outlined in Sec. 4.6.1. The reconstructed scene illustrates the estimated pose of all 14 cameras and the so-called "sparse point cloud" of estimated feature point positions, in the globally-referenced East-North-Up (ENU) reference frame. The metal pipe, sewer grate, and the GPS patch antenna which are visible in the scene (see Fig. 4.9) are all apparent in the sparse point cloud. The next few subsections will further analyze this VISRTK solution in terms of (1) it's ability to speed carrier phase ambiguity resolution as compared to standalone CDGNSS and (2) in terms of its absolute accuracy.

4.6.2.1 TAR Improvement

Figure 4.11 compares the ASR of a VISRTK solution computed on real data as compared to that of (1) a standalone CDGNSS solution and (2) a standalone CDGNSS solution aided with an centimeter-accurate antenna motion profile prior. VISRTK was able successfully resolve the ambiguities when computing a solution on behalf of 10 (or more) epochs of data (dashed orange trace). CDGNSS, in comparison required 11 epochs of data to do the same. This improvement was not as significant as the improvement seen with the simulated data in Fig. 4.7, when the VISRTK TAR neared that of a solution computed a perfect motion profile, likely due to incorrectly identified point features in the real data, which loosened the accuracy of the relative motion profile provided from the image measurements.

4.6.2.2 Jumpstart Improvement

This section analyzes the ASR improvement that comes when performing jumpstart VISRTK on behalf of the real data collected using the procedure outlined in Sec. 4.6.1. Figure 4.12 illustrates the Jumpstart VISRTK scene reconstruction in which 20 of the point features (denoted as large blue points) had position priors. The positions of these 20 point features were not exactly known, but their positions were first approximated to millimeter accuracy via a VISRTK solution computed on behalf of all 14 epochs of measurements. Figure 4.13 illustrates the ASR results as

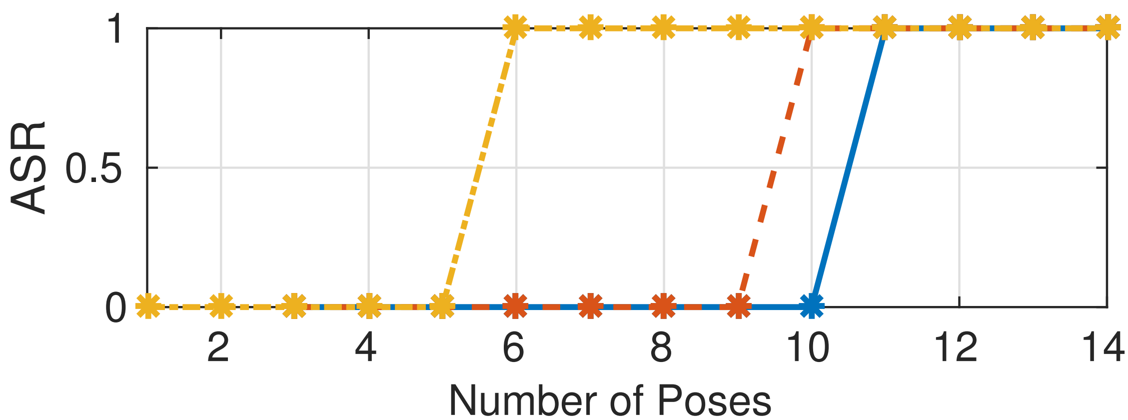

Figure 4.11: Plot comparing the VISRTK ASR (orange dashed trace), the standalone CDGNSS ASR (blue solid trace), and the CDGNSS ASR given a precise motion profile (yellow dash-dotted trace) as a function of the number of measurement epochs used in the solution. All were computed on the basis of the real data collected using the procedure outlined in Sec. 4.6.1. The constraint offered by the addition of feature point measurements enables faster ambiguity resolution for VISRTK as compared to standalone CDGNSS, but not as fast as that facilitated by a perfect motion profile prior.

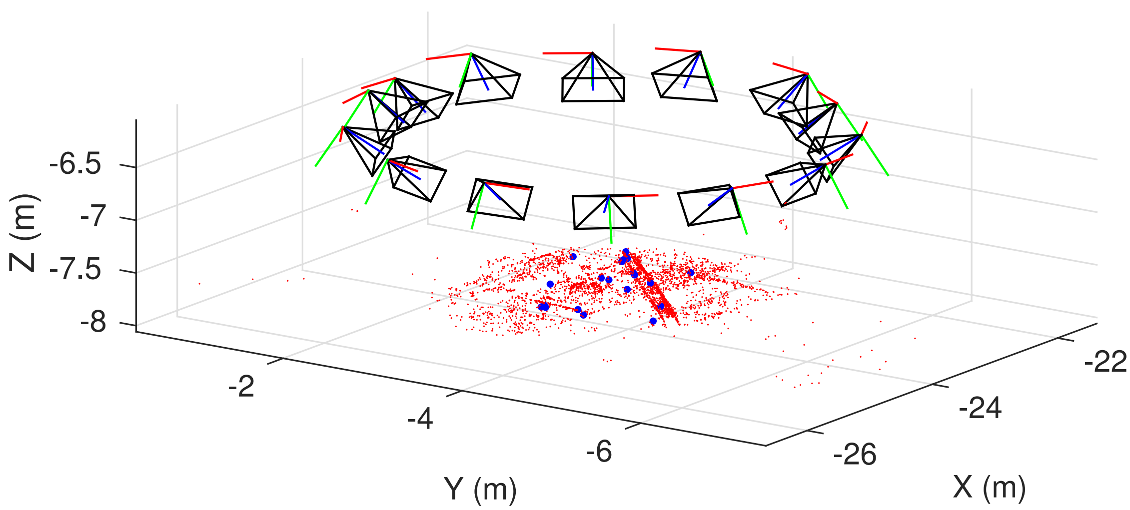

Figure 4.12: A 3D reconstruction using Jumpstart VISRTK solution computed on the basis of real data collecting using the procedure outlined in Sec. 4.6.1. The 20 points in blue are those for which prior information on their position is available to the VISRTK algorithm while the points in red are those for which no prior is available.

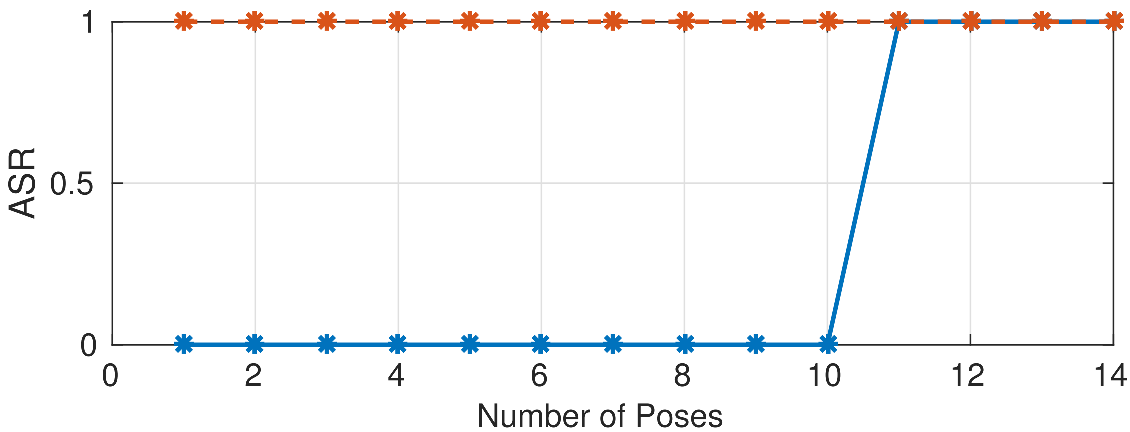

Figure 4.13: Plot comparing the VISRTK ASR (orange dashed trace) and the standalone CDGNSS ASR (blue solid trace) as a function of the number of measurement epochs used in the solution. Both were computed on the basis of real data, collected using the procedure outlined in Sec. 4.6.1. Centimeter-accurate positional priors on the 20 points illustrated in blue in Fig. 4.12 were used by Jumpstart VISRTK to enable instantaneous ambiguity resolution as depicted by the VISRTK ASR trace.

compared to a standalone CDGNSS solution. As with the simulated data, Jumpstart VISRTK facilitates instantaneous ambiguity resolution. This result is significant. It demonstrates that a low-cost GNSS antenna and a smartphone-grade camera can be used to remove one of the largest barriers to mass-market centimeter-accurate positioning today: convergence time. With only a single image and at least 4 premapped feature points, instantaneous ambiguity resolution is achievable.

4.6.2.3 Accuracy

This section analyzes the accuracy of VISRTK when applied to the real data collected using the procedure outlined in Sec. 4.6.1. Figure 4.14 illustrates the metric accurate dense reconstruction of the scene illustrated in Fig. 4.9.

Figure 4.14: A 3-dimensional metric-accurate dense reconstruction of the scene illustrated in Fig. 4.9. Dense reconstruction was performed on the output of the VISRTK-produced pose and sparse point reconstruction illustrated in Fig. 4.10, with the goal of using dense reconstruction to "add" more points to clearly locate the center of the GNSS antenna in the scene. The highlighted point in the yellow bubble denotes the VISRTK+Dense Reconstruction-estimated position of the center of the surface of the GNSS antenna, which will be compared against the surveyed location of the antenna to evaluate the VISRTK reconstruction accuracy.

Table 4.2: GNSS Antenna Position as computed using VISRTK+MVS and CDGNSS (in meters)

Position	East	North	Up
VISRTK+MVS	-24.280	-3.722	-7.438
CDGNSS	-24.278	-3.721	-7.440
Difference	-0.002	-0.001	0.002
Expected Std.	0.004	0.008	0.005

Dense reconstruction, also known as multi-view stereo (MVS), is a procedure which takes the original set of images and estimated camera poses and reconstructs a dense point cloud representation of the scene [138, 139]. Dense reconstruction was performed after the VISRTK solution using VisualSFM [135] using the original image files and the VISRTK-estimated camera poses. VisualSFM performed the dense reconstruction using an underlying MVS toolchain known as Clustering Views for Multi-View Stereo (CMVS) [138].

As with the sparse point cloud of Fig. 4.10, the dense point cloud produced from dense reconstruction was globally-referenced to the ENU reference frame. A point, which was on the surface and in the center of the GNSS antenna pictured in the scene, was selected, revealing its ENU coordinates (see Fig. 4.14). To evaluate the accuracy of the VISRTK+MVS solution, this coordinate was compared to the surveyed location of the antenna, determined from a CDGNSS solution computed on behalf of the earlier IF data collected from the antenna (see Sec. 4.6.1, step 7). Table 4.2 shows the results. For the CDGNSS surveyed coordinate shown in the table, the antenna calibration values published by the National Geodetic Survey [140] were used to translate the surveyed position from that of the antenna's phase center to

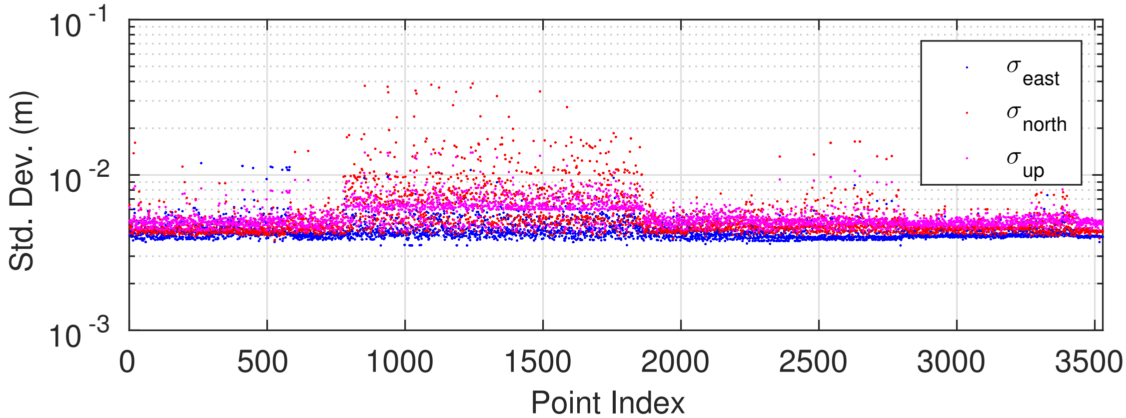

Figure 4.15: VISRTK 3-dimensional point position estimate errors for the approximately 3500 points shown in Fig. 4.10. A majority of the errors are in the sub-centimeter range.

that of the center of its top surface. As such, both coordinates (VISRTK+MVS and CDGNSS) now refer to the position of the center of the antenna's top surface.

The difference between the VISRTK+MVS solution and the phase-center-compensated CDGNSS solution is on the millimeter-level. This accuracy falls well within the VISRTK-estimator's expected accuracy for points which fall on the top surface of the antenna, as shown in the last column of Table 4.1. Fig. 4.15 shows that the per-dimension error standard deviation of most point features is on the sub-centimeter-level. Consequently, since the VISRTK estimator's expected point feature accuracy matches the empirical accuracy, there is some reason to believe that the estimator's expected pose accuracy can also be trusted. Figure 4.16 shows the attitude error and positional error standard deviation for each camera pose. The expected camera position accuracy is on the sub-centimeter level, while the camera attitude accuracy is on the sub-degree level.

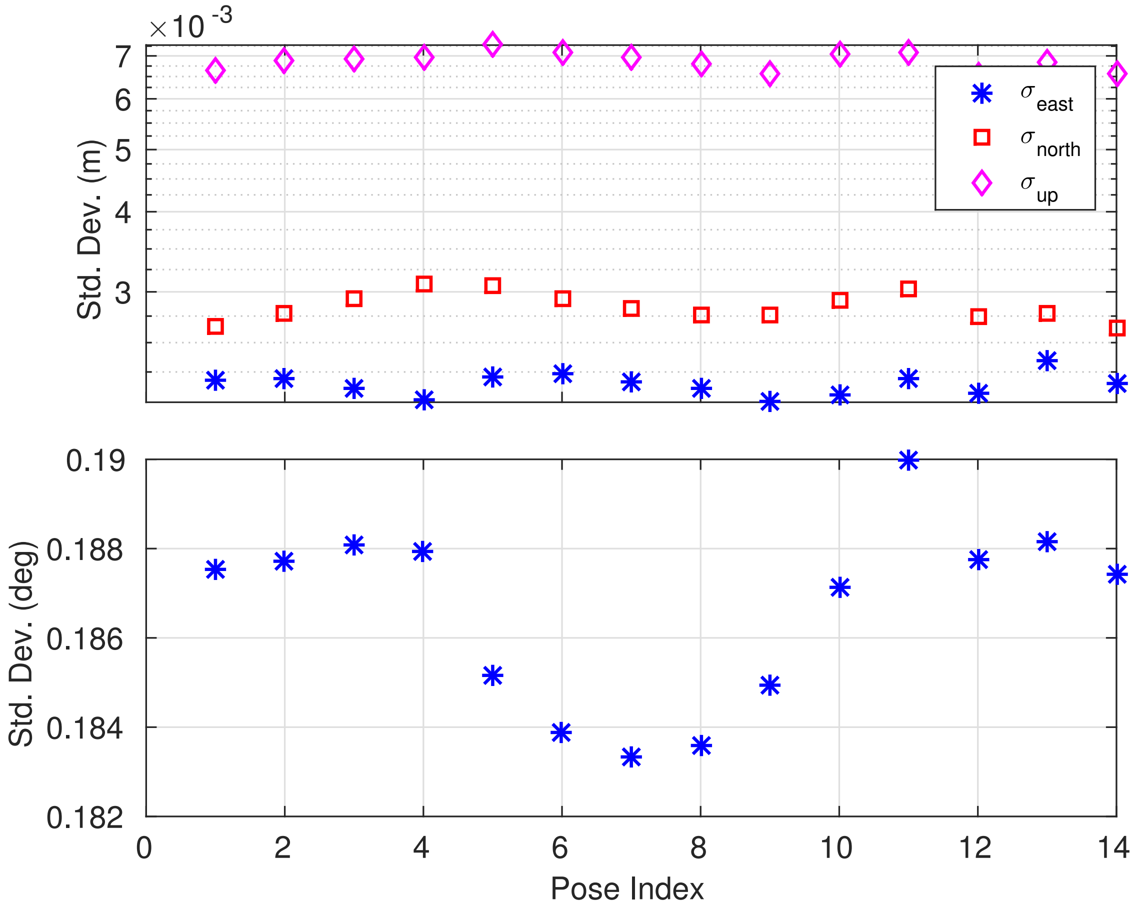

Figure 4.16: VISRTK 3-dimensional camera position (top panel) and attitude (bottom panel) estimate errors for the 15 camera poses illustrated in Fig. 4.10. Camera positional errors are in the sub-centimeter range and attitude errors are in the sub-degree range.

Table 4.3: Simulated Data Parameters

$\sigma_{p_i^j}$	$\sigma_{\phi_i,\mathrm{B}}$	$\sigma_{\phi_i,\mathrm{A}}$	$\mathbf{x}_{\mathcal{C}_i}^{\mathcal{A}}$	Point Density	Num. SVs	Time Between Epochs
1 pixel	8 mm	2 mm	[0, -.05, -.015] m	0.3 points/m^2	11	30 s

4.6.3 VISRTK Comparison to Existing Frameworks

This section compares, in simulation, the solution accuracy of the VISRTK tight-coupled framework to that of the existing similarity transform and loosely-coupled frameworks. Fig. 4.17 shows the VISRTK-reconstructed result of the simulated scene, whereby 17 cameras are positioned 10 meters from the outside of a 20-meter-radius cylinder of point features, collecting a single epoch of feature point and GNSS carrier phase measurements at each location. The cameras are purposely simulated to not complete the circle around the cylinder in order to analyze solution accuracy under scenario in which the advantages that come from loop closure [3, 4] are not attainable. Such scenarios are typical as there are many cases in which a receiver is exploring and does not wish to return to locations to which it has already been. One of the advantages of VISRTK and also the loosely-coupled approach is that they integrate the GNSS measurements into their estimators' cost functions at a deep enough level to prevent drift and reduce the necessity of loop closure. In contrast, as the results of this section will reveal, the similarity transform framework is unable to take advantage of GNSS measurements in a way that prevents drift in the absence of loop closure.

The full simulation parameters are shown in Table 4.3.

Figures 4.18 4.20 compare the camera pose and point feature position ac-

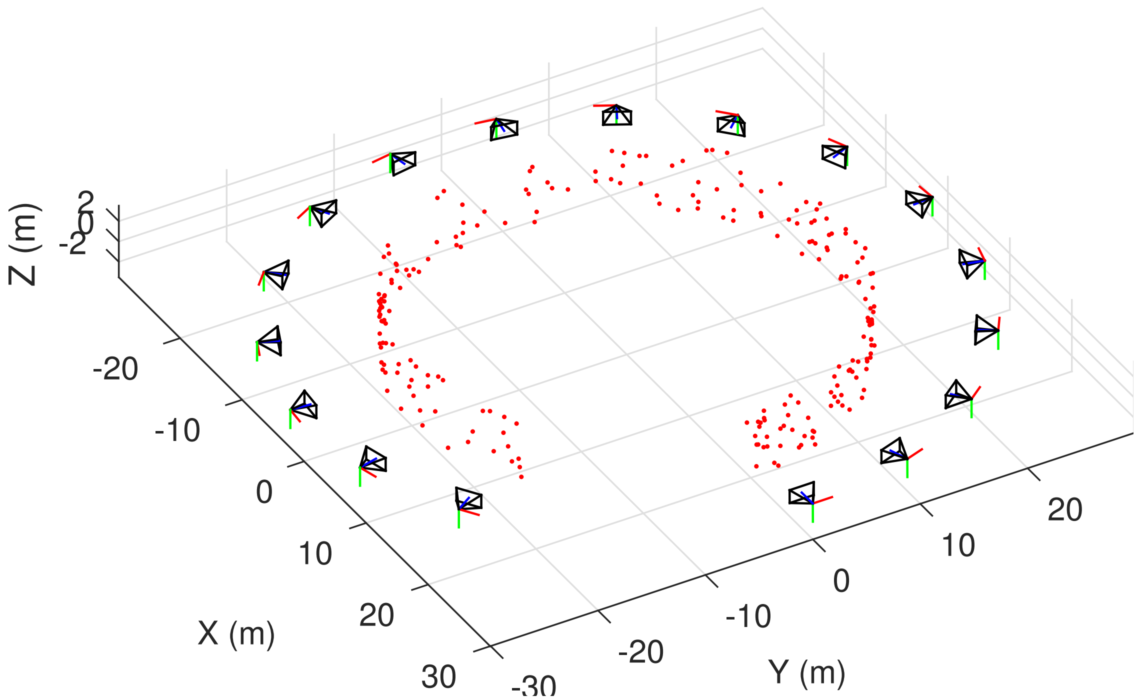

Figure 4.17: A VISRTK-produced 3-dimensional scene reconstruction of a simulated scene, whereby 17 cameras are positioned 10 meters from the outside of a 20-meter-radius cylinder of point features. A single epoch of feature point and GNSS carrier phase measurements at each camera pose were provided to the estimator for reconstruction. The circle of cameras was purposefully left "unclosed" to enable the analysis of the accuracy of the VISRTK framework (and of the other two existing frameworks presented in Sec. 4.3) under a scenario in which the advantages that come from loop closure [3, 4] are not realized.

curacy of the VISRTK and loosely coupled frameworks to that of the similarity transform framework. The number of GNSS signals are enough to guarantee near-instantaneous integer ambiguity resolution for both the VISRTK framework and for the standalone CDGNSS algorithm that computes, from the carrier phase measurements, centimeter-accurate position measurements for the loosely coupled framework. Consequently, as the carrier phase measurements provided to the CDGNSS algorithm are a near-linear function of its state—provided that the integer ambiguities are resolved correctly—the information provided to the loosely coupled estimator in the form of CDGNSS-derived position estimates is nearly equivalent to that provided by the carrier phase measurements to the VISRTK estimator. Therefore, the results of VISRTK and the loosely-coupled framework are nearly equivalent, and as such, the estimates shown in the top panels of Figs. 4.18 4.20 represent the accuracy of both the VISRTK and loosely coupled frameworks. The bottom panels represent the accuracy of the similarity transform framework.

It is clear from the figures that the VISRTK and loosely coupled frameworks are superior to that of the similarity transform. The similarity transform solution experiences drift in all three of its estimates: camera position, attitude, and point feature position. This drift is especially noticeable for poses and points on the "outside edges" of the trajectory, e.g., in camera pose estimates with no neighboring poses (pose indices 1 and 17) and in the position errors of the point features seen by these cameras (point indices less than 50 and greater than 200).

4.7 Conclusion

This chapter presented and analyzed an estimation framework that combines monocular camera images with GNSS carrier phase measurements for fast, robust,

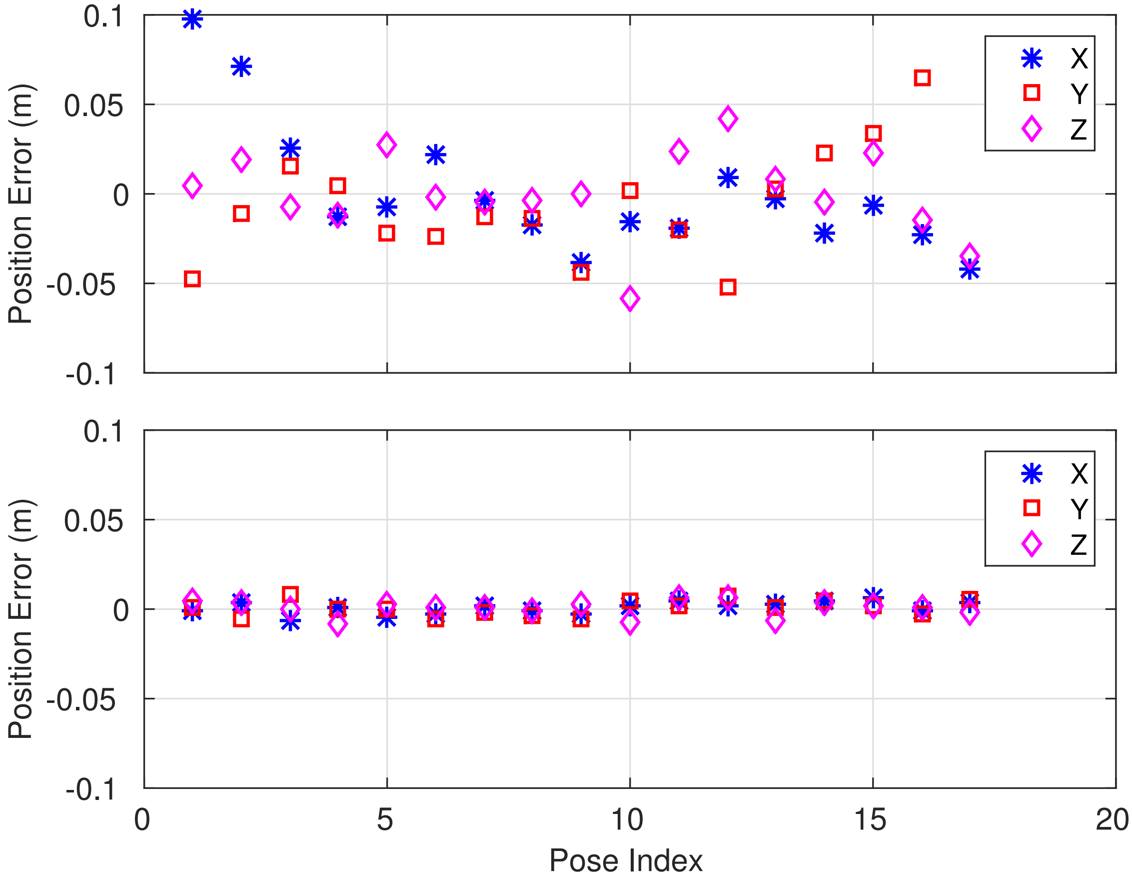

Figure 4.18: Plot comparing the camera position errors of the similarity transform framework (top panel) to that of the VISRTK and loosely coupled architectures (bottom subplot). Results were computed on the basis of simulated measurements, characterized in Table 4.3. The VISRTK reconstructed scene is illustrated in Fig. 4.17. It is clear that the positional errors are larger for the similarity transform framework as the framework does not couple GNSS position or carrier phase measurements into the same least squares cost function as the feature point measurements and is thus sub-optimal as compared to the other two frameworks. Significant error drift can be seen in the similarity transform solution, particularly on the outer poses, as there is not way for the GNSS measurements to be used to correct relative errors present in the vision-only BA solution.

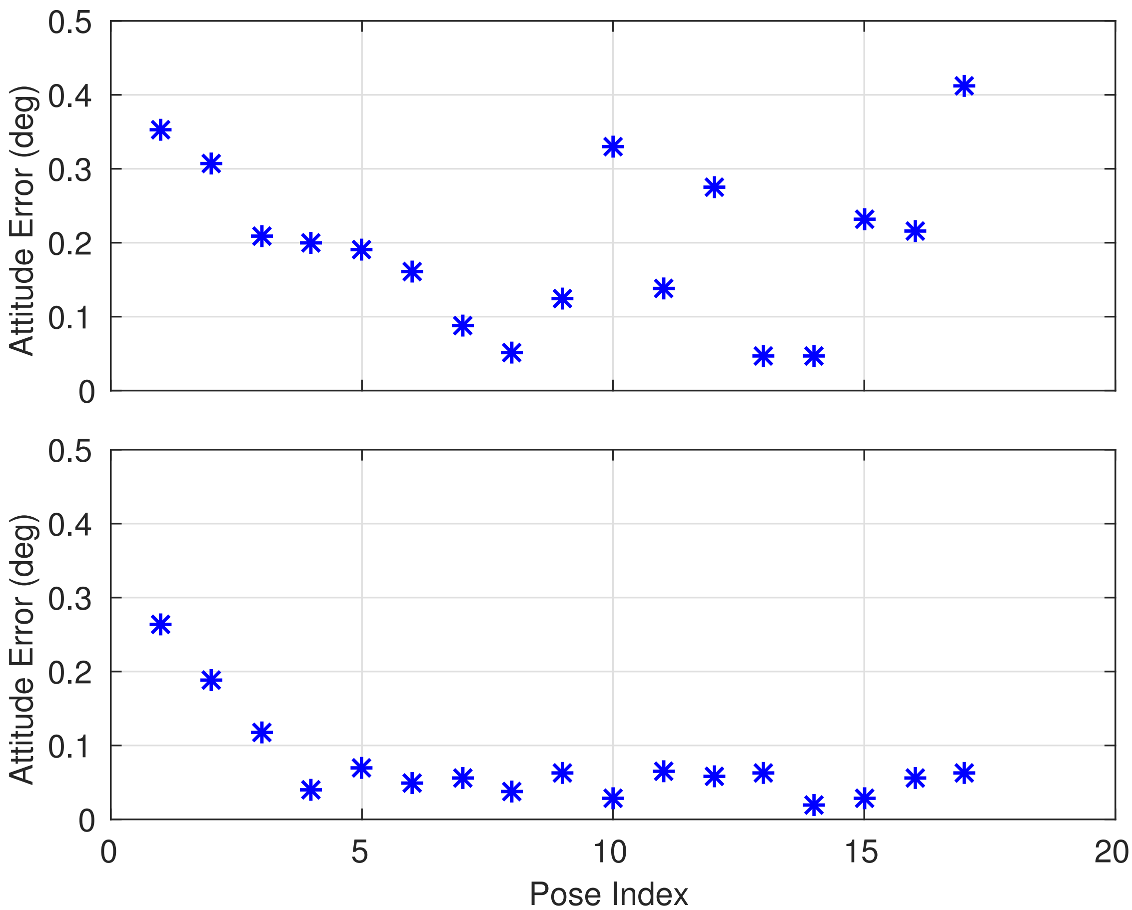

Figure 4.19: Plot comparing the camera attitude errors of the similarity transform framework (top panel) to that of the VISRTK and loosely coupled architectures (bottom subplot). It is clear that the attitude errors are larger for the similarity transform framework than for the other frameworks.

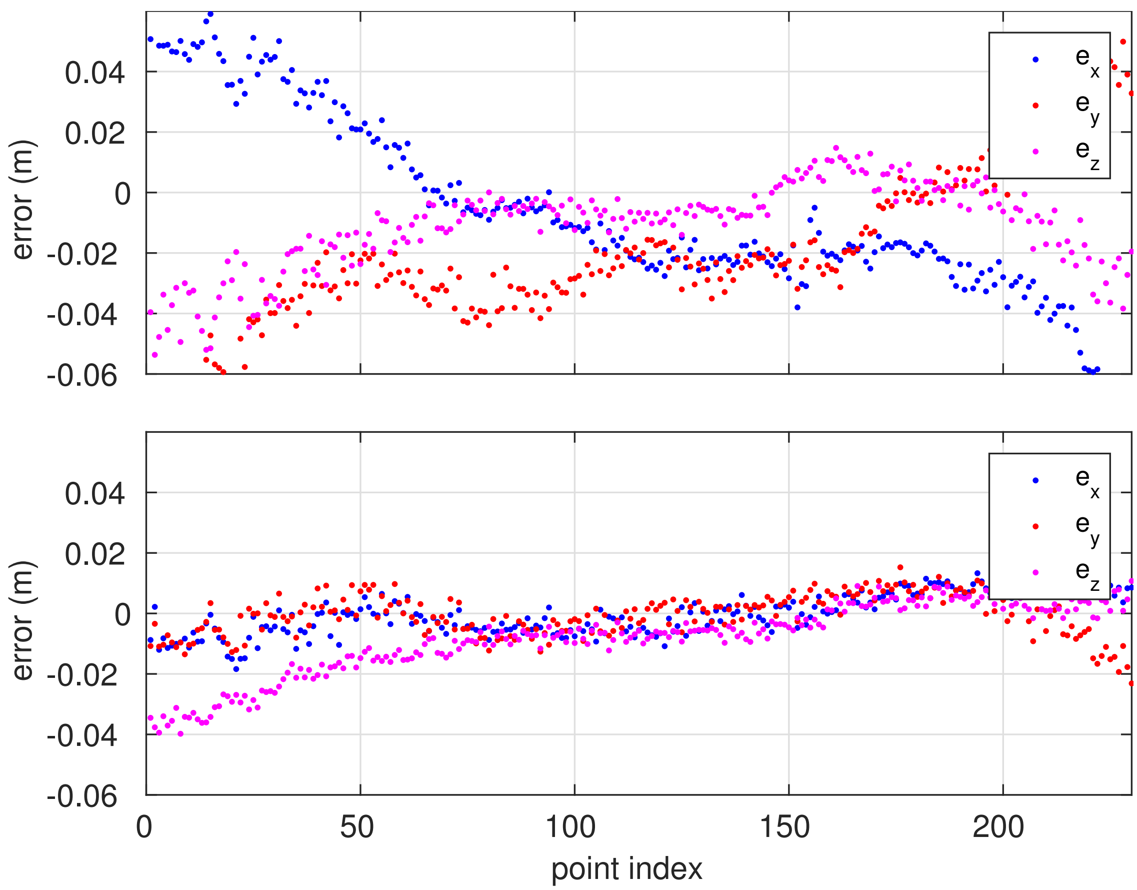

Figure 4.20: Plot comparing the point feature position errors of the similarity transform framework (top panel) to that of the VISRTK and loosely coupled architectures (bottom subplot). It is clear that the position errors are larger for the similarity transform framework than for the other frameworks.

precise, and globally-referenced mobile device position and orientation (pose) determination. The framework, which is termed VISRTK after the common industry synonym for CDGNSS, Real Time Kinematic (RTK), augments the bundle-adjustment-(BA-)-based structure from motion (SFM) algorithm with carrier phase differential GNSS (CDGNSS) algorithm in a way that preserves both the sparseness of the Jacobian matrix in BA and the integer structure of the ambiguities in CDGNSS. In doing so, the proposed fused framework is able to exploit the computational efficiency of BA and the precision of CDGNSS to efficiently and accurately determine the pose of the mobile device in a global reference frame. Comparisons to existing approaches which combine GNSS and camera measurements for globally-referenced pose determination reveal that these do not combine measurements as tightly nor optimally as the proposed approach, resulting in the proposed approach having a faster, more robust, and more accurate solution. Empirical simulation results and results using real data in the form of images and GNSS carrier phase measurements captured from a low-cost GNSS receiver and smartphone platform show that the proposed estimation framework (1) achieves centimeter- and sub-degree-accurate pose estimates, (2) leads to faster resolution of the CDGNSS integer ambiguities as compared to standalone CDGNSS, and (3) is able to use prior information from previously-localized point features for instantaneous CDGNSS integer-ambiguity resolution.

Chapter 5

Conclusion

The uses of centimeter-accurate positioning in the mass market are becoming increasingly numerous. It is anticipated that a device with low-cost centimeter-accurate positioning and sub-degree accurate orientation capabilities will usher in a host of new and useful applications to the commercial and consumer industries. In the wireless communication industry, the ability to use GNSS measurements to obtain precise antenna position and orientation information could benefit V2V and millimeter wave communication where centimeter-accurate position information can facilitate high gain, narrow beamwidth communication links that require minimal feedback overhead. In another wireless application, two rigidly attached GNSS antennas could be used to provide sub-degree heading determination of cellular basestation antennas to perform precise antenna alignment and maximize coverage efficiency. Furthermore, a mobile device with robust centimeter positioning capability could be used in the entertainment industry for geo-referenced augmented and virtual reality, in the construction industry for low-cost surveying and 3-D map making, and in the automotive industry to provide guidance, navigation, and collision avoidance of autonomous and semi-autonomous vehicles. This dissertation defends the following thesis statement:

> *Centimeter-accurate GNSS positioning on low-cost mobile platforms is achievable, but hard. These platforms, however, have certain intrinsic features that can be exploited to make the process easier.*

The following section offers a summary of the contributions proving this thesis statement.

5.1 Summary

- Chapter 2 presents a carrier phase reconstruction technique to enable low-power centimeter-accurate positioning on mobile devices is developed and analyzed. Carrier-phase positioning solutions currently require continuous, non-duty-cycled signal phase measurements. Accurate carrier phase reconstruction permits the aggressive duty cycling of phase measurements, significantly decreasing the overall energy consumption of existing solutions.

- Chapter 3 demonstrates for the first time that a centimeter-accurate positioning solution is possible based on data collected from the internal antenna of a smartphone. It is shown that the primary impediment to performing CDGNSS positioning on low-cost mobile platforms lies not in the commodity GNSS chipset within the phone, but instead in the antenna, whose chief failing is its poor multipath suppression [2]. It is demonstrated wavelength-scale random antenna motion can be used to substantially improve the CDGNSS initialization time as compared to keeping the antenna stationary.

- Chapter 4 presents a joint image and GNSS measurement estimation framework that fuses smartphone camera measurements with differential GNSS carrier phase measurements to reduce the CDGNSS initialization times and estimate to centimeter- and sub-degree-accuracy the pose of consumer mobile platforms.

5.2 Future Work

This section outlines a number of future research directions that build upon this dissertations contributions.

5.2.1 VISRTK Observability Analysis

It is well known that a standalone CDGNSS solution computed on the basis of carrier phase measurements only (no pseudorange measurements or position prior information) requires at least two measurement epochs to be observable [20]. However, with a position prior, the problem becomes observable even after a single epoch of data. Furthermore, depending on the accuracy of this position prior and the accuracy and quantity of the carrier phase measurements, these ambiguities become not only observable, but estimable to a high degree of certainty as well. High ambiguity estimability facilitates what is known as instantaneous or single-epoch ambiguity resolution within the GNSS community [27, 141, 142], where a centimeter-accurate CDGNSS position can be computed instantly after only a single epoch of measurements. In chapter 4, a method called "jumpstart," was explained and analyzed to show that, instead of a position prior on the GNSS antenna, prior information regarding the position of identified point features in images taken by a smartphone or other camera fixed to the same platform as the GNSS antenna, such prior information could be used to enable instantaneous ambiguity resolution when properly considered within the VISRTK framework.

In the earlier analysis of Chapter 4, the number of point features with positional priors was 50, likely exceeding the absolute minimum required. Future work could perform a theoretical observability analysis of the VISRTK framework to identify the minimum number of point feature priors required for full state observability assuming (1) a single epoch and (2) multiple epochs of phase and image measurements. Prior work in the computer vision community has shown that at least four points are required for camera pose observability when no other measurements, e.g., phase measurements, are present [143, 144]. With the added constraint of phase measurements, even with added integer ambiguity needing to be resolved, this minimum of four points could very likely be reduced.

5.2.2 Phase Outlier and Cycle Slip Detection and Correction

The combination of image measurement with GNSS carrier phase measurements in the tightly coupled VISRTK framework discussed in Chapter 4 introduces many more constraints into the framework's centralized batch estimator. These additional constraints were used, as described in the chapter, to reduce the time to ambiguity resolution and, consequently to a centimeter-accurate position fix as compared to standalone CDGNSS. As it turns out, these constraints can also be used to detect and correct for abnormalities in the carrier phase measurements themselves, thereby preventing these abnormalities from negatively impacting the resulting state estimate. In particular, future work would develop and analyze techniques to perform cycle slip detection and correction and phase error outlier detection within the VISRTK framework. Such work future work could build upon prior work in the area of tightly coupled GNSS/INS systems [145–147].

5.2.3 Receiver versus Reference Network Tradeoff Analysis

The analysis performed in this dissertation has assumed the use of single frequency GNSS antennas due to their low cost and current availability in mass market mobile devices. However, the added signals that dual-frequency GNSS would bring would improve the accuracy, robustness, and ambiguity resolution time of devices employing CDGNSS. Dual frequencies would also enable the estimation of the double-differenced ionospheric errors [148], enabling the same ambiguity resolution time with a denser reference receiver network, all else equal. However, the requirement of a second antenna and front end required to produce dual-frequency GNSS measurements would add cost, even if only a few cents, to every device produced. As the number of devices increases, there becomes a point whereby it may be more beneficial to shift the cost to the network by densifying the reference network. A denser network would ensure that single frequency devices can achieve the same convergence time of a dual frequency device with a sparser network. Future work would analyze these trade-offs, considering the ambiguity resolution performance, robustness, and accuracy improvements that dual frequency would enable while increasing device cost. Such analysis could be performed not under the assumption of point-to-point CDGNSS, as was considered herein, but also Network RTK and PPP-RTK techniques that enable sparser reference stations as compared to standalone CDGNSS without giving up on convergence time [149–151].

Bibliography

[1] D. L. Warren and J. F. Raquet, "Broadcast vs. precise GPS ephemerides: a historical perspective," *GPS Solutions*, vol. 7, no. 3, pp. 151–156, 2003.

[2] K. M. Pesyna, Jr., R. W. Heath, Jr., and T. E. Humphreys, "Centimeter positioning with a smartphone-quality GNSS antenna," in *Proceedings of the ION GNSS+ Meeting*, 2014.

[3] E. Eade and T. Drummond, "Unified loop closing and recovery for real time monocular SLAM.," in *BMVC*, vol. 13, p. 136, Citeseer, 2008.

[4] C. Stachniss, D. Hähnel, and W. Burgard, "Exploration with active loop-closing for fastslam," in *Intelligent Robots and Systems, 2004.(IROS 2004). Proceedings. 2004 IEEE/RSJ International Conference on*, vol. 2, pp. 1505–1510, IEEE, 2004.

[5] D. Jewell, "Trends in GPS/PNT user equipment," 2013. `http://gpsworld.com/trends-in-gpspnt-user-equipment/`.

[6] H. Dediu, "Invaluable." `http://www.asymco.com/2014/03/18/invaluable/`, 2014.

[7] R. B. Langley, "Innovation: Mobile phone GPS antennas," pp. 29–35, Feb. 2010. GPS World.

[8] W. Ballantyne, G. Turetsky, G. Slimak, and J. Shewfelt, "Achieving low energy-per-fix with A-GPS cellular phones," in *Proceedings of the ION GPS Meeting*, pp. 2234–2242, 2001.

[9] K. Alexander, "U.S. GPS program and policy update," in *26th SBAS International Working Group*, National Coordination Office, Feb. 2014.

[10] Department of Defense, "Global Positioning System Standard Positioning Service performance standard," tech. rep., Assistant secretary of defense for command, control, communications, and intelligence, 2008.

[11] WAAS Test Team, "Wide-Area Augmentation System performance analysis report," tech. rep., Federal Aviation Administration, January 2014.

[12] P. Misra and P. Enge, *Global Positioning System: Signals, Measurements, and Performance.* Lincoln, Massachusetts: Ganga-Jumana Press, revised second ed., 2012.

[13] J. Betz and K. Kolodziejski, "Generalized theory of code tracking with an early-late discriminator part i: lower bound and coherent processing," *IEEE Transactions on Aerospace and Electronic Systems*, vol. 45, no. 4, pp. 1538–1556, 2009.

[14] K. Dixon, "Starfire: A global SBAS for sub-decimeter precise point positioning," in *Proceedings of the ION GNSS Meeting*, pp. 26–29, 2006.

[15] P. Teunissen, P. De Jonge, and C. Tiberius, "The LAMBDA method for fast GPS surveying," in *Proceedings of International Symposium on GPS Technology Applications*, vol. 29, (Bucharest, Romania), pp. 203–210, Union of Romanian Geodesy, Sept. 1995.

[16] C. Counselman and S. Gourevitch, "Miniature interferometer terminals for earth surveying: ambiguity and multipath with global positioning system," *IEEE Transactions on Geoscience and Remote Sensing*, no. 4, pp. 244–252, 1981.

[17] C. C. Counselman III, R. I. Abbot, S. A. Gourevitch, R. W. King, and A. R. Paradis, "Centimeter-level relative positioning with GPS," *Journal of Surveying Engineering*, vol. 109, no. 2, pp. 81–89, 1983.

[18] P. Henkel, *Reliable carrier phase positioning.* PhD thesis, Munchen, Techn. Univ., Diss., 2010, 2010.

[19] B. W. Parkinson and P. K. Enge, *Global Positioning System: Theory and Applications*, vol. 2, ch. 1: Differential GPS, pp. 3–50. Washington, D.C.: American Institute of Aeronautics and Astronautics, 1996.

[20] P. Teunissen, P. De Jonge, and C. Tiberius, "Performance of the LAMBDA method for fast GPS ambiguity resolution," *Navigation, Journal of the Institute of Navigation*, vol. 44, no. 3, pp. 373–383, 1997.

[21] M. Ge, G. Gendt, M. Rothacher, C. Shi, and J. Liu, "Resolution of GPS carrier-phase ambiguities in precise point positioning (ppp) with daily observations," *Journal of Geodesy*, vol. 82, no. 7, pp. 389–399, 2008.

[22] D. Laurichesse and F. Mercier, "Integer ambiguity resolution on undifferenced GPS phase measurements and its application to ppp," in *Proceedings of the 20th International Technical Meeting of the Satellite Division of The Institute of Navigation (ION GNSS 2007)*, pp. 839–848, 2001.

[23] Broadcom, *Product Brief: BCM4750 AGPS chip*, 2007.

[24] F. van Diggelen, "Who's your daddy? Why GPS will continue to dominate consumer GNSS," *Inside GNSS*, pp. 30–41, March/April 2014.

[25] E. Gakstatter, "Centimeter-level RTK accuracy more and more available for less and less," 2014. GPS World.

[26] Qualcomm, "Gps and glonass: dual-core" location for your phone," Dec. 2011. http://www.qualcomm.com/media/blog/2011/12/15/gps-and-glonass-dual-core-location-your-phone.

[27] G. Giorgi, P. J. Teunissen, S. Verhagen, and P. J. Buist, "Instantaneous ambiguity resolution in global-navigation-satellite-system-based attitude determination applications: A multivariate constrained approach," *Journal of Guidance, Control, and Dynamics*, vol. 35, no. 1, pp. 51–67, 2012.

[28] P. Teunissen, P. De Jonge, and C. Tiberius, "The least-squares ambiguity decorrelation adjustment: its performance on short GPS baselines and short observation spans," *Journal of geodesy*, vol. 71, no. 10, pp. 589–602, 1997.

[29] P. Teunissen, "Closed form expressions for the volume of the GPS ambiguity search spaces," *Artificial Satellites- Planetary Geodesy*, vol. 32, no. 1, pp. 5–20, 1997.

[30] T. E. Humphreys, K. M. Pesyna, Jr., F. van Diggelen, and S. Podshivalov, "On the feasibility of centimeter-accurate positioning via a smartphone's antenna and GNSS chip," in *Proceedings of the ION GNSS+ Meeting*, 2015. (In preparation.).

[31] D. P. Shepard, K. M. Pesyna, Jr., and T. E. Humphreys, "Precise augmented reality enabled by carrier-phase differential GPS," in *Proceedings of the ION GNSS Meeting*, (Nashville, Tennessee), Institute of Navigation, 2012.

[32] D. Shepard, "Fusion of carrier-phase differential GPS, bundle-adjustment-based visual slam, and inertial navigation for precisely and globally-registered augmented reality," Master's thesis, The University of Texas at Austin, May 2013.

[33] K. M. Pesyna, Jr., Z. M. Kassas, R. W. Heath, Jr., and T. E. Humphreys, "A phase-reconstruction technique for low-power centimeter-accurate mobile positioning," *IEEE Transactions on Signal Processing*, vol. 62, pp. 2595–2610, May 2014.

[34] K. M. Pesyna, Jr., Z. M. Kassas, and T. E. Humphreys, "Constructing a continuous phase time history from TDMA signals for opportunistic navigation," in *Proceedings of the IEEE/ION PLANS Meeting*, pp. 1209–1220, April 2012.

[35] K. M. Pesyna, Jr., T. Novlan, C. Zhang, R. W. Heath, Jr., and T. E. Humphreys, "Exploiting antenna motion for faster initialization of centimeter-accurate GNSS positioning with low-cost antennas," *IEEE Transactions on Aerospace and Electronic Systems*, 2015. (Submitted for review.).

[36] K. M. Pesyna, Jr, R. W. Heath, Jr., and T. E. Humphreys, "Accuracy in the palm of your hand: Centimeter positioning with a smartphone-quality GNSS antenna," *GPS World*, vol. 26, pp. 16–31, Feb. 2015.

[37] K. M. Pesyna, Jr., D. P. Shepard, R. W. Heath, Jr., and T. E. Humphreys, "VISRTK: Fusion of camera and GNSS carrier phase measurements for fast, robust, precise, and globally-referenced mobile device pose determination," *IEEE Transactions on Signal Processing*, 2015. (In preparation.).

[38] K. M. Pesyna, Jr., R. W. Heath, Jr., and T. E. Humphreys, "Precision limits of low-energy GNSS receivers," in *Proceedings of the ION GNSS+ Meeting*, (Nashville, Tennessee), Institute of Navigation, 2013.

[39] K. M. Pesyna, Jr., K. D. Wesson, R. W. Heath, Jr., and T. E. Humphreys, "Extending the reach of GPS-assisted femtocell synchronization and localization through tightly-coupled opportunistic navigation," in *IEEE GLOBECOM Workshop*, 2011.

[40] K. M. Pesyna Jr., Z. M. Kassas, J. A. Bhatti, and T. E. Humphreys, "Tightly-coupled opportunistic navigation for deep urban and indoor positioning," in *Proceedings of the ION GNSS Meeting*, (Portland, Oregon), Institute of Navigation, 2011.

[41] K. D. Wesson, K. M. Pesyna, Jr., J. A. Bhatti, and T. E. Humphreys, "Opportunistic frequency stability transfer for extending the coherence time of GNSS receiver clocks," in *Proceedings of the ION GNSS Meeting*, (Portland, Oregon), Institute of Navigation, 2010.

[42] D. P. Shepard, T. E. Humphreys, K. M. Pesyna, Jr., and J. A. Bhatti, "A system and method for using global navigation satellite system (GNSS) navigation and visual navigation to recover absolute position and attitude without any prior association of visual features with known coordinates," Feb. 2014. US Patent filed on Feb., 3, 2014.

[43] u-Blox, *Datasheet: NE0-7 GPS/GNSS Module*, 2013.

[44] M. Psiaki, “Kalman filtering and smoothing to estimate real-valued states and integer constants,” *Journal of Guidance, Control, and Dynamics*, vol. 33, pp. 1404–1417, Sept.-Oct. 2010.

[45] S. Mohiuddin and M. L. Psiaki, “High-altitude satellite relative navigation using carrier-phase differential global positioning system techniques,” *Journal of Guidance, Control, and Dynamics*, vol. 30, pp. 1628–1639, Sept.-Oct. 2007.

[46] T. Bell, “Automatic tractor guidance using carrier-phase differential GPS,” *Computers and electronics in agriculture*, vol. 25, no. 1, pp. 53–66, 2000.

[47] J. Farrell, T. Givargis, and M. Barth, “Real-time differential carrier phase GPS-aided INS,” *Control Systems Technology, IEEE Transactions on*, vol. 8, no. 4, pp. 709–721, 2000.

[48] K. Alanen, L. Wirola, J. Käppi, and J. Syrjärinne, “Mobile rtk using low-cost GPS and internet-enabled wireless phones,” *Inside GNSS*, vol. 1, pp. 32–39, 2006.

[49] D. B. Cox and J. D. Brading, “Integration of lambda ambiguity resolution with kalman filter for relative navigation of spacecraft,” *Navigation, Journal of the Institute of Navigation*, vol. 47, no. 3, pp. 205–210, 2000.

[50] S. Mohiuddin and M. Psiaki, “Carrier-phase differential Global Positioning System navigation filter for high-altitude spacecraft,” *Journal of Guidance, Control, and Dynamics*, vol. 31, no. 4, pp. 801–814, 2008.

[51] K. Q. Chiang, M. L. Psiaki, S. P. Powell, R. J. Miceli, and B. W. O’Hanlon, “GPS-based attitude determination for a spinning rocket,” in *Proceedings of the ION GNSS Meeting*, (Nashville, Tennessee), pp. 2342–2350, Institute of Navigation, 2012.

[52] P. De Jonge and C. Tiberius, “The LAMBDA method for integer ambiguity estimation: implementation aspects,” *Publications of the Delft Geodetic Computing Centre, LGR-Series*, 1996.

[53] A. Hassibi and S. Boyd, “Integer parameter estimation in linear models with applications to GPS,” *IEEE Transactions on Signal Processing*, vol. 46, no. 11, pp. 2938–2952, 1998.

[54] B. Hassibi and H. Vikalo, “On the sphere-decoding algorithm I. Expected complexity,” *IEEE Transactions on Signal Processing*, vol. 53, no. 8, pp. 2806–2818, 2005.

[55] J. Jaldén and B. Ottersten, "On the complexity of sphere decoding in digital communications," *IEEE Transactions on Signal Processing*, vol. 53, no. 4, pp. 1474–1484, 2005.

[56] M. Pohst, "On the computation of lattice vectors of minimal length, successive minima and reduced bases with applications," *ACM SIGSAM Bulletin*, vol. 15, no. 1, pp. 37–44, 1981.

[57] M. Psiaki and S. Mohiuddin, "Modeling, analysis, and simulation of GPS carrier phase for spacecraft relative navigation," *Journal of Guidance Control and Dynamics*, vol. 30, no. 6, p. 1628, 2007.

[58] T. E. Humphreys, M. L. Psiaki, and P. M. Kintner, Jr., "Modeling the effects of ionospheric scintillation on GPS carrier phase tracking," *IEEE Transactions on Aerospace and Electronic Systems*, vol. 46, pp. 1624–1637, Oct. 2010.

[59] G. J. Bierman, *Factorization Methods for Discrete Sequential Estimation*. New York: Academic Press, 1977.

[60] G. Bierman, M. Belzer, J. Vandergraft, and D. Porter, "Maximum likelihood estimation using square root information filters," *IEEE Transactions on Automatic Control*, vol. 35, no. 12, pp. 1293–1298, 1990.

[61] R. G. Brown and P. Y. Hwang, *Introduction to Random Signals and Applied Kalman Filtering*. Wiley, 1997.

[62] M. L. Psiaki and H. Jung, "Extended Kalman filter methods for tracking weak GPS signals," in *Proceedings of the ION GPS Meeting*, (Portland, Oregon), pp. 2539–2553, Institute of Navigation, 2002.

[63] J. T. Curran, G. Lachapelle, and C. C. Murphy, "Improving the design of frequency lock loops for GNSS receivers," *IEEE Transactions on Aerospace and Electronic Systems*, vol. 48, no. 1, pp. 850–868, 2012.

[64] K. M. Pesyna, Jr. and T. E. Humphreys, "Cost analysis of square root information filtering and smoothing with a mixed real-integer state," *Whitepaper*, 2013. `http://radionavlab.ae.utexas.edu/reconstruction/`.

[65] E. Agrell, T. Eriksson, A. Vardy, and K. Zeger, "Closest point search in lattices," *IEEE Transactions on Information Theory*, vol. 48, no. 8, pp. 2201–2214, 2002.

[66] P. Teunissen, "An optimality property of the integer least-squares estimator," *Journal of Geodesy*, vol. 73, no. 11, pp. 587–593, 1999.

[67] A. Lenstra, H. Lenstra, and L. Lovász, "Factoring polynomials with rational coefficients," *Mathematische Annalen*, vol. 261, no. 4, pp. 515–534, 1982.

[68] M. Psiaki and S. Mohiuddin, "Global positioning system integer ambiguity resolution using factorized least-squares techniques," *Journal of Guidance, Control, and Dynamics*, vol. 30, pp. 346–356, March-April 2007.

[69] X.-W. Chang and T. Zhou, "MILES: MATLAB package for solving Mixed Integer LEast Squares problems," *GPS Solutions*, vol. 11, no. 4, pp. 289–294, 2007.

[70] P. Xu, "Voronoi cells, probabilistic bounds, and hypothesis testing in mixed integer linear models," *IEEE Transactions on Information Theory*, vol. 52, no. 7, pp. 3122–3138, 2006.

[71] P. Teunissen, "Success probability of integer GPS ambiguity rounding and bootstrapping," *Journal of Geodesy*, vol. 72, no. 10, pp. 606–612, 1998.

[72] P. Teunissen, "Gnss ambiguity bootstrapping: theory and application," in *Proceedings of International Symposium on Kinematic Systems in Geodesy, Geomatics and Navigation*, pp. 246–254, 2001.

[73] S. Verhagen, "On the reliability of integer ambiguity resolution," *Navigation, Journal of the Institute of Navigation*, vol. 52, no. 2, pp. 99–110, 2005.

[74] S. Verhagen, B. Li, and P. J. Teunissen, "Ps-lambda: Ambiguity success rate evaluation software for interferometric applications," *Computers & Geosciences*, vol. 54, pp. 361–376, 2013.

[75] A. Thompson, J. Moran, and G. Swenson, *Interferometry and Synthesis in Radio Astronomy*, ch. 9: Very-Long-Baseline Interferometry, pp. 304–382. Wiley, 2001.

[76] O. Woodman, "An introduction to inertial navigation," *University of Cambridge, Computer Laboratory, Tech. Rep. UCAMCL-TR-696*, 2007.

[77] Y. Bar-Shalom, X. R. Li, and T. Kirubarajan, *Estimation with Applications to Tracking and Navigation*. New York: John Wiley and Sons, 2001.

[78] T. E. Humphreys, B. M. Ledvina, M. L. Psiaki, and P. M. Kintner, Jr., "GNSS receiver implementation on a DSP: Status, challenges, and prospects," in *Proceedings of the ION GNSS Meeting*, (Fort Worth, TX), pp. 2370–2382, Institute of Navigation, 2006.

[79] T. E. Humphreys, J. Bhatti, T. Pany, B. Ledvina, and B. O'Hanlon, "Exploiting multicore technology in software-defined GNSS receivers," in *Proceedings of the ION GNSS Meeting*, (Savannah, GA), pp. 326–338, Institute of Navigation, 2009.

[80] B. O'Hanlon, M. Psiaki, S. Powell, J. Bhatti, T. E. Humphreys, G. Crowley, and G. Bust, "CASES: A smart, compact GPS software receiver for space weather monitoring," in *Proceedings of the ION GNSS Meeting*, (Portland, Oregon), pp. 2745–2753, Institute of Navigation, 2011.

[81] STMicroelectronics, *Datasheet: ST iNEMO inertial module*, 2012.

[82] J. Huang, F. Qian, A. Gerber, Z. M. Mao, S. Sen, and O. Spatscheck, "A close examination of performance and power characteristics of 4g lte networks," in *Proceedings of the 10th international conference on Mobile systems, applications, and services*, pp. 225–238, ACM, 2012.

[83] W. Mao, H. Tsao, and F. Chang, "Intelligent GPS receiver for robust carrier phase tracking in kinematic environments," in *IEE Proceedings, Radar, Sonar and Navigation*, vol. 151, pp. 171–180, IET, 2004.

[84] M. Lashley, D. M. Bevly, and J. Y. Hung, "Performance analysis of vector tracking algorithms for weak GPS signals in high dynamics," *Selected Topics in Signal Processing, IEEE Journal of*, vol. 3, no. 4, pp. 661–673, 2009.

[85] M. Sahmoudi and R. J. Landry, "Multipath mitigation techniques using maximum-likelihood principle," *Inside GNSS*, pp. 24–29, 2008.

[86] F. van Diggelen, "Expert advice: Are we there yet? The state of the consumer industry," *GPS World*, Mar. 2010. GPS World.

[87] C. Miller, K. O'Keefe, and Y. Gao, "Time correlation in GNSS positioning over short baselines," *Journal of Surveying Engineering*, vol. 138, no. 1, pp. 17–24, 2011.

[88] C. Miller, K. OKeefe, and Y. Gao, "Operational performance of RTK positioning when accounting for the time correlated nature of GNSS phase errors," in *Proceedings of the ION GNSS Meeting*, pp. 21–24, 2010.

[89] K. O'Keefe, M. Petovello, G. Lachapelle, and M. E. Cannon, "Assessing probability of correct ambiguity resolution in the presence of time-correlated errors," *Navigation, Journal of the Institute of Navigation*, vol. 53, no. 4, pp. 269–282, 2007.

[90] M. G. Petovello, K. OKeefe, G. Lachapelle, and M. E. Cannon, "Consideration of time-correlated errors in a Kalman filter applicable to GNSS," *Journal of Geodesy*, vol. 83, no. 1, pp. 51–56, 2009.

[91] S. Han and C. Rizos, "Standardization of the variance-covariance matrix for GPS rapid static positioning," *Geomat. Res. Aust.*, vol. 62, pp. 37–54, 1995.

[92] P. Teunissen, "GPS ambiguity resolution: impact of time correlation, cross-correlation and satellite elevation dependence," *Studia Geophysica et Geodaetica*, vol. 41, no. 2, pp. 181–195, 1997.

[93] B. Li, S. Verhagen, and P. J. Teunissen, "Robustness of GNSS integer ambiguity resolution in the presence of atmospheric biases," *GPS Solutions*, vol. 18, no. 2, pp. 283–296, 2014.

[94] T. Pany, N. Falk, B. Riedl, C. Stber, J. Winkel, and H.-P. Ranner, "GNSS synthetic aperture processing with artificial antenna motion," in *Proceedings of the ION GNSS+ Meeting*, (Nashville, Tennessee), Institute of Navigation, 2013.

[95] Novatel, *Datasheet: GPS-702L Dual-Frequency Pinwheel GPS Antenna*, 2014.

[96] Antcom, *Datasheet: Active L1/L2 GPS Antenna, P/N: 53G1215A-XT-1*, 2006.

[97] Taoglas, *Datasheet: Active L1 GPS Antenna, P/N: Dominator AA.161.*

[98] T. Takasu and A. Yasuda, "Kalman-filter-based integer ambiguity resolution strategy for long-baseline RTK with ionosphere and troposphere estimation," in *Proceedings of the ION National Technical Meeting*, 2010.

[99] T. E. Humphreys, "How to fool a GPS," Feb. 2012. `http://www.ted.com/talks/todd_humphreys_how_to_fool_a_gps`.

[100] R. van Nee, J. Siereveld, P. Fenton, and B. Townsend, "The multipath estimating delay lock loop: approaching theoretical accuracy limits," in *Proceedings of the IEEE/ION PLANS Meeting*, pp. 246–251, IEEE, 1994.

[101] B. Townsend, P. Fenton, K. Van Dierendonck, and R. Van Nee, "L1 carrier phase multipath error reduction using MEDLL technology," in *Proceedings of the ION GPS Meeting*, vol. 8, pp. 1539–1544, INSTITUTE OF NAVIGATION, 1995.

[102] M. L. Psiaki, T. Ertan, B. W. O'Hanlon, and S. P. Powell, "GNSS multipath mitigation using antenna motion," *Navigation, Journal of the Institute of Navigation*, vol. 62, no. 1, pp. 1–22, 2015.

[103] P. Axelrad, C. J. Comp, and P. F. MacDoran, "SNR-based multipath error correction for GPS differential phase," *IEEE Transactions on Aerospace and Electronic Systems*, vol. 32, no. 2, pp. 650–660, 1996.

[104] L. Garin and J.-M. Rousseau, "Enhanced strobe correlator multipath rejection for code & carrier," in *Proceedings of the ION GPS Meeting*, pp. 559–568, 1997.

[105] L. Lau and P. Cross, "Development and testing of a new ray-tracing approach to GNSS carrier-phase multipath modelling," *Journal of Geodesy*, vol. 81, no. 11, pp. 713–732, 2007.

[106] M. S. Braasch, "Performance comparison of multipath mitigating receiver architectures," in *Aerospace Conference, 2001, IEEE Proceedings.*, vol. 3, pp. 3–1309, IEEE, 2001.

[107] C. Mekik and O. Can, "An investigation on multipath errors in real time kinematic GPS method," *Scientific Research and Essays*, vol. 5, no. 16, pp. 2186–2200, 2010.

[108] J. Tranquilla, J. Carr, and H. M. Al-Rizzo, "Analysis of a choke ring groundplane for multipath control in global positioning system (gps) applications," *IEEE Transactions on Antennas and Propagation*, vol. 42, no. 7, pp. 905–911, 1994.

[109] W. Kunysz, "High performance GPS pinwheel antenna," in *Proceedings of the ION International Technical Meeting*, pp. 19–22, 2000.

[110] J. Ray, M. Cannon, and P. Fenton, "GPS code and carrier multipath mitigation using a multiantenna system," *IEEE Transactions on Aerospace and Electronic Systems*, vol. 37, no. 1, pp. 183–195, 2001.

[111] P. E. Gill, W. Murray, and M. H. Wright, *Practical optimization.* Academic press, 1981.

[112] J. Ray and M. Cannon, "Characterization of GPS carrier phase multipath," in *Proceedings of the ION National Technical Meeting*, 1999.

[113] D. F. Bétaille, P. A. Cross, and H.-J. Euler, "Assessment and improvement of the capabilities of a window correlator to model GPS multipath phase errors," *IEEE Transactions on Aerospace and Electronic Systems*, vol. 42, no. 2, pp. 705–717, 2006.

[114] J. J. Spilker, Jr., *Global Positioning System: Theory and Applications*, ch. 14: Multipath Effects, pp. 547–568. Washington, D.C.: American Institute of Aeronautics and Astronautics, 1996.

[115] V. U. Zavorotny, K. M. Larson, J. J. Braun, E. E. Small, E. D. Gutmann, and A. L. Bilich, "A physical model for GPS multipath caused by land reflections: Toward bare soil moisture retrievals," *Selected Topics in Applied Earth Observations and Remote Sensing, IEEE Journal of*, vol. 3, no. 1, pp. 100–110, 2010.

[116] P. Closas, C. Fernandez-Prades, and J. A. Fernandez-Rubino, "A Bayesian approach to multipath mitigation in GNSS receivers," *IEEE Journal of Selected Topics in Signal Processing*, vol. 3, pp. 695–706, Aug. 2009.

[117] S. N. Sadrieh, A. Broumandan, and G. Lachapelle, "Spatial/temporal characterization of the GNSS multipath fading channels," in *Proceedings of the ION GNSS Meeting*, pp. 393–401, 2010.

[118] P. J. Teunissen and D. Odijk, "Ambiguity dilution of precision: definition, properties and application," *Proceedings of ION GPS-1997*, pp. 16–19, 1997.

[119] D. Odijk and P. Teunissen, "Sensitivity of ADOP to changes in the single-baseline GNSS model," *Artificial Satellites*, vol. 42, no. 2, pp. 71–96, 2007.

[120] J. Skaloud, "Reducing the GPS ambiguity search space by including inertial data," in *Proceedings of the ION International Technical Meeting*, pp. 2073–2080, 1998.

[121] J. Wendel, J. Metzger, R. Moenikes, A. Maier, and G. Trommer, "A performance comparison of tightly coupled GPS/INS navigation systems based on extended and sigma point kalman filters," *Navigation, Journal of the Institute of Navigation*, vol. 53, no. 1, pp. 21–31, 2006.

[122] C. Goodall, S. Carmichael, N. El-Sheimy, and B. Scannell, "INS face off: MEMS versus FOG," *Inside GNSS*, pp. 48–55, July/August 2012.

[123] B. Carse, B. Meadows, R. Bowers, and P. Rowe, "Affordable clinical gait analysis: An assessment of the marker tracking accuracy of a new low-cost optical 3d motion analysis system," *Physiotherapy*, vol. 99, no. 4, pp. 347–351, 2013.

[124] A. K. Brown, "GPS/INS uses low-cost MEMS IMU," *Aerospace and Electronic Systems Magazine, IEEE*, vol. 20, no. 9, pp. 3–10, 2005.

[125] A. Angrisano, M. Petovello, and G. Pugliano, "Benefits of combined GPS/GLONASS with low-cost MEMS IMUs for vehicular urban navigation," *Sensors*, vol. 12, no. 4, pp. 5134–5158, 2012.

[126] D. P. Shepard and T. E. Humphreys, "High-precision globally-referenced position and attitude via a fusion of visual SLAM, carrier-phase-based GPS, and inertial measurements," in *Proceedings of the IEEE/ION PLANS Meeting*, May 2014.

[127] R. Hartley and A. Zisserman, *Multiple view geometry in computer vision*, vol. 2. Cambridge Univ Press, 2000.

[128] B. Triggs, P. McLauchlan, R. Hartley, and A. Fitzgibbon, "Bundle adjustment–a modern synthesis," *Vision algorithms: theory and practice*, pp. 153–177, 2000.

[129] H. Strasdat, J. Montiel, and A. J. Davison, "Visual slam: Why filter?," *Image and Vision Computing*, 2012.

[130] G. Nuetzi, S. Weiss, D. Scaramuzza, and R. Siegwart, "Fusion of IMU and vision for absolute scale estimation in monocular SLAM," *Journal of Intelligent & Robotic Systems*, vol. 61, pp. 287–299, Jan. 2011.

[131] G. Klein and D. Murray, "Parallel tracking and mapping for small AR workspaces," in *6th IEEE and ACM International Symposium on Mixed and Augmented Reality*, pp. 225–234, IEEE, 2007.

[132] M. I. Lourakis and A. A. Argyros, "SBA: A software package for generic sparse bundle adjustment," *ACM Transactions on Mathematical Software (TOMS)*, vol. 36, no. 1, p. 2, 2009.

[133] T. E. Humphreys, "Attitude determination for small satellites with modest pointing constraints," in *Proc. 2002 AIAA/USU Small Satellite Conference*, (Logan, Utah), 2002.

[134] B. K. Horn, "Closed-form solution of absolute orientation using unit quaternions," *JOSA A*, vol. 4, no. 4, pp. 629–642, 1987.

[135] C. Wu, "VisualSFM: A visual structure from motion system," 2011. `http://ccwu.me/vsfm`.

[136] C. Wu, S. Agarwal, B. Curless, and S. M. Seitz, "Multicore bundle adjustment," in *Computer Vision and Pattern Recognition (CVPR), 2011 IEEE Conference on*, pp. 3057–3064, IEEE, 2011.

[137] C. Wu, "Siftgpu: A gpu implementation of scale invariant feature transform (sift)," 2007. `http://cs.unc.edu/~ccwu/siftgpu`.

[138] Y. Furukawa, B. Curless, S. M. Seitz, and R. Szeliski, "Clustering views for multi-view stereo," *IEEE Trans. Pattern Anal. Mach. Intell*, pp. 1362–1376, 2010.

[139] Y. Furukawa and J. Ponce, "Accurate, dense, and robust multiview stereopsis," *Pattern Analysis and Machine Intelligence, IEEE Transactions on*, vol. 32, no. 8, pp. 1362–1376, 2010.

[140] G. L. Mader, "GPS antenna calibration at the national geodetic survey," *GPS solutions*, vol. 3, no. 1, pp. 50–58, 1999.

[141] S. Verhagen, P. J. Teunissen, and D. Odijk, "The future of single-frequency integer ambiguity resolution," in *VII Hotine-Marussi Symposium on Mathematical Geodesy*, pp. 33–38, Springer, 2012.

[142] M. Pratt, B. Burke, and P. Misra, "Single-epoch integer ambiguity resolution with GPS-GLONASS L1 data," in *Proceedings of the 53rd Annual Meeting of The Institute of Navigation*, (Albuquerque, NM), pp. 691–699, 1997.

[143] Y. Wu and Z. Hu, "PnP problem revisited," *Journal of Mathematical Imaging and Vision*, vol. 24, no. 1, pp. 131–141, 2006.

[144] C.-X. Zhang and Z.-Y. Hu, "Probabilistic study on the multiple solutions of the P3P problem.," *Ruan Jian Xue Bao(Journal of Software)*, vol. 18, no. 9, pp. 2100–2104, 2007.

[145] T. Takasu and A. Yasuda, "Cycle slip detection and fixing by MEMS-IMU/GPS integration for mobile environment RTK-GPS," in *Proc. 21st Int. Tech. Meeting of the Satellite Division of the Institute of Navigation (ION GNSS 2008), Savannah, GA*, pp. 64–71, 2008.

[146] C. Altmayer, "Enhancing the integrity of integrated GPS/INS systems by cycle slip detection and correction," in *Intelligent Vehicles Symposium, 2000. IV 2000. Proceedings of the IEEE*, pp. 174–179, IEEE, 2000.

[147] O. L. Colombo, U. V. Bhapkar, and A. G. Evans, "Inertial-aided cycle-slip detection/correction for precise, long-baseline kinematic GPS," in *Proceedings of the ION GPS*, 1999.

[148] A. J. Van Dierendonck, "How GPS receivers measure (or should measure) ionospheric scintillation and TEC and how GPS receivers are affected by the ionosphere," in *Proc. 11th International Ionospheric Effects Symposium*, (Alexandria, VA), 2005.

[149] P. Teunissen and A. Khodabandeh, “Review and principles of PPP-RTK methods,” *Journal of Geodesy*, vol. 89, no. 3, pp. 217–240, 2014.

[150] D. Odijk, P. J. Teunissen, and A. Khodabandeh, “Single-frequency PPP-RTK: theory and experimental results,” in *Earth on the Edge: Science for a Sustainable Planet*, pp. 571–578, Springer, 2014.

[151] G. Hu, H. Khoo, P. Goh, and C. Law, “Development and assessment of GPS virtual reference stations for RTK positioning,” *Journal of Geodesy*, vol. 77, no. 5-6, pp. 292–302, 2003.